Radiometric Sensitivity to Soil Moisture Relative to Vegetation Canopy Anisotropy, Canopy Temperature, and Canopy Water Content at 1.4 GHz

by

Brian Kirk Hornbuckle

A dissertation submitted in partial fulfillment
of the requirements for the degree of
Doctor of Philosophy
(Electrical Engineering and Atmospheric, Oceanic & Space Sciences)
at The University of Michigan
2003

Doctoral Committee:

Professor Anthony W. England, Chair
Professor Henry N. Pollack
Assistant Research Scientist Roger D. De Roo
Professor Emeritus Donald J. Portman
Professor John M. Norman, The University of Wisconsin, Madison

ABSTRACT

Radiometric Sensitivity to Soil Moisture Relative to
Vegetation Canopy Anisotropy, Canopy Temperature,
and Canopy Water Content at 1.4 GHz

by
Brian Kirk Hornbuckle

Chair: Anthony W. England

Many impacts of climate change will be expressed in the hydrologic cycle. Microwave radiometry is sensitive to the quantity and distribution of water in soil and vegetation. Recent advances in technology will allow global measurements at useful spatial resolutions. Critical to this vision is the development of reliable models of microwave brightness. In this dissertation, measurements of 1.4 GHz brightness, micrometeorology, and soil moisture were collected over the course of the growing season in a field of corn. It was determined that the brightness of a field–corn canopy at both polarizations is isotropic in azimuth during much of the season. At senescence, brightness is a function of row direction. This phenomenon is caused by water loss from the leaves, which when dry become essentially invisible. The question is raised whether other biophysical processes associated with critical periods of drought or extreme wetness could cause similar changes in the effective constitutive properties of the canopy. A current model of microwave brightness, appropriate for weakly–scattering canopies, was unable to predict change in brightness with incidence angle. Significant scatter darkening was observed. A new model was formulated with an anisotropic canopy. The new model was compared to continuous measurements of brightness collected during the highest canopy biomass of the season. With the aid of

coincident measurements of micrometeorology and soil moisture, the radiometric sensitivities to vegetation canopy temperature, soil moisture, and canopy water, either in the form of intercepted precipitation or dew, were determined and compared to sensitivities in a hypothetical nonscattering canopy of equivalent density, such as thick grass. Sensitivity to canopy temperature is similar in both types of canopies. Soil moisture sensitivity is higher in the corn canopy where moisture is concentrated in stems and fruit. An increase in canopy water has the net effect of decreasing the brightness equally at both polarizations in corn, while an increase in brightness occurs in nonscattering canopies. Dew can decrease the brightness more than a soaking rain. With an appropriate emission model, there will be year round sensitivity to soil moisture in most, and perhaps all, agricultural crops.

Completed in memory of J. Edwin Nelson and Glen C. Hornbuckle.

I wish I could have shared my joy with you during this process.

Dedicated to Jalene, Amaris, Malachi, and Eliana Hornbuckle.

May our family continue to receive God's blessings

and share them with others.

ACKNOWLEDGEMENTS

Five people made this work possible.

- Mark Fischman built the first 1.4 GHz radiometers.
- Roger De Roo made them work in the field.
- David Boprie made everything else work.
- Tony England found a way to bring all of these people together.
- Jason Woods provided an experiment site.

I have been fortunate to have Tony England as my advisor. He allowed me to travel, to take chances, even at the risk of damaging his reputation, and provided me with independence. He has also been a superb mentor and I hope to follow his example of integrity. Thank you, Tony.

I shared countless hours of field work with David Boprie. Your contribution to the group has been invaluable. Thank you for watching out for me. I will miss your companionship.

Roger De Roo was always willing to answer any questions. Thank you for sharing your time with me and others. I thank Don Portman serving on my committee and the significant amount of time he spent with me in the field and carefully reading my manuscripts. John Norman added a new dimension to my education after agreeing to serve on my committee and has become a valuable mentor. I appreciate Henry Pollack's willingness to join my committee late in the process.

I can not thank Jason Woods enough for the use of his farm and a remarkable field site. The quality of the measurements in this work reflect his and his father's stewardship of their land. Ned Birkey of Monroe County Extension introduced me to farmers in the area and kept me involved with agriculture in southeast Michigan. Gerard Kluitenberg at Kansas State gave instrumentation advice and provided soil texture analysis. Tom Stoffel of the National Renewable Energy Lab, Tom Kirk of Eppley Lab, Jim Bilskie and Ed Swiatek of Campbell Scientific, and Sally Logsdon of the Soil Tilth Lab all provided valuable instrumentation advice. I would also like to thank Avery Demond for use of her lab in Civil and Environmental Engineering and Jodi Ryder for her help.

I appreciate the assistance of the following people in the field: David Boprie, Roger De Roo, Ed Kim, Mark Fischman, Xiaohua Lin, Yuka Muto, Hanh Pham, Ying–Ying Zhang, Mike Carr, Emily Faivre, Ryan Peterson, Soumitra Ray, Catherine Piowtrowski, Tarreg Mawari, Aneela Qureshi, Mauricio Vacas, Don Portman, Tony England, and C. E. Hornbuckle. I appreciate the loan of instruments from Frank Marsik and the Global Change Laboratory at UM and Tom Jackson of the United States Department of Agriculture.

I would also like to acknowledge the love and support of my parents, Carol and C. E. Hornbuckle, and Jalene's parents, Brooksie and Doug Miller.

Finally, I thank my wife Jalene for her love, companionship, affection, and endurance during this process. I especially am grateful for her determination that I keep my responsibilities as a father throughout the last four and a half years. Because of her hard work, we are the proud parents of three wonderful children: Amaris, Malachi, and Eliana.

This work was supported by NASA grant NAG5–8661 from the Land Surface Hydrology Program. I am grateful for tuition and stipend support provided by an NSF Science and Engineering Graduate Fellowship, an EPA STAR Graduate Fellowship, a Michigan Society of Fellows Associate Fellowship, and finally by a Lyman Judson Fellowship from Rackham Graduate School.

"Thanks Be to God." Ann Arbor, Michigan, February 6, 2003.

TABLE OF CONTENTS

LIST OF TABLES

LIST OF FIGURES

Figure

CHAPTER 1

Climate Variability, Soil Moisture, and Microwave Radiometry

1.1 Introduction

To what degree is climate changing in response to human activities?

What would be the impacts of any climate change?

What amount of natural climate variability can be expected?

We can answer these important questions now with some certainty. There has been significant warming over the past century in the observational record [*Intergovernmental Panel on Climate Change*, 1996] and the twentieth century was the warmest of the past five centuries [*Pollack et al.*, 1998]. Losses in weather catastrophes have increased steadily over the past fifty years, due to both an increase in the frequency of catastrophes and to shifts in land use, a sign of society's increasing susceptibility to extreme weather [*Kunkel et al.*, 1999b]. To separate anthropogenic effects from naturally occurring variability, we must continue to develop our understanding of Earth's climate. One important process that is still not well understood is the exchange of water between the soil, vegetation, and atmosphere.

> "Water is at the heart of climate change and the impacts of climate variability. Any assessment of climate change, its causes and impacts, must be based

> on significantly better observations of the water cycle." [*National Research Council*, 1999]

Microwave radiometry, the measurement of naturally emitted microwave radiation, is sensitive to the presence of liquid water. When directed toward the earth's surface, it can reveal the the quantity and distribution of water stored in vegetation and the first few centimeters of the soil, key components of the water cycle. Although the response to changes in soil water content has been well documented, there are still many questions about the effect of the overlying vegetation. For example:

- Can scattering of radiation within the vegetation canopy be neglected? The most widely used model for land surface microwave brightness assumes negligible scattering, but it has been validated only at steep angles of incidence at which the vegetation has the least impact.

- At what level of vegetation is there no longer any useful sensitivity to changes in soil water content? Does the transparency of the canopy depend on simply the amount of water in the canopy or also on its distribution?

- What effect do changes in vegetation water content have upon the emitted microwave radiation? These variations can be caused by intercepted precipitation and dew, or by slower, more subtle processes such as diurnal variations, senescence, and plant response to drought or extreme wetness.

In this dissertation, I first examine the electromagnetic properties of one type of vegetation canopy, field corn, and show that if scattering is neglected, the canopy must be considered an anisotropic medium. I then formulate a new model which assumes weak scattering. Finally, I quantify the effect of changes in vegetation temperature, soil moisture, and the amount and distribution of moisture within a corn canopy on the microwave brightness, and compare these effects with those which would be observed in a hypothetical nonscattering canopy such as thick grass by comparing the new model with observations.

Both the European Space Agency and NASA have plans to launch satellite microwave radiometers later this decade. These new instruments, in conjunction with the findings of this dissertation and other ongoing research, will allow us to further our understanding of the climate system and, in the future, to intelligently manage humanity's impact on Earth's climate and environment.

1.2 Observed Change in Mean Climate and Climate Variability

An increase of 0.6°C in the global mean temperature record since the beginning of the 20th century has been observed [*Intergovernmental Panel on Climate Change*, 1996]. Using data from 358 boreholes in eastern North America, central Europe, southern Africa, and Australia, *Pollack et al.* [1998] concluded that the average surface temperature has increased 0.5°C in the 20th century and that the 20th century is the warmest of past five centuries. Furthermore, a greater warming in daily minimum temperature than daily maximum temperature has been observed [*Easterling et al.*, 1997]. Not only have mean temperatures increased in the past century, it also appears that they have become more variable. In the United States, for example, the two–month period of November and December, 2000, was the coldest such period on record. This followed the warmest winter on record, and the January through October, 2000, period was the warmest 10–month period since records began in 1895. The ten warmest years on record have all occurred since 1983 [*News and Notes*, 2001].

1.2.1 Hydrologic Change

Besides changes in temperature during the past century, changes in Earth's hydrology have also been observed. The areas of the world affected by drought or excessive wetness has increased overall, although there is significant local variability. In the United States, excessive wetness is increasing, while in China, an increase in the areas affected by drought

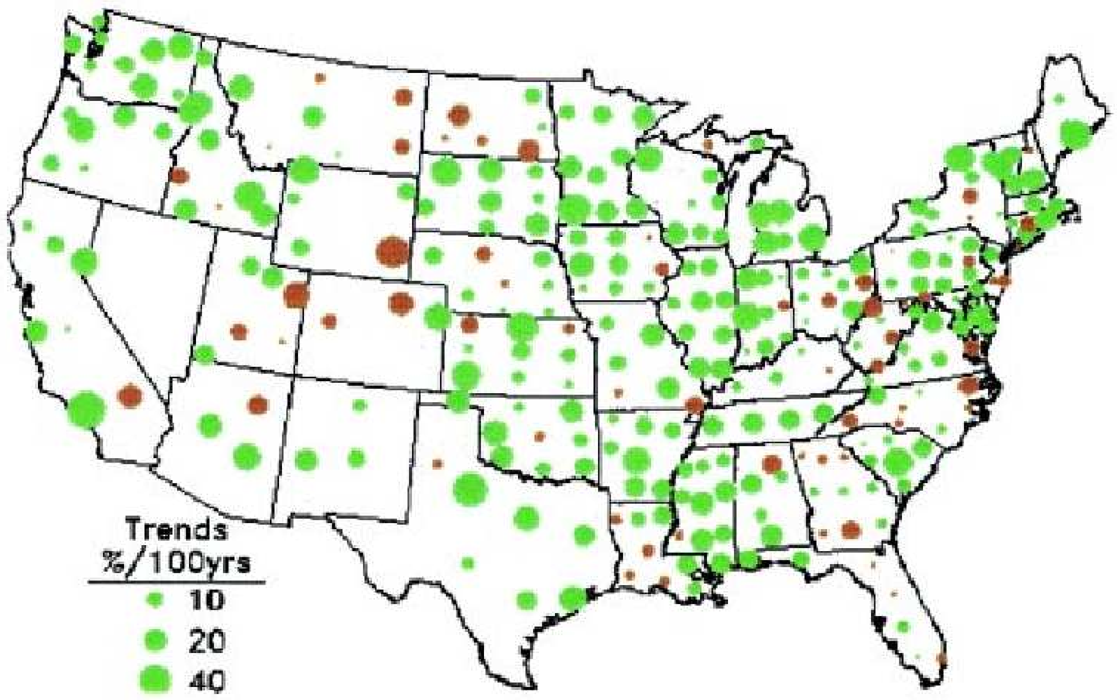

Figure 1.1: Observed linear trends in annual precipitation (% per century) during the 20th century. Green (light) dots indicate increasing trends and brown (dark) dots indicate decreasing trends. From *Groisman et al.* [2001].

has been observed [*Easterling et al.*, 2000b]. Both an overall increase in annual precipitation (Figure 1.1) and an increase in heavy precipitation events have been observed in the United States [*Karl et al.*, 1996; *Karl and Knight*, 1998; *Kunkel et al.*, 1999a; *Groisman et al.*, 1999, 2001].

Changes in precipitation amount and frequency have also been observed worldwide. Figure 1.2 shows trends in total seasonal precipitation and the frequency of heavy precipitation within that season for various regions of the world during the past century. For each region (e.g. USA, W. USSR, etc.) the season with the maximum precipitation was selected. For the United States, this season is the summer (the months of June, July, and August). The frequency of heavy precipitation is found by counting the number of days the precipitation exceeds a region–specific threshold within that season. The thresholds range from 20 mm to 100 mm. The total length of time analyzed for each region ranges from 34 to 96

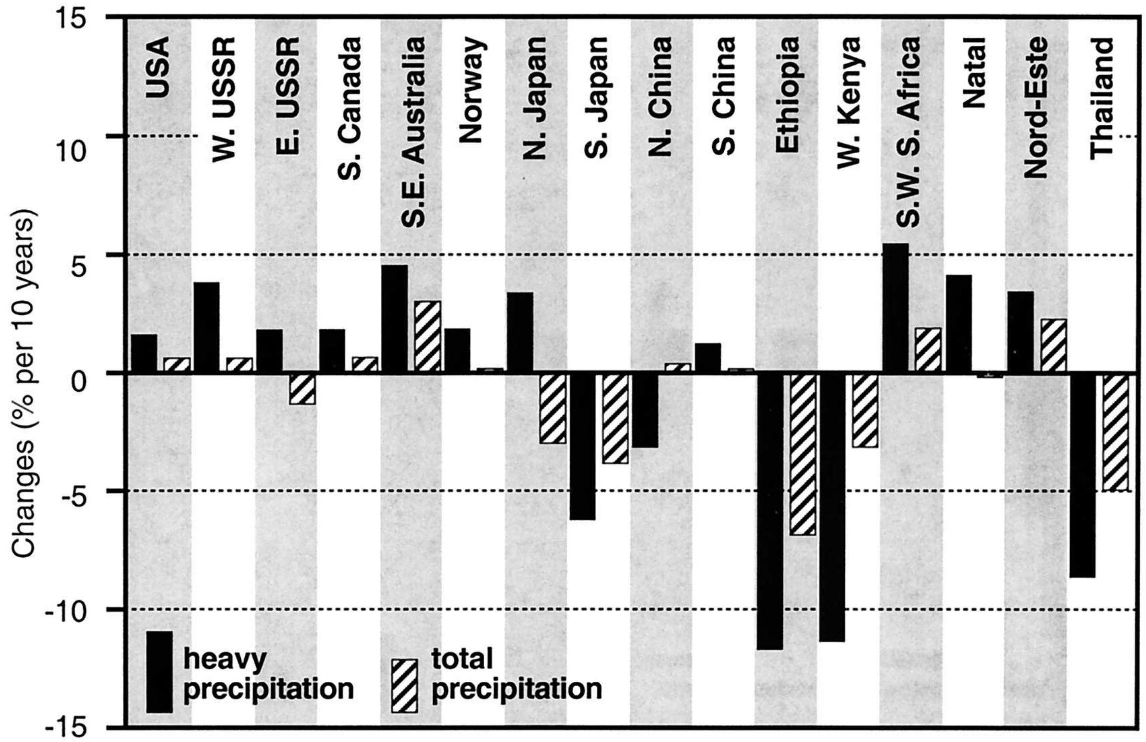

Figure 1.2: Observed linear trends in total seasonal precipitation and frequency of heavy precipitation events for various regions of the world during the 20th century. Natal is in South Africa, Nord–Este is in Brazil. From *Easterling et al.* [2000a].

years, with most regions having at least 50 years of data.

First, note that except for only a few regions (Norway, S. China, and Natal) the total amount of seasonal precipitation has changed significantly during the past century. Some regions are getting wetter, while others drier during their season of maximum precipitation. Next, the change in heavy precipitation usually has the same sign as the change in total precipitation during the season. In the European part of the former Soviet Union (W. USSR), as the total amount of seasonal precipitation has increased, the frequency of days with heavy precipitation has also increased. In Ethiopia, there has been a decrease in both the total amount of seasonal precipitation and the frequency of heavy precipitation events.

Changes with the same sign would be expected: part of the increase in precipitation is due to an increase frequency of heavy precipitation and vice versa. But the size of these changes relative to each other seem disproportionately large, i.e. it appears that not only is the frequency of heavy precipitation increasing as a result of the overall increase in precipitation, but the manner in which precipitation falls, either in light or heavy rain events (the variability of precipitation) is also changing. Although it is tempting to make this strong generalization, it can not be made solely on this information in all cases. On the other hand, in four regions (E. USSR, N. Japan, N. China, and Natal) the changes have opposite signs. In these regions, we can say with confidence that not only is the mean amount of seasonal precipitation changing, so is the variability. For example, there has been an increase in the frequency of heavy precipitation in N. Japan *despite the fact* that the overall amount has decreased.

Besides changes in precipitation, changes in streamflow data have also been observed. *Lins and Slack* [1999] analyzed streamflow data from the Hydro-Climatic Data Network (HCDN), a network of over 1500 stream gauges across the United States. Using a subset of these data consisting of stations with daily records over long periods of time, they found that annual low and median daily mean discharge rates have increased during the 20th century. Interestingly, the maximum average daily streamflow during each year had not increased significantly. *Groisman et al.* [2001] analyzed the same data set in order to discover why an increase in heavy precipitation events was apparently not causing an increase in maximum streamflow. After eliminating data from the Western United States, where snow melt can mask the effect of precipitation on streamflow, they found that in the Eastern United States there has been an increase in high streamflow during the month of maximum streamflow in response to the increase in heavy precipitation.

Douglas et al. [2000] also analyzed the HCDN streamflow data. They used a special statistical method designed to discount any significance resulting from correlated streamflow within the same basin. For example, if the streamflow at an up–river gauge is high, then naturally the streamflow downstream would also tend to be high. Their method included only one of these gauges in their analysis. Over a fifty year period from 1939 to 1988, no statistically significant increase in flood flows (the maximum average daily streamflow

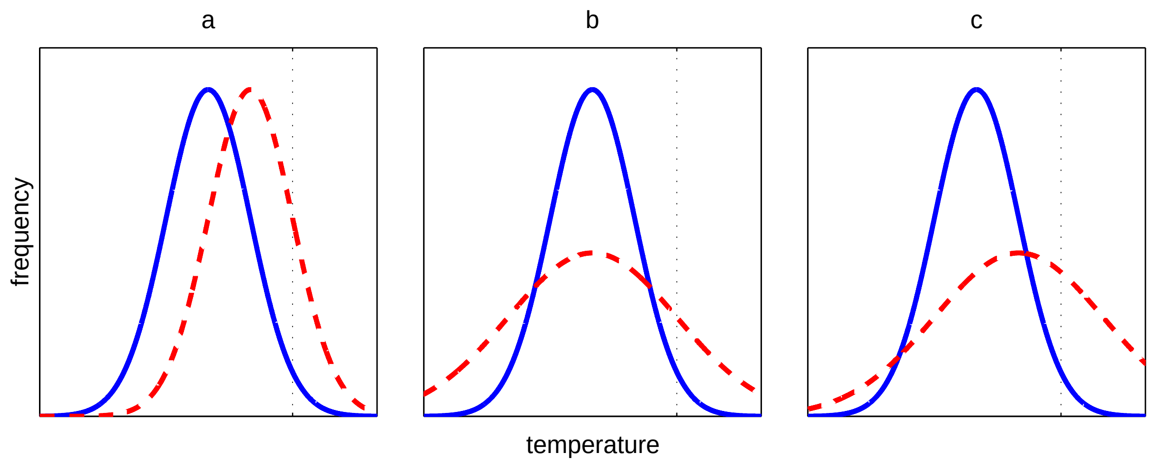

Figure 1.3: Impacts of a change in a change in mean (a), a change in variance (b), and a change in both mean and variance (c) on the frequency of extreme temperatures.

during each water year, October through September) were found at any time or space scale. However, an increase in the level of low flows (the lowest seven-day average streamflow during each drought year, April through March) was found in the Upper Midwest over the past fifty years.

1.3 Impacts of Climate Variability

Changes in Earth's climate may affect both mean values and the *frequency of extreme events*. For example, a single increase in mean daily maximum temperature may also increase the frequency of extreme high temperatures (plot a in Figure 1.3). If instead mean daily maximum temperatures do not change, a change in the variance, or spread, of the temperature distribution would also increase the frequency of extreme temperatures (plot b in Figure 1.3). A change in both mean and variance (plot c in Figure 1.3) would result in a much larger frequency of extreme temperatures than changes in mean or variance by themselves [*Meehl et al.*, 2000]. Although a general warming in the earth's climate is a concern, it is likely that humans can adapt to slow changes in mean temperature. On the other hand, we are much more sensitive to extreme weather events, part of the *climate variability*. An increase in extreme events such as heat waves, cold snaps, droughts, and floods could have

Table 1.1: Likelihood of global changes in climate extremes observed during the twentieth century and predicted for the twenty–first century. From *Easterling et al.* [2000b].

	Observed (20th Century)	*Predicted (21st Century)*
higher maximum temperatures	very likely	very likely
more hot summer days	likely	very likely
increase in heat index	likely	very likely
more heat waves	possible	very likely
higher minimum temperatures	virtually certain	very likely
fewer frost days	virtually certain	likely
fewer cold waves	very likely	very likely
more heavy one–day precip events	likely	very likely
more heavy multi–day precip events	likely	very likely
more drought	likely	very likely
more wet spells	likely	likely
more intense mid–latitude storms	possible	possible

devastating effects [*Kunkel et al.*, 1999b]. Not only should we be concerned with mean changes in temperature and precipitation, but also with how the variability of temperature and precipitation may be changing (Table 1.1).

One example of our susceptibility to climate variability is agriculture. Figure 1.4 is a graph of field corn yield versus year for five counties in Southeast Michigan since 1955. Note that although agricultural production has increased over the years, productivity is still limited by weather, in particular precipitation. Each dip in yield is associated with abnormally dry months during the growing season. The amount, timing, and seasonality of precipitation are all important [*Sharratt et al.*, 2001]. Both surface water (the moisture immediately replenished by precipitation) and groundwater (recharged slowly over the entire year) supply moisture to growing vegetation. For corn, during May and June the plant roots are too shallow to reach moisture well below the surface and hence depend on a pattern of precipitation that sufficiently wets the surface. By the middle of the summer, the amount of water lost through evapotranspiration outweighs the amount moisture in the form of precipitation, and the roots of the corn plant must pull moisture from deeper depths in the ground, moisture that was deposited during the preseason in the late fall, winter, and early spring.

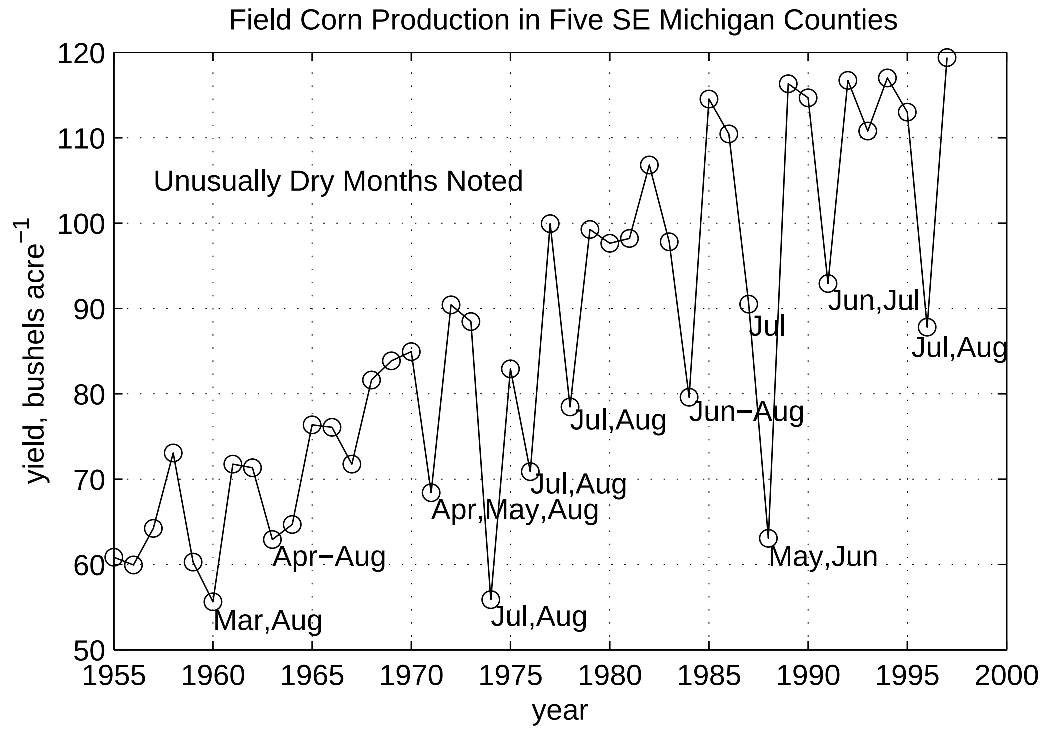

Figure 1.4: Yield (corn for grain) versus year for five southeast Michigan counties: Monroe, Lenawee, Hillsdale, Jackson, and Washtenaw. Yield data obtained by the author from the Published Estimates Database, United States Department of Agriculture (USDA) National Agriculture Statistics Service. Precipitation data used to identify dry months from the National Climatic Data Center. Measurements from the cities of Monroe (Monroe County), Adrian (Lenawee), Hillsdale (Hillsdale), Jackson (Jackson), and Ann Arbor (Washtenaw) were used to estimate regional precipitation. Months of unusually low precipitation are noted.

In most parts of the Corn Belt, the ground water moisture supply is almost always present and precipitation during the growing season is the limiting factor. On the western edge of the Corn Belt where annual rainfall is lower, this is not always the case. *Neild et al.* [1987] analyzed corn yields and precipitation data in Eastern Nebraska for dry–land (as opposed to irrigated) fields. When preseason (September to May) precipitation was above average, there was a 70% probability that corn yields would be above average also, regardless of what happened during the rest of the growing season.

Although a farmer must be able to survive occasional poor growing years, any increase in the variability of precipitation could disrupt this delicate balance and be economically disastrous to the agricultural community. Our world as a whole is becoming more sensitive to climate variability. Losses in weather catastrophes have increased steadily over the past fifty years, mainly due to shifts in land use (a greater susceptibility to extreme weather such as hurricanes and floods) and not just an increased frequency in the number of catastrophes [*Kunkel et al.*, 1999b].

1.3.1 Natural Climate Variability?

Despite the fact that the phrase “climate change” has only recently become part of our everyday language, there have *always* been varying amounts of climate change in Earth’s history. Since the Industrial Revolution, humans have had an increasingly stronger impact on the environment and climate. Although increased concentrations of greenhouse gases in the atmosphere from the combustion of fossil fuels lead scientists to believe that the climate variability observed in the past century is not part of the *natural climate variability*, they have yet to determine exactly how climate has been affected. The ability to answer this question is limited by the finite (and relatively short) length of the observational record and by incomplete knowledge of the processes which determine Earth’s climate.

Further study of the climate system will allow a better characterization of the climate we will experience in the future. In the meantime, it is only prudent to encourage the use of alternative sources of energy [*Hoffert et al.*, 2002] to avoid further compounding the problem. Otherwise we may consign ourselves to many negative consequences such as hotter and drier summers, the expansion of arid areas, drought in the tropics, and flooding in high– and mid–latitude rivers [*Wetherald and Manabe*, 2002].

1.4 Soil Moisture and its Effect on Climate

One important process that is not well understood is the cycling of water between the Earth’s surface and atmosphere. Water is continuously exchanged between the oceans, atmosphere, and land surface in a process known as the *hydrologic cycle*. Figure 1.5 illustrates the the dominant exchange mechanisms and storage areas of water on the Earth and

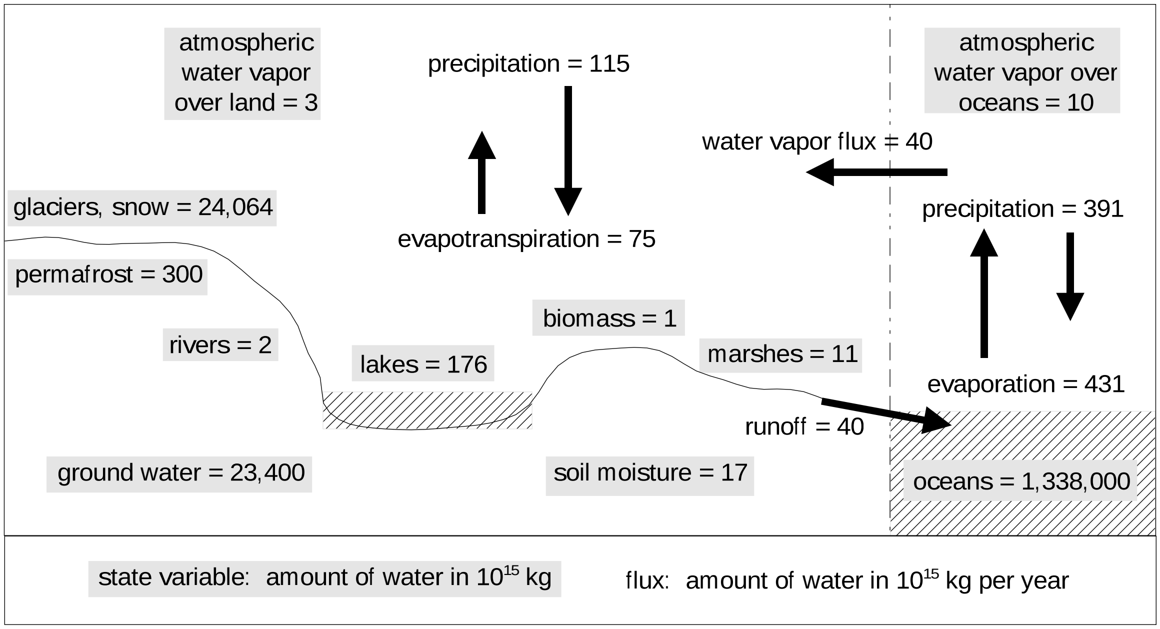

Figure 1.5: The global hydrologic cycle: flux and storage. Redrawn from *Oki* [1999].

their magnitude. The amount of water stored in the unsaturated zone of the Earth's surface above the water table is commonly referred to as *soil moisture*. Although the soil stores little water relative to other reservoirs, it receives the majority of the water returned to the surface via precipitation and is a major source of water for evaporation and transpiration. As a result, soil moisture is a very active reservoir unlike the other larger, essentially static reservoirs.

1.4.1 Surface Energy Budget

A more quantitative analysis of the role of soil moisture in the climate system can also be seen by examining the energy budget at the Earth's surface. The total amount of radiative energy per unit area per second directed towards the Earth's surface is the sum of the incident solar radiation, S, and emission from the atmosphere, A. Some of the solar radiation is reflected and the surface also emits radiation. The net radiation can be written [*Arya*, 1988]:

$$R_n = S + A - \left(aS + e\sigma T_s^4\right). \tag{1.1}$$

Here a is the albedo, σ is the Stefan–Boltzmann constant, e the emissivity, and T_s is the surface temperature. During the night, the net radiation is usually negative, but during the day it reaches several hundred W m^{-2}. By conservation of energy, the net radiation is balanced by sensible heat flux into the atmosphere, H_S; the flux of latent heat into the atmosphere, H_L; the flux of heat into the ground, G; and the rate of change of energy stored in the vegetation canopy (if present), $\dot{W}_{veg}$:

$$R_n = H_S + H_L + G + \dot{W}_{veg}. \tag{1.2}$$

H_S is primarily the convection (including conduction) of heat away from the surface. It is dependent on both the temperature difference between the surface and the atmosphere and the degree and nature of turbulence. Both G and $\dot{W}_{veg}$ are normally small when integrated over the course of a day.

Just as the human body perspires to cool itself when hot, so too "sweat" soil and vegetation when warmed by the sun. Accordingly, latent heat flux is equal to the rate of evaporation and transpiration, E, multiplied by the latent heat of vaporization, L_e:

$$H_L = L_e E. \tag{1.3}$$

Soil moisture is the source of most water evaporated from the soil and transpired by plants. In heavily vegetated areas, the evapotranspiration can be relatively large. For example, on a single day in the middle of August, 23,540 liters (6218 gallons) of water per acre were removed from the soil in a field of corn near Britton, Michigan, largely from transpiration but also by evaporation from the bare soil beneath the canopy [personal data, 1999]. In comparison, 25 mm (one inch) of rain on one acre of ground is equivalent to 102,900 liters (27,200 gallons) of water. During the height of the growing season in mid–August, this crop was removing the equivalent of more than an inch of rain from the soil *every five days*. In a single day, a hundred–acre field loses an amount of water equivalent to an Olympic–sized swimming pool. For a sense of the amount of latent heat transferred, imagine the energy required to boil the water of this swimming pool.

Eltahir [1998] outlined the details of a possible soil moisture – rainfall positive feedback. In general, wet soil increases net radiation, total heat flux into the atmospheric boundary layer (the layer of air directly influenced by the Earth's surface), and the moist static energy, W_{mse}, within the boundary layer. The moist static energy of an air parcel per unit mass is the sum of its potential energy, thermal energy, and latent heat stored by water vapor:

$$W_{mse} = gz + c_p T + L_e q \tag{1.4}$$

where g is the acceleration of gravity, z the elevation of the air parcel, c_p the air specific heat, T the temperature, and q the specific humidity. W_{mse} has units of energy per unit mass.

There are two main pathways through which soil moisture can enhance the likelihood of precipitation, which in turn raises the soil moisture and enhances precipitation.

1. Wet soil absorbs more solar radiation because of its lower albedo, which results in an increase in daytime R_n at the surface. This leads to a greater flux of energy into the boundary layer according to (1.2), which increases W_{mse}. An increase in W_{mse} strengthens both: the vertical gradient of W_{mse} in atmosphere, making convection and subsequent precipitation more likely; and the horizontal gradient of W_{mse}, enhancing atmospheric circulation and the movement of atmospheric moisture from other areas into the region. Furthermore, a higher W_{mse} brings the elevation at which water condenses in the boundary layer closer to the surface, increasing the likelihood of precipitation from convection.

2. Wet soil increases H_L which increases the total flux of energy and water vapor to the boundary layer and decreases the surface temperature. The decrease in surface temperature increases net radiation at surface according to (1.1), which leads to an increased probability of precipitation as detailed in the first pathway. The decrease in surface temperature also decreases the amount by which the air must cool in order to saturate (lowers the wet bulb depression) which allows clouds to form closer to the

surface and decreases the boundary layer depth. Given the same amount of H_S and H_L, W_{mse} is larger in a smaller boundary layer.

Eltahir [1998] supported this theoretical framework with data from the First International Satellite Land Surface Climatology Project (ISLSCP) Field Experiment (FIFE) in Kansas. Using soil moisture and precipitation records in Illinois, *Findell and Eltahir* [1997] found a small but statistically significant positive correlation between soil moisture and subsequent rainfall in Illinois. In a later paper, *Findell and Eltahir* [1999] used soil moisture and near surface observations of air temperature, humidity, and pressure in Illinois to further analyze soil moisture – rainfall feedback. They found that this feedback was not due to a positive correlation between soil moisture and boundary layer moist static energy, nor was there a positive correlation between moist static energy and precipitation. On the other hand, the theoretical relationship between soil moisture and wet bulb depression, and between wet bulb depression and subsequent rainfall *did* hold true.

Recently, *Findell* [2001] determined that a more complete analysis of the structure and composition of the boundary layer is needed to determine the relationship between soil moisture and precipitation. In particular, the moisture content of the air in the lower troposphere and the early morning temperature gradient between 1 and 3 km have a great influence on the likelihood of convection and subsequent rainfall. Using data from Illinois and a boundary layer model, she found that when the air is very moist, surface fluxes have little effect and the likelihood of precipitation is atmospherically controlled. The same is true for very dry air. Between these two extremes, the existence of a temperature inversion (virtual temperature increases with height) in the critical region inhibits convection. When there is a near dry adiabatic lapse rate (10 K km^{-1}), dry soils are more likely to induce convection, i.e. there is a *negative* feedback between soil moisture and precipitation. The dry adiabatic lapse rate is the rate at which dry air cools with elevation assuming no exchange of heat between an air parcel and the surrounding atmosphere. When the lapse rate is close to moist adiabatic, wet soils are more likely to induce precipitation (a *positive*

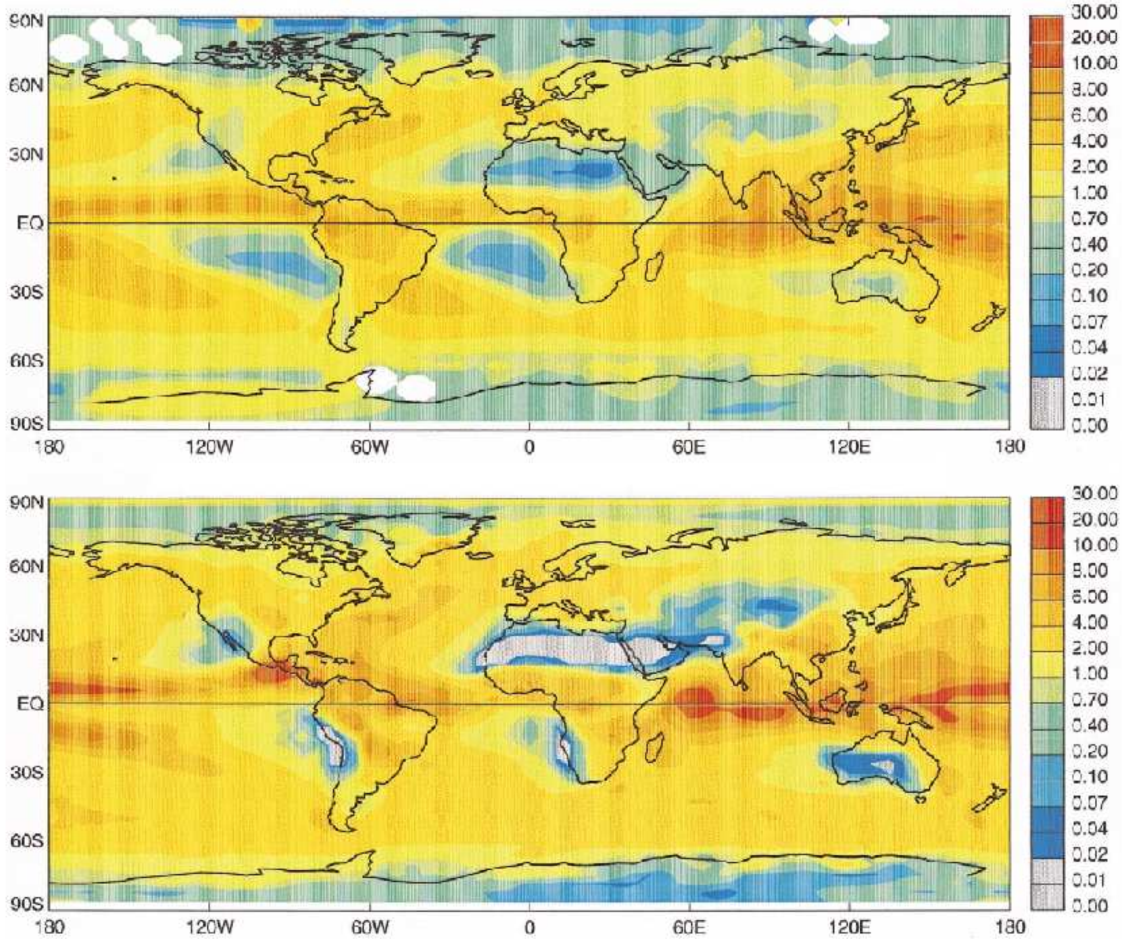

Figure 1.6: Mean annual precipitation in mm per day as computed using observations over a 17-year period (top) and by a GCM. From *Koster et al.* [2000].

feedback). The moist adiabatic lapse rate is the rate at which saturated air cools with elevation. It is always less than the dry adiabatic lapse rate because of release of latent heat with condensation.

1.4.2 Predictions of General Circulation Models (GCMs)

The relationship between soil moisture and precipitation, as well as the general role of soil moisture in the climate system, has also been examined using atmospheric General Circulation Models (GCMs), complex numerical models that simulate the behavior of the atmosphere on large scales. GCMs can not perfectly reproduce Earth's climate, but they are still extremely useful for two reasons. First, model predictions have been verified with actual observations in a qualitative sense. Figure 1.6 shows mean annual precipitation in mm per day as computed using observations over a 17-year period and by the NASA Goddard Earth Observing System-Climate (GEOS-ARIES) GCM with 720 years of forcing data. Note that the model reproduces the general qualities of observed precipitation, i.e. regions which are dry match the regions predicted to be dry, but the match is not perfect. For example, the Sahara Desert is easy to see in the model output, but it is too dry. Second, GCMs produce physically intuitive results. When high levels of carbon dioxide, methane, and other greenhouse gases occur in the atmosphere, GCMs correctly produce a warming of climate and an intensification of the water cycle [*Washington*, 1992].

Many researchers have used GCMs to investigate soil moisture's effect on climate. *Manabe* [1969] was able to reproduce the qualitative features of global water and energy cycle after incorporating the effect of land surface hydrology into one of the first GCMs. *Walker and Rowntree* [1977] found that when a desert area was replaced by moist land in a GCM, wetness was maintained for several weeks. This led them to conclude that ground dryness sustain desert conditions and that soil moisture is important both in short–range forecasts (one to two days) and over longer periods of time (more than 2 weeks). *Mahfouf* [1991] and *Mintz and Walker* [1993] both used GCM studies to illustrate the intricate relationship between soil moisture, evapotranspiration, and energy transfer at the Earth's surface. *Delworth and Manabe* [1989] compared a 50–year GCM simulation where soil moisture was free to change with a 50–year simulation where soil moisture was prescribed and verified that interactive soil moisture was directly connected to the fluctuations of near–surface relative humidity and temperature and increased the total variability of the atmosphere. *Segal and Arritt* [1992] found that a thermally–induced circulation equivalent in intensity to a sea breeze can be caused by sharp contrast between extended wet soil or crops and adjacent dry land areas.

1.4.3 Soil Moisture and Precipitation

A relationship between soil moisture and precipitation has been noted by other researchers in GCM studies. *Shukla and Mintz* [1982] found that rainfall, atmospheric motion, and temperature depend strongly on land surface evapotranspiration and that vegetation plays an important role in climate. *Rind* [1982] reduced soil moisture to 25% of its observed value, found that subsequent summertime temperatures are higher and precipitation decreases, and concluded that knowledge of late spring soil moisture can help predict summertime precipitation. *Yeh et al.* [1984] found that irrigation affected the distribution of evaporation and precipitation and that anomalies of soil moisture persisted for several months due to positive feedback between increased evaporation and precipitation. *Oglesby and Erickson* [1989] concluded that reduced soil moisture can prolong and amplify North American drought. *Koster and Suarez* [1996] found that shortening the soil water retention period resulted in increased precipitation variance. *Bonan and Stillwell-Soller* [1998] concluded that soil moisture feedbacks amplified the severity and persistence of floods and droughts in the Mississippi River Basin.

Beljaars and Viterbo [1999] emphasized the importance of the land surface by illustrating the improvement in precipitation forecasts in the European Center for Medium–range Weather Forecasting's (ECMWF) GCM when modeling of land–atmosphere interaction was improved. *Koster et al.* [2000] found that land–atmosphere feedback can amplify or suppress the chaotic nature of the atmosphere. Knowledge of the land surface state improved precipitation predictability in "transition" regions between very humid and very dry areas, typically over the middle of large continents, where there is sufficient energy to evaporate surface water and surface water is variable. On the other hand, knowledge of sea surface temperature (SST) is more useful at higher latitudes where net radiation is low, and in deserts and very humid and wet areas. *Hong and Pan* [2000] observed strong positive feedback between soil moisture and precipitation due mostly to the effect on turbulent mixing than the input of moisture into atmosphere. *Hong and Kalnay* [2000] simulated the Oklahoma–Texas drought of 1998 and found that SST anomalies and favorable initial conditions established the drought in the late spring and that the drought was maintained by positive feedback from dry soil moisture conditions during the summer. The drought ended in the fall when stronger large–scale weather systems overwhelmed the soil moisture positive feedback. They also emphasized that when appropriate physical models of land–atmosphere interaction are incorporated into GCMs, forecasting skill will greatly increase.

1.4.4 Soil Moisture and Extreme Weather

Researchers have also used GCMs retrospectively to study extreme weather events. *Chang and Wetzel* [1991] simulated the development of a tornado that occurred during relatively quiet atmospheric conditions near Grand Island, Nebraska. They compared three different GCM simulations: no spatial variation of soil moisture or vegetation; soil moisture variation; and soil and vegetation variation. Realistic soil moisture and vegetation variations produced the best forecast and they noted that the "observed stationary front was strongly enhanced by differential heating caused by observed gradients of soil moisture, as acted upon by the vegetation cover."

Pan et al. [1995] found that artificially adding moisture to soil in a GCM simulating the record Midwest drought of 1988 changed relative precipitation but did not create any new areas of precipitation and concluded that a sudden increase in soil moisture would not have stopped the drought. When simulating the record Midwest floods of 1993 they found that the saturated surface significantly contributed to the total rainfall. Their conclusion was that local recycling of water is more important during times of extreme wetness than during drought. On the other hand, *Giorgi et al.* [1996] concluded that local recycling of evaporated water was *not* important as compared to large scale moisture fluxes and synoptic activity during the drought of 1988 and the floods of 1993. Furthermore, they found that the main effect of decreased evaporation is to increase buoyancy and sustain convection. In other words, there is a *negative* feedback between soil moisture and precipitation. *Trenberth* *and Guillemot* [1996] postulated that although the 1988 drought and 1993 floods were initiated by large scale sea surface temperature and atmospheric circulation anomalies (La Niña in 1988, El Niño in 1993), soil moisture acted to amplify and prolong the wet and dry conditions. In contrast to *Pan et al.* [1995], *Dirmeyer and Brubaker* [1999] examined the transport and surface sources of moisture supplying precipitation over the United States during the drought of 1988 and floods of 1993 and found that 41% of the precipitation in the Mississippi River Basin originated locally in 1988 compare to only 33% in 1993. During the peak of flooding in July 1993, the precipitation – soil moisture recycling ratio was considerably lower than other months that year. The main source of moisture was the Gulf of Mexico and Caribbean. In 1988, during the peak of the drought in June the recycling ratio was maximum, implying that soil moisture played an important role in the persistence of the drought.

From these studies it is clear that soil moisture has a significant effect on climate, although the exact nature of its effect has yet to be determined. Figure 1.7 graphically illustrates the effect current soil moisture (SM) conditions have on the weather predictions of one particular model, the NASA Goddard GCM [personal communication, Suarez et al., 2001] and [*Entekhabi et al.*, 1999]. Map A displays the observed difference in precipitation over the United States during the summer of 1993 (the record flood year in the Midwest) and the summer of 1988 (the record drought year). Notice the large difference in precipitation over the Midwest. Map D shows the difference in forecasted precipitation during the summers of 1993 and 1988 using information that would have been available at that time. This particular retrospective forecast was not very accurate, particularly in the Midwest. It was made using satellite measurements of sea surface temperature (SST) observed in 1988 and 1993 and climatic (expected for that region and time of year) soil moisture conditions. Maps B and C show precipitation analysis made using more realistic measurements of the current soil moisture state in 1988 and 1993, created with observed precipitation records and a simple water balance model. Clearly, knowledge of current soil moisture conditions

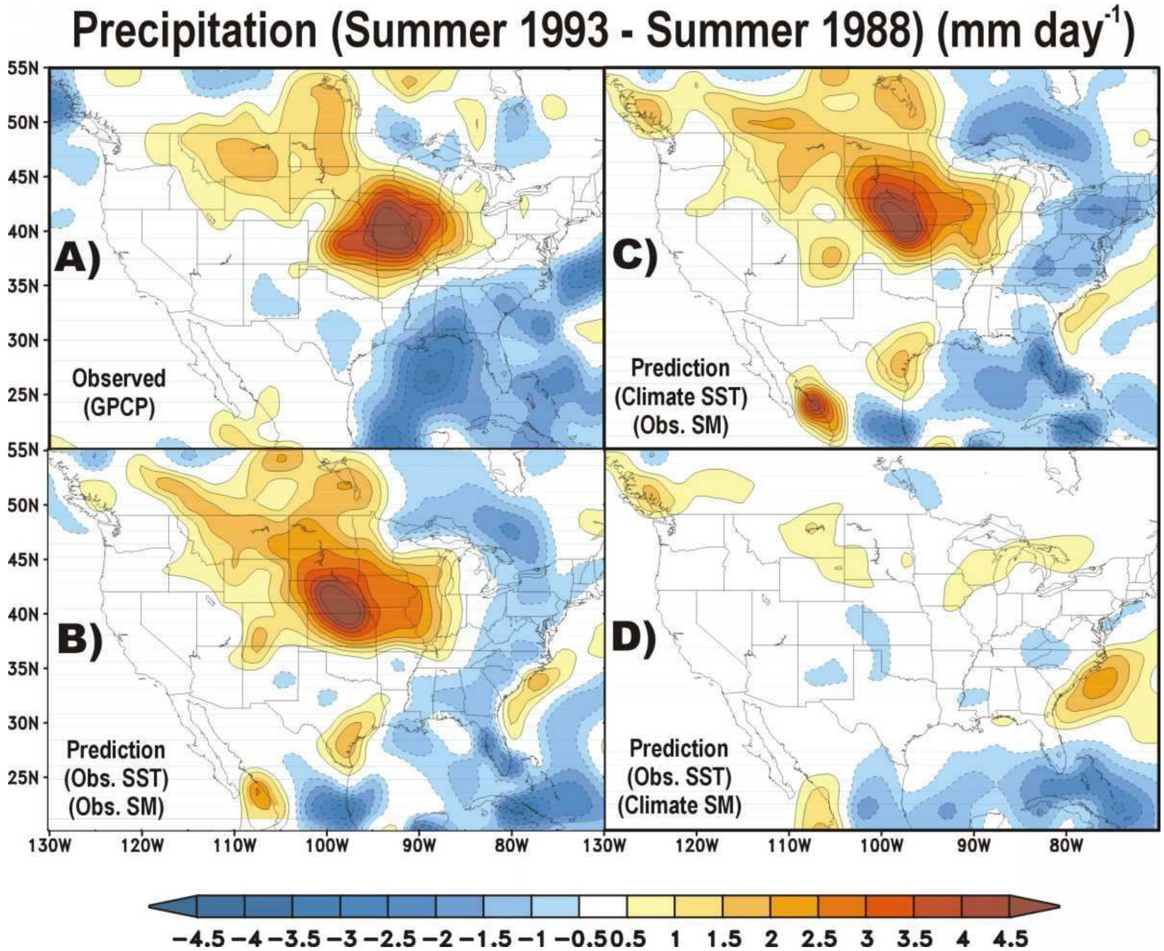

Figure 1.7: Difference in precipitation over the United States between the summer of 1993 and the summer of 1988 [Suarez, Schubert, and Chang, personal communication, 2001]. Also cited in *Entekhabi et al.* [1999].

improved the retrospective forecasts. In map B, observations of sea surface temperature were used in the analysis, while in C, climatic values of sea surface temperature were used.

1.5 Soil–Vegetation–Atmosphere Transfer

Much of the uncertainty and conflicting results among GCMs can be explained by the difficulty in modeling land–atmosphere interaction [*Roads and Betts*, 2000]. In a GCM, transport of moisture and energy within and between the soil, vegetation, and atmosphere is described by a *soil–vegetation–atmosphere transfer (SVAT) model*. How water is taken up by roots, the extent of the root system, evaporation from the soil, how efficiently the

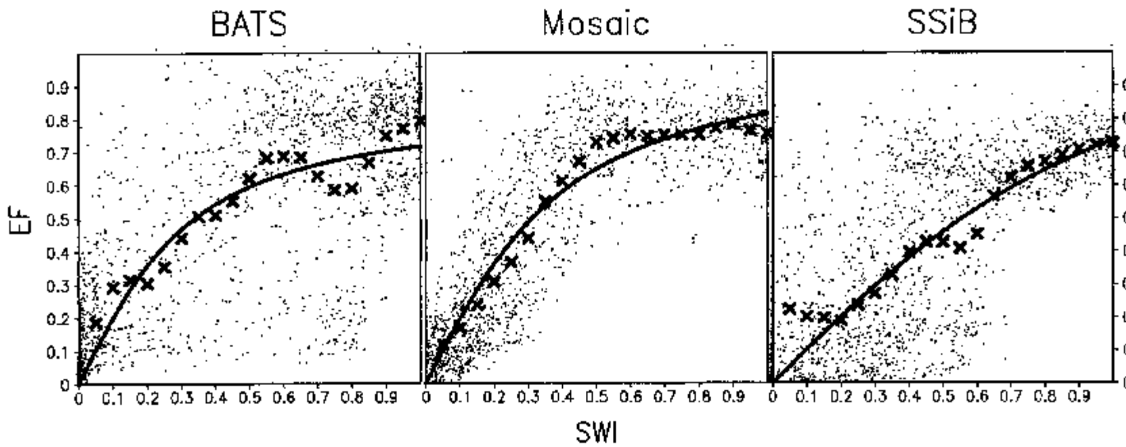

Figure 1.8: Evaporative fraction (EF) versus soil water index (SWI) for three different SVAT models each driven with the same data. From *Dirmeyer et al.* [2000].

vegetation can transpire, and radiative energy balance are just some of the processes that SVAT models intend to replicate. Although these models are very sophisticated in most cases, they can not possibly address all of the physical processes they attempt to represent [*Beljaars and Viterbo*, 1999]. As a result, individual models consistently disagree with each other, even when driven by the same weather [*Schulz et al.*, 1998; *Anderson et al.*, 1999; *Pitman et al.*, 1999; *Dirmeyer et al.*, 2000; *Roads and Betts*, 2000].

For example, Figure 1.8 shows a scatter plot of evaporative fraction (EF), the ratio of latent heat flux to the sum of sensible and latent heat fluxes, versus soil water index (SWI), the ratio of the difference between the water content of the soil and the wilting point to the difference between field capacity and wilting point for the uppermost soil layer near the surface. Typically, $0 < \text{SWI} < 1$, where SWI = 0 is soil moisture at the wilting point and SWI = 1 represents soil moisture at field capacity. The points represent all land grid cells in the Northern Hemisphere covered by grass or shrubs. Each SVAT model (BATS, Mosaic, and SSiB) uses the same data from July 1987 and July 1988. The X's represent the mean of each SWI bin of width 0.05, and the thick curve is the best-fit line of the X's [*Dirmeyer et al.*, 2000].

Although each SVAT model was forced with the same data, some differences exist between the three models due to their different representations of the associated physical processes. For all the models, the same general relationship between EF and SWI exists: as the soil gets wetter (SWI increases) more of the energy is transferred to the atmosphere via latent heat flux than sensible heat flux. In wet soil, part of the absorbed net radiation is used by the vegetation to transpire and to evaporate the soil water. This cools the soil, reducing the amount of sensible heat transfer that can occur. Unlike more substantial vegetation such as trees that have larger root systems and can pull water from deeper soil layers, the water available to the atmosphere in grass and shrubs is a strong function of the water content of the uppermost soil layers. BATS and Mosaic allow EF to be very large and in some cases to saturate (no sensible heat flux). In SSiB, EF values are rarely above 0.8. On the other hand, SSiB and Mosaic do not allow low values of EF when the soil is very wet (SWI close to 1) while BATS does allow a wide range of EF to occur even when the soil is very wet. These discrepancies are caused by the peculiarities of each model. Sensible heat flux is never absent in SSiB, while it appears BATS does not allow the soil albedo, and hence net radiation, to change much when wet, allowing EF to be low.

1.6 Microwave Radiometry

Microwave radiometry, or passive microwave remote sensing, offers a unique opportunity to improve modeling of land–atmosphere interaction. Microwave radiometry is the measurement of the naturally emitted electromagnetic radiation at microwave wavelengths (Figure 1.9). Because the amount of emitted microwave radiation depends greatly on the presence of liquid water, it can be used to measure *near–surface soil moisture*, the amount of water in the first few centimeters of the earth's surface [*Schmugge et al.*, 1974; *Eagleman and Lin*, 1976; *Njoku and Kong*, 1977; *Newton*, 1977].

Unfortunately, the amount of water available to the atmosphere is determined both by the surface wetness and by the rooting depth of the vegetation, which can be more than a meter in depth. Two recent breakthroughs have made it possible to determine this *plant–*

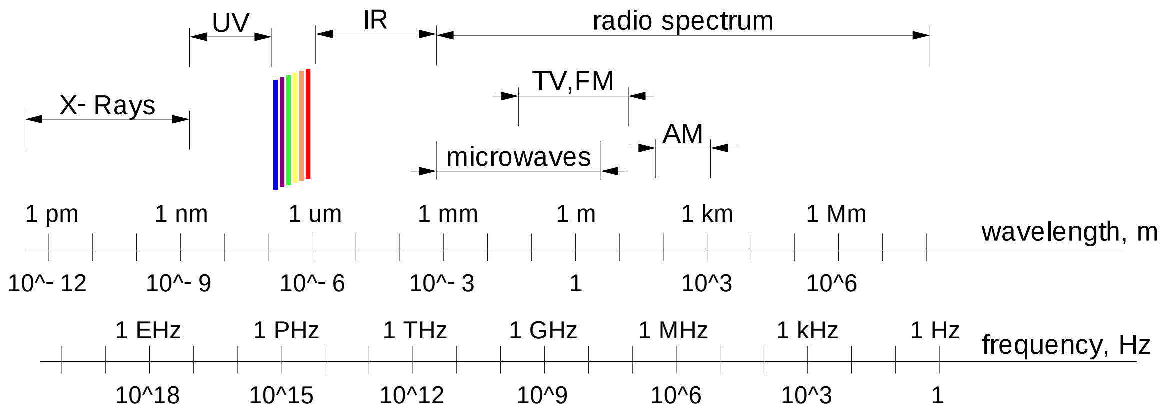

Figure 1.9: The electromagnetic spectrum. Visible wavelengths lie between the ultraviolet (UV) and the infrared (IR). Drawn by the author.

available water and the associated flux of moisture and energy at the land surface on a global scale.

First, it has been recognized that estimates of plant–available water can be improved with a temporal record of near–surface soil moisture as long as the observation intervals are less than the moisture retention period of the surface soil layer [*Mahfouf*, 1991; *Calvet et al.*, 1998; *Wigneron et al.*, 1999; *Calvet and Noilhan*, 2000]. Data assimilation techniques have been developed to directly assimilate observed microwave brightness into SVAT models to improve their estimates of soil moisture and temperature [*Houser et al.*, 1998] using both Kalman filter methods [*Entekhabi et al.*, 1994; *Galantowicz et al.*, 1999] and variational assimilation [*Reichle et al.*, 2001]. Second, new technologies such as Synthetic Thinned–Array Radiometry (STAR) [*Swift et al.*, 1991; *Le Vine et al.*, 1994; *Le Vine*, 1999] and Direct–Sampling Digital Radiometry (DSDR) [*Fischman and England*, 1999] have made it feasible to build satellite radiometers that have useful spatial resolution at the optimal soil moisture remote sensing frequency of 1.4 GHz ($\lambda = 21$ cm) by reducing antenna size and weight, as well as overall complexity and power requirements.

Within the next several years, the ability to monitor soil moisture globally will drastically improve. Currently, the Special Sensor Microwave Imager (SSM/I) series of defense satellites carry the most useful microwave radiometers which operate at a frequency of 19 GHz ($\lambda = 1.6$ cm). Unfortunately their ability to "see" soil moisture is weak because of their short wavelength. In the summer of 2002, NASA and the Japanese space agency (NASDA) launched EOS Aqua and ADEOS-II, respectively. Both satellites carry a 6.9 GHz ($\lambda = 4.3$ cm) radiometer as part of the Advanced Microwave Scanning Radiometer (AMSR) system. At this longer wavelength, vegetation is less opaque. Both NASA and the European Space Agency (ESA) have plans to launch 1.4 GHz ($\lambda = 21$ cm) satellite radiometers later this decade in 2006 and 2005, respectively. In order to take advantage of these opportunities, reliable models of land surface brightness need to be developed.

1.6.1 Physical Basis

All matter naturally emits electromagnetic energy. Matter is composed of atoms that are constantly in motion as long as the temperature is above absolute zero. The atoms themselves are composed of charged particles. An accelerating electric charge must emit electromagnetic energy. *Brightness*, B, is the power emitted per unit area, per unit solid angle. According to the Planck Law,

$$B_f(f) = \frac{2hf^3/c^2}{\exp(hf/kT) - 1} \tag{1.5}$$

where $B_f(f)$ is the spectral brightness (units of W m^{-2} sr^{-1} Hz^{-1}), h is the Planck constant ($= 6.63 \times 10^{-34}$ J s), f is the frequency, c the speed of light ($\approx 3 \times 10^8$ m s^{-1}), k is the Boltzmann constant ($= 1.38 \times 10^{-23}$ J K^{-1}), and T is the temperature in Kelvin A *radiometer* measures the brightness captured by its antenna. Essentially, a radiometer is a very sensitive AM radio receiver.

As temperature increases, atoms move more quickly and radiate more energy. Emitted brightness is determined by the electromagnetic properties of an object. When brightness encounters a boundary between two media with different electromagnetic properties, part of the incident brightness is reflected back into the original medium, and the rest is transmitted into the second medium. Hence electromagnetic properties (specifically permittivity, permeability, and conductivity) determine the emitted brightness. It is also important to note that these properties are frequency dependent.

Take for example a radiometer measuring the brightness of moist soil. At low frequencies, moist soil and air have very different electrical properties because of water's high permittivity. Hence the power emitted from a moist soil halfspace is much less than the power emitted from a dry soil halfspace whose electrical properties are more similar to air. In the first case, more of the brightness is reflected back into the soil and less is transmitted. As the water content decreases, the electromagnetic contrast between the soil and the air decreases and the soil appears brighter. At higher frequencies, water no longer has a high permittivity and hence the brightness of wet and dry soil are very similar. If two objects are at the same temperature, the object with a higher *emissivity* is brighter. A *blackbody* is a perfect emitter (no reflection occurs at the surface boundary) and has an emissivity of unity. A highly polished metal surface can have an emissivity close to zero.

1.6.2 Brightness Temperature

If $hf/kT << 1$, then $\exp(hf/kT) - 1 \approx hf/kT$ and (1.5) simplifies to

$$B = \frac{2k}{\lambda^2} T \tag{1.6}$$

where λ is the free–space wavelength and a small but finite range of frequencies sampled has been assumed. This is called the Rayleigh–Jeans Law and it is valid for low frequencies ($<$ 100 GHz, most of the microwave region) and naturally–occurring temperatures in Earth's environment.

Since Planck Law radiation is completely unpolarized, half of the brightness is horizontally–polarized and half is vertically–polarized. Hence

$$B_p = \frac{1}{2} \times B = \frac{k}{\lambda^2} T \tag{1.7}$$

where B_p is the p–polarized brightness. Because the magnitude of brightness is so small and nonsensical ($\approx 10^{-18}$ W m^{-2} sr^{-1} at microwave wavelengths), the p–polarized brightness is normally represented by a *brightness temperature*, T_B. The brightness temperature corresponds to the thermometric temperature of a blackbody radiator that would produce the same p–polarized brightness:

$$B_p = \frac{k}{\lambda^2} T_B \tag{1.8}$$

where the subscript p has been deleted on the brightness temperature because polarization dependence is assumed. The brightness temperature has units of Kelvin and gives a better sense of whether objects are "cold" (have a low temperature and/or low emissivity) or "hot" (high temperature and/or high emissivity). For an object with a uniform temperature, its emissivity is then the ratio of its brightness temperature to its thermometric temperature:

$$e = T_B/T. \tag{1.9}$$

For objects in thermal equilibrium with their surroundings,

$$e = 1 - R \tag{1.10}$$

where R is the reflectivity of the interface.

1.6.3 Why Microwaves?

The emissivities of most natural surfaces do not vary greatly at infrared wavelengths. On the other hand, microwave emissivity is strongly dependent upon the composition and structure of the surface or volume under observation. Specifically, microwave emissivities vary strongly with surface roughness, internal structure, polarization, look–angle [*England and Johnson*, 1977], and particularly *water content* due to liquid water's high permittivity at microwave frequencies. It is precisely liquid water's distinct electromagnetic properties that make microwave remote sensing sensitive to the water content of soil and vegetation. Because of their longer wavelength, microwaves penetrate vegetation and soil in contrast to high–frequency optical and infrared radiation. As a result, modest vegetation is semi–transparent and the soil beneath the canopy is "visible" to a microwave radiometer. Microwaves, unlike optical and infrared radiation, also have the ability to penetrate clouds (including ice clouds) and, to some extent, rain [*Ulaby et al.*, 1981-1986].

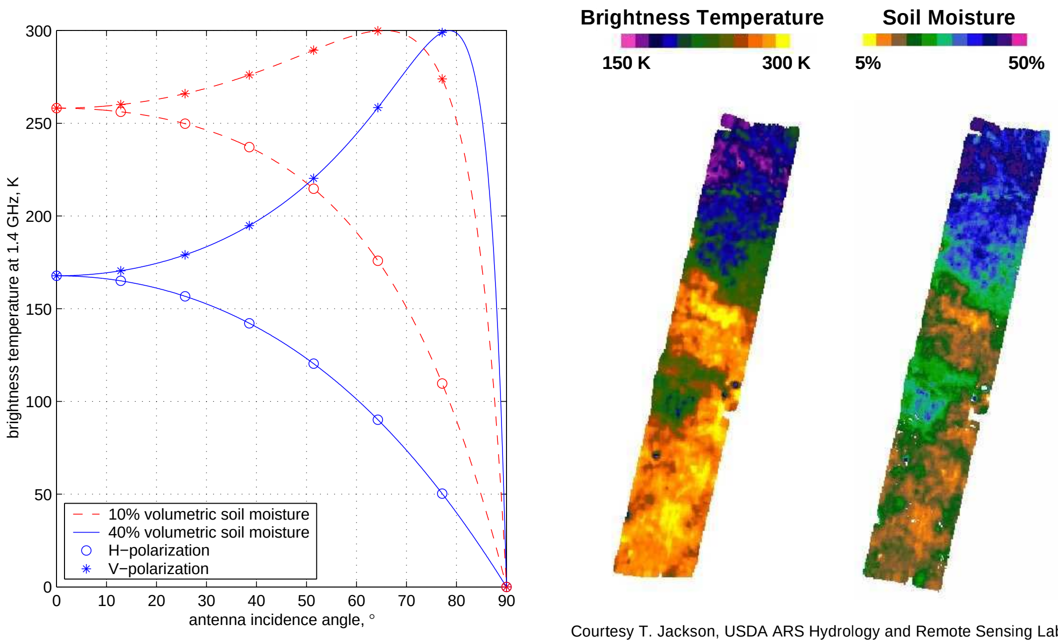

Figure 1.10: At left, the horizontally– and vertically–polarized brightness temperature of a smooth bare soil surface as a function of incidence angle for wet and dry soil. At right, an example of a soil moisture map derived from a map of brightness temperature.

The graph at left in Figure 1.10 illustrates the effects of polarization, look–angle, and moisture content on the microwave brightness of a smooth bare soil surface. Note the Brewster angle at vertical polarization, the angle at which $R = 0$ and $e = 1$. Horizontal polarization is preferred since the difference in brightness between wet and dry soil is maintained out to large incidence angles. This difference in brightness (≈ 100 K) is large in relation to the precision of typical microwave radiometer (< 1 K) and results in an excellent signal–to–noise ratio. Theoretically, changes in soil moisture of less than 1% can be measured. At right in Figure 1.10 is an example of a soil moisture map made using an airplane microwave radiometer. Note how cold brightness temperatures correspond to wet areas.

The depth to which radiometry is sensitive to soil moisture scales with wavelength. At 1.4 GHz ($\lambda = 21$ cm), there is sensitivity to the first 4 to 5 cm, while at 19 GHz ($\lambda = 1.6$ cm), there is sensitivity only to the first few millimeters. This “emitting depth” can change depending on how sharply the soil constitutive properties vary with depth. Instead,

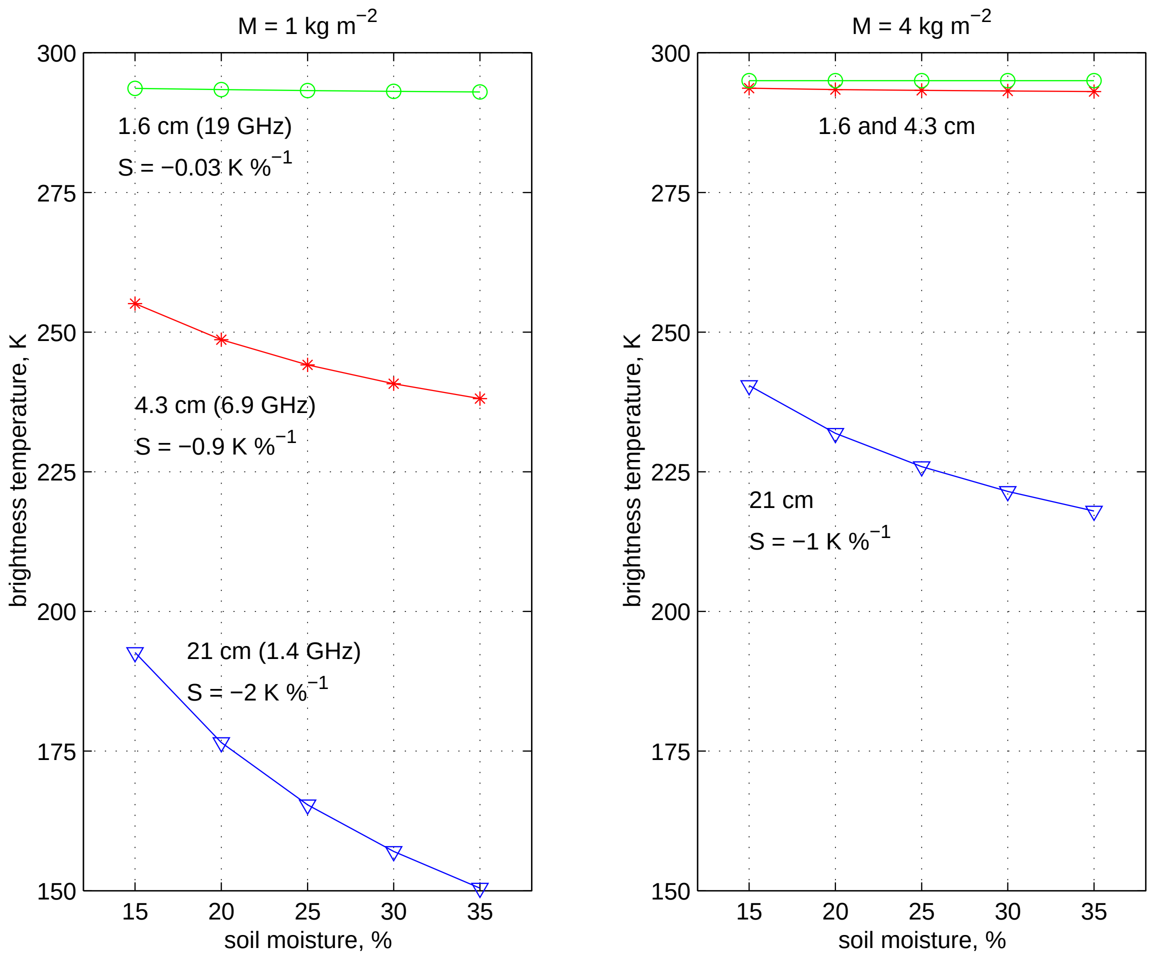

Figure 1.11: Modeled brightness temperature as a function of volumetric soil moisture at three different wavelengths, for vegetation column densities of $M = 1$ and 4 kg m^{-2} for an ideal, nonscattering canopy. The soil is treated as a uniform halfspace, and soil and vegetation temperature is 295 K. S is the sensitivity of brightness to soil moisture.

it is more useful to speak of the *impedance match* between the soil and the air, i.e. how reflective the soil surface is. At 1.4 GHz, this reflectivity is sometimes determined by only the first centimeter when the soil moisture profile is sharp (very wet just at the surface) [*Jackson et al.*, 1998]. On the other hand, when the soil is very dry and the moisture profile is uniform, the reflectivity can depend on the first several centimeters [*Schmugge and Choudhury*, 1981].

1.6.4 Effect of Vegetation

At microwave frequencies, the brightness of a vegetated surface is determined by both the state of the canopy and the underlying soil. The vegetation type, stage of growth, density, temperature, and moisture content, as well as the soil water content, soil type, roughness, and temperature are all important factors. When the canopy has a sufficiently low column density, microwave brightness is most sensitive to soil water content [*Schmugge*, 1978; *Newton and Rouse*, 1980; *Wang et al.*, 1980b; *Jackson et al.*, 1982; *Ulaby et al.*, 1983]. At higher column densities, vegetation gradually becomes opaque until no sensitivity to soil moisture can be seen.

The two graphs in Figure 1.11 illustrate the effect of vegetation column density on the relationship between brightness temperature and soil water content at three different microwave wavelengths. Vegetation column density, M, is the integrated vertical mass of vegetation matter per unit horizontal area. For a column density of $M = 1$ kg m^{-2} equivalent to a 30 cm high corn crop, there is little sensitivity at $\lambda = 1.6$ cm, while at $\lambda = 4.3$ and 21 cm there is approximately a 1 and 2 K change per volume percent soil moisture, respectively. At a column density of $M = 4$ kg m^{-2} equivalent to a 1.5 m corn crop, only radiation at $\lambda = 21$ cm (1.4 GHz) shows any change with soil moisture.

As the wavelength increases, microwave brightness originating from the soil suffers less attenuation by vegetation. At short wavelengths, the canopy effectively becomes infinitely thick even at modest levels of column density. At 1.4 GHz, the vegetation column density at which there is no longer practical sensitivity to soil moisture appears to be about 8 kg m^{-2} (equivalent to a dense, mature corn canopy) [*Wang et al.*, 1984], while at a higher frequency such as 6.9 GHz, the limit is at most half as much. Longer wavelengths are also preferred because they are less susceptible to soil surface roughness and soil and canopy heterogeneity. The challenge at long wavelengths is to construct satellite instruments that effectively balance size and weight restrictions with footprint size (spatial resolution). New technology mentioned previously promises to make these types of satellites possible.

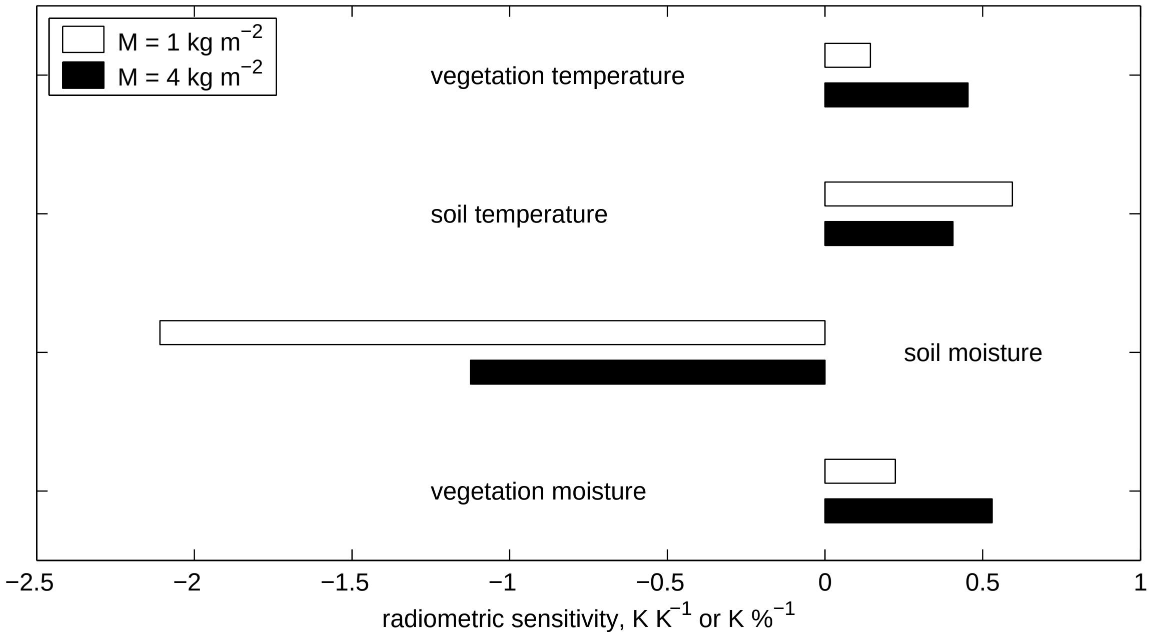

Figure 1.12: Radiometric sensitivity to vegetation temperature, soil temperature, soil moisture, and vegetation moisture for an ideal, nonscattering canopy at 1.4 GHz.

Anticipating forthcoming satellite radiometers at 1.4 GHz, much work has been done at this frequency with ground–based and airplane instruments within the last two decades. Although the response to changes in soil water content has been well documented, there are still many questions about the effect of the overlying vegetation. Besides column density, are there other canopy properties that can significantly affect the microwave brightness? Figure 1.12 displays the 1.4 GHz radiometric sensitivity to soil moisture along with sensitivity to soil temperature, vegetation temperature, and vegetation moisture as predicted by a zero–order radiative transfer model. Note that brightness *decreases* as soil moisture increases, while the other changes tend to *increase* the brightness. At low vegetation column densities, sensitivity to soil moisture dominates. For $M = 1$ kg m^{-2}, soil moisture sensitivity is ≈ -2 K per volume percent, as illustrated in Figure 1.11. As the column density increases, the radiometric sensitivity to soil temperature and vegetation temperature and moisture become comparable to soil moisture sensitivity.

In the past, changes within the canopy, both in temperature and moisture content, have been assumed to be small. Can these changes be neglected? At higher column densities

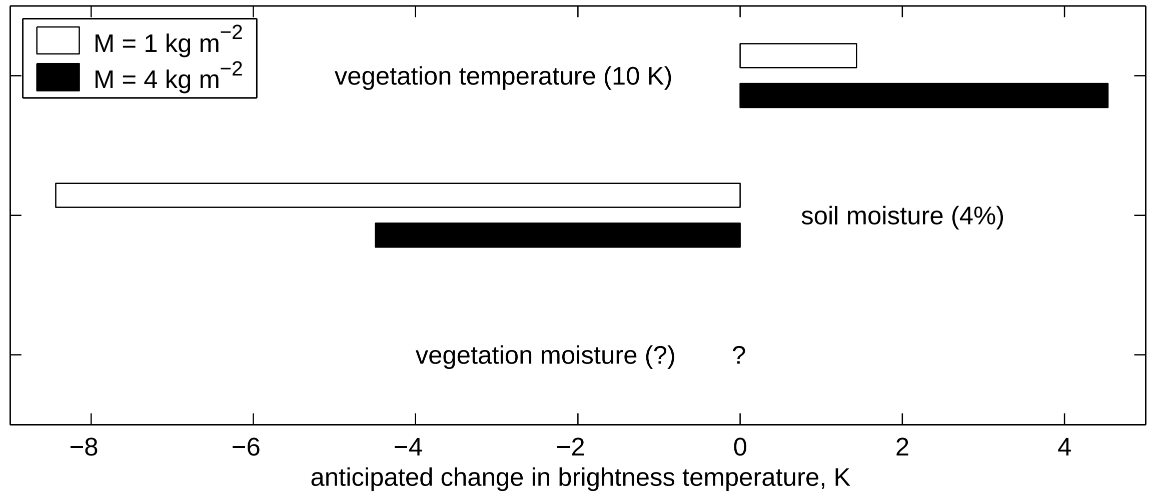

Figure 1.13: Anticipated change in 1.4 GHz brightness temperature in response to changes in vegetation temperature (10 K variation in diurnal cycle) and soil moisture (desire sensitivity to 4%) in a nonscattering canopy. Expected change in vegetation moisture not known.

when the soil moisture sensitivity is small but still measurable, these other factors will have competing influences. Figure 1.13 shows the expected change in 1.4 GHz brightness temperature given expected changes in vegetation temperature (assuming a typical diurnal variation of 10 K) and desired soil moisture sensitivity (to $\approx$ 4% by volume). At $M =$ 4 kg m^{-2}, these changes are almost equal in magnitude.

What is not immediately known is what changes in vegetation water content can be expected and thus the corresponding change in brightness. Furthermore, are the predictions of the zero–order radiative transfer model, suitable for a nonscattering canopy, representative of what may happen in a canopy such as corn where scattering may be significant? These are some of several questions this dissertation seeks to answer:

- *Can scattering of radiation within a corn canopy be neglected at 1.4 GHz?* The most widely used model for land surface microwave brightness (the zero–order radiative transfer model) assumes negligible scattering, but it has only been validated at steep angles of incidence at which the vegetation has the least impact.

- *At what level of vegetation column density is there no longer any useful sensitivity to changes in soil water content in a corn canopy?* Does the transparency of a general canopy depend on simply the amount of vegetation or water in the canopy or also on its distribution?

- *What effect do changes in vegetation water content have upon the emitted microwave radiation?* These variations can be caused by intercepted precipitation and dew, or by slower, more subtle processes such as diurnal variations, senescence, and plant response to drought or extreme wetness. Are these changes the same in both scattering and nonscattering canopies?

1.7 Format of Dissertation

The second chapter of this dissertation describes experiments during which radiometric and micro–meteorological data were collected in a field of corn, and the instruments used to collect these data. The third chapter discusses the electromagnetic properties of a corn canopy in terms of the nature of absorption, emission, and scattering. It also determines whether the zero–order radiative transfer model is suitable for scattering canopies such as field corn. A new zero–order model is formulated. The fourth chapter compares the new model with observations. It then examines the effect of changes in canopy water content on the microwave brightness of field corn, due to intercepted precipitation and dew. Finally, the sensitivity to soil moisture in field corn observed in this and other investigations is presented. The competing effects of vegetation temperature and moisture and soil moisture are also detailed for both a scattering canopy such as field corn and a hypothetical nonscattering canopy such as thick grass. Finally, the fifth chapter discusses the contributions of this thesis to the general body of research, and future work in this subject area.

CHAPTER 2

The Eighth Radiobrightness and Energy Balance Experiment

The Eighth Radiobrightness and Energy Balance EXperiment (REBEX–8) was conducted by members of the Microwave Geophysics Group at the University of Michigan during 2001. The goal of the experiment was to record simultaneous, long time–series measurements of microwave brightness, soil moisture, and relevant micrometeorology on the plot scale, at several different stages of growth and under various environmental conditions in a "complex" vegetation canopy. A complex canopy is loosely defined as one that contains significant small–scale heterogeneity in the form of different canopy components, such that scattering may be important at microwave wavelengths. The particular canopy observed in REBEX–8 was a field corn canopy. The plot scale is defined as an area on the order of 10^2 m^2, which lies between a scale encompassing the entire field (order 10^6 m^2) and fine–scale field variations such as tilled row structure (order 10^0 m^2). Radiometer footprints varied from approximately 20 to 40 m^2, depending on the incidence angle, and encompassed several rows.

This approach to studying land surface microwave brightness is seldom used. Traditional remote sensing studies attempt to replicate satellite measurements, in which discrete measurements of brightness are made only once every one to three days. Continuous measurements of brightness, micrometeorology, and soil state allow the integration of many types of observations with models of land–atmosphere interaction and microwave bright-

Figure 2.1: Truck–mounted radiometers and micrometeorological station on day of year 144, looking southeast.

ness. Together, they can be used to tease out many subtle, yet important physical properties that might otherwise be hard to find, much like using the context of a sentence to decipher an unknown word as opposed to only examining the word itself.

The experimental site, an 800 (E–W) by 400 m (N–S) privately–owned corn field under conventional tillage and crop rotation, was located in Southeastern Michigan approximately 40 km south and west of North Campus of the University of Michigan. The site was unusually flat and uniform in terms of soil properties and vegetation. See Figure 2.1 for a picture of the site and equipment in late May. The soil at the site was a silty clay loam of the Lenawee series. Soil texture was measured by the Kansas State University Agronomy Department's Soil Testing Laboratory and found to be 16.1% sand, 55.0% silt, 28.9% clay for the first 10 cm soil layer, with slightly less than 2% total carbon. Average row spacing was 0.77 m. Plant density was 7.49 m^{-2}. Rows were planted E–W.

Five distinct experiments of one to four days each were conducted at different times during the spring, summer, and fall to observe different stages of vegetation growth. Table 2.1 describes the vegetation conditions during each REBEX and a labeling convention. The field was planted on April 29 and 30 (day of year 119 and 120) and harvested on October 17 and 18 (day of year 290 and 291). Between REBEX–8 and REBEX–8x1, all equipment was removed from the field to accommodate cultivation on June 11 and 12 (days of year 162 and 163). After June 25 (day of year 176) the fraction of vegetation cover was unity. The experiments after cultivation are collectively referred to as REBEX–8x. Measurements of microwave brightness were only measured during each experimental period. Micrometeorology was measured continuously from the middle of May through the middle of October, save for the cultivation period.

Leaf–area index (LAI) and vegetation and water column densities were measured periodically throughout the summer. Each LAI value was computed from the average of ten samples taken at random locations separated by 5 to 10 m within the field. Each sample made use of one above–canopy measurement and the average of three below–canopy measurements of the incident radiation. Below–canopy measurements were made in the row, and one–third and two–thirds of the way across the row space. The wet and dry masses of six randomly chosen plants were averaged to compute column densities. Each plant was separated by component (stem, leaves, and ear). Samples were placed in paper bags and dried in a 70 °C oven for 7 days.

REBEX–7, a supporting field experiment, was conducted the previous summer in a field of corn 1 km north of the REBEX–8 site. This field had nearly identical topography

Table 2.1: REBEX information. Date information includes days of year. *GS* refers to vegetation growth stage. *H* is vegetation height in meters. *M* is vegetation column density in kg m^{-2}. M_w is water column density in kg m^{-2}. *LAI* is leaf area index in m^2 m^{-2}.

	Dates	*GS*	*H*	*M*	M_w	*LAI*
REBEX–8	May 23-25 (143-145)	effectively bare soil	0.2	0.3	0.3	0.1
REBEX–8x1	July 4 (185)	growing	1.8	4.8	4.3	3.2
REBEX–8x2	July 11-13 (192-194)	growing	2.2	5.7	5.0	4.0
REBEX–8x3	Aug 17-20 (229-232)	mature	3.0	8.0	6.3	4.8
REBEX–8x4	Oct 10 (283)	senescent	2.8	4.9	2.7	2.5

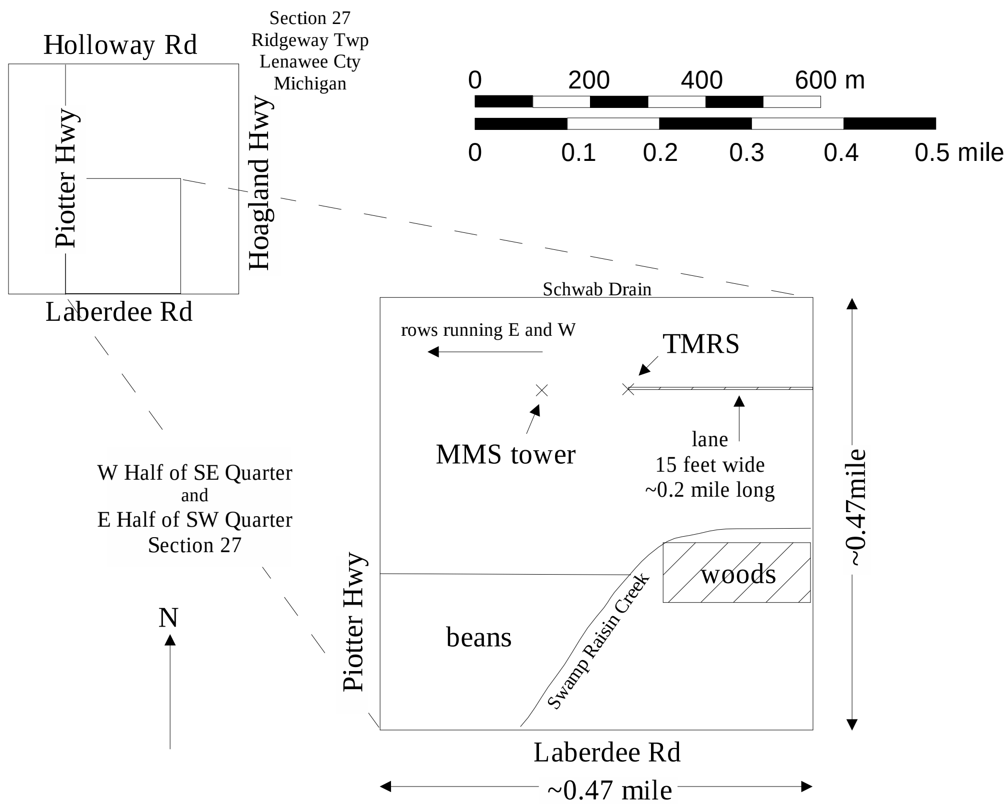

Figure 2.2: Map of REBEX–8 and –8x site. Truck–mounted radiometers (TMRS) and Micro–meteorological station (MMS) marked.

and soil and vegetation properties. The same implements and procedures were used to plant and cultivate the corn. Many of the same measurements made in REBEX–8 were also made the previous summer in REBEX–7.

2.1 Microwave Radiometers

Two 1.4 GHz radiometers, oriented to record horizontally–polarized (H–pol) and vertically–polarized (V–pol) brightness, were mounted on the hydraulic arm of a truck. The arm, along with a rotator at the end of the arm, made it possible to change both the incidence angle, θ, and the azimuthal angle, ϕ, at which the radiometers received radiation. Azimuthal angle was measured with respect to row direction, with $\phi = 0°$ parallel to the row direction. Antennae E– and H–plane half–power beamwidths were approximately 21°. Side lobe levels were below -20 dB. Terrain brightness was measured at two–minute intervals. The truck was positioned within the field at the head of a "lane", a portion of the field that was not planted. The lane, 6 rows wide and approximately 250 m long, began at the eastern edge of the field and continued west. The antenna footprints were located at the head of the lane, to the west ($\phi = 0°$) and to the south ($\phi = 90°$). See Figure 2.2 for a map of the site.

Due to the radiometer fabrication schedule, only one radiometer was available during REBEX–8. It was oriented to measure H–pol 1.4 GHz brightness. Both radiometers were deployed for all subsequent field experiments. Unknown equipment problems with the H–pol radiometer contaminated many data and only H–pol brightness measurements during REBEX–8x3 and –8x4 were usable. Measurements of V–pol 1.4 GHz brightness were successfully made during REBEX–8x1, –8x2, –8x3, and –8x4.

2.1.1 Direct–Sampling Digital Radiometer (DSDR)

The input signal to a radiometer is the time–varying antenna voltage associated with the intercepted power. This voltage signal is essentially random noise and can be described by a zero–mean Gaussian (normal) probability distribution. In particular, the amplitude of the voltage is normally distributed, while the envelope is Rayleigh distributed. Since power is directly proportional to the square of the voltage, the expected value of the power (or power estimate) is proportional to the expected value of the square of the voltage, also known as the voltage's variance. The corresponding power has an exponential distribution. The average power is equal to the standard deviation of a single measurements of power.

A traditional radiometer (one with a superheterodyne receiver) uses a mixer to down–convert the high frequency input signal. A Direct–Sampling Digital Radiometer (DSDR) [*Fischman*, 2001], on the other hand, employs a fast A/D converter to sub–harmonically sample (and effectively down–convert) the input voltage signal. Subsequent digital hardware then operates on the signal (which is now just a stream of numbers) to measure the input power. The output of a DSDR is a single number that is the average of N samples of the square of the quantized voltage signal, $Q[v(t_n)]^2$, sampled at time t_n. It is called the r_Q

value:

$$r_Q = \frac{1}{N}\sum_{n=1}^{N} Q[v(t_n)]^2. \tag{2.1}$$

The r_Q value is simply a time–limited estimate of the variance of the quantized voltage, which is an estimate of the power captured by the radiometer's antenna as discussed earlier.

The A/D converter must have a minimum number of quantization levels within the input signal voltage range in order to measure its power. This is determined using a parameter called the normalized signal strength, s, defined as the standard deviation of the input signal, σ, normalized by the discretization step size (quantization voltage), v_o, of the A/D converter:

$$s = \sigma/v_o. \tag{2.2}$$

The radiometers deployed in REBEX–8 and –8x used SPT7610 flash A/D converters manufactured by Signal Processing Technologies (Colorado Springs, Colorado). Their small–signal bandwidth was 1.4 GHz and their discretization step size was $v_o = 1$ V / 2^6 bits $= 15.625$ mV bit^{-1}. Small–signal bandwidth is defined by the manufacturer as the frequency at which the sampler and digitizer attenuate the input signal by 3 dB when the input signal is 20 dB below the full-scale input range of the A/D converter. Since the full–scale input range is 1 V, the small-signal input signal would be 100 mV. When attenuated by 3 dB, the resulting signal is approximately 71 mV. Dividing by the discretization step size gives the effective number of digitization levels within the small–signal bandwidth around 1.4 GHz:

$$71 \text{ mV}/15.625 \text{ mV} = 4.5 \text{ levels}. \tag{2.3}$$

Since the effective range of a Gaussian signal is $\approx 6\sigma$, the 4.5 levels must span $6s$ and therefore:

$$6s = 4.5, \quad s = 4.5/6 = 0.75. \tag{2.4}$$

Hence these A/D converters satisfy the large signal approximation of $s > 2/3$ as defined by *Fischman* [2001]. When this condition is satisfied, the difference between an r_Q value obtained with a ideal A/D converter of infinite resolution and the r_Q value from a real A/D converter has reached a constant value of ${v_o}^2/12$. In reality, $r_Q/{v_o}^2$ is what is actually recorded in a DSDR output data file. To correct for the noise introduced by the quantization process, $1/12$, was subtracted from a DSDR output.

2.1.2 DSDR Precision

Accuracy is a measure of how close a measurement is to the real value. Precision is the closeness of agreement among several measurements of the same quantity. Precision can also be thought of as the reproducibility of a measurement or the sensitivity of the instrument in terms of the minimum detectable change. The accuracy of a radiometer's measurement of terrain brightness temperature depends on the calibration procedure and the radiometer's stability. Calibration accuracy is difficult to quantify and is discussed later. A radiometer's precision is commonly called its noise–equivalent sensitivity, or $NE\Delta T$. There are three main sources of noise which degrade the $NE\Delta T$ of a DSDR:

1. Random DC bias fluctuations in the A/D converter, ΔT_L;

2. The finite number of samples, ΔT_F;

3. Gain change due to random temperature fluctuations, ΔT_G.

Because these effects are independent,

$$NE\Delta T \approx \sqrt{{\Delta T_L}^2 + {\Delta T_F}^2 + {\Delta T_G}^2}. \tag{2.5}$$

Previously it was shown that the quantization process introduces a bias, but it can be removed easily. The A/D converter also introduces noise associated with random DC bias fluctuations. *Fischman* [2001] formulated an uncertainty function of a DSDR's digital correlator, $f_L(s)$, which describes the noise associated with DC bias fluctuations:

$$\Delta T_L = T_{sys} \frac{f_L(s)}{2\sqrt{3}s^2} \tag{2.6}$$

where T_{sys} is the noise temperature of the antenna and analog hardware before the A/D converter. For $s = 0.75$, $f_L(s)$ is approximately 6×10^{-5} (Figure 2.4 of *Fischman* [2001]). For a typical radiometer with T_{sys} of 400 K, $\Delta T_L \approx 0.01$ K.

Earlier the r_Q value was described as a time-limited estimate of the expected value. The actual expected value of a signal can only be found after an infinite number of samples have been recorded. The sensitivity contribution due to a finite sampling time is

$$\Delta T_F = \frac{T_{sys}}{\sqrt{N}} \tag{2.7}$$

where N is the number of independent samples of the incident brightness that are averaged together to determine the final measurement. $N = f_s \tau$, where the digital sample rate $f_s = 1/t_n$. In REBEX–8 and –8x, $f_s = 5$ MHz and $\tau \approx 1$ s, which yields $N = 5 \times 2^{20} \approx 5 \times 10^6$ samples. Accordingly, $\Delta T_F \approx 0.2$ K for a typical T_{sys} of 400 K.

Finally, the gain, G, of the amplifiers used to boost the antenna voltage to a measurable level is sensitive to changes in temperature:

$$\Delta T_G = T_{sys} \left| \frac{\Delta G}{G} \right| . \tag{2.8}$$

For the amplifiers used in REBEX–8 and –8x, $(G + \Delta G)/G = -0.06$ dB for every 1 °C change in the physical temperature of the amplifier. Hence,

$$\frac{\Delta G}{G} T_{sys} = \left(\frac{G + \Delta G}{G} - 1 \right) T_{sys} = -5.5 \text{ K }^{\circ}\text{C}^{-1} \tag{2.9}$$

for a typical T_{sys} of 400 K. Given an amplifier temperature fluctuation $\sigma_{amp} = 0.09$ °C, as measured during REBEX–8x4 (Figure 2.3), $\Delta T_G \approx 0.5$ K. The total DSDR sensitivity, according to (2.5) is then:

$$NE\Delta T \approx \sqrt{0.01^2 + 0.2^2 + 0.5^2} = 0.5 \text{ K}. \tag{2.10}$$

Figure 2.4 displays measured $NE\Delta T$ during REBEX–8x4. V–pol $NE\Delta T$ is slightly lower than 0.5 K. This may be because during this short observation interval, temperature fluctuations may have been lower than for the entire period (as illustrated by Figure 2.3

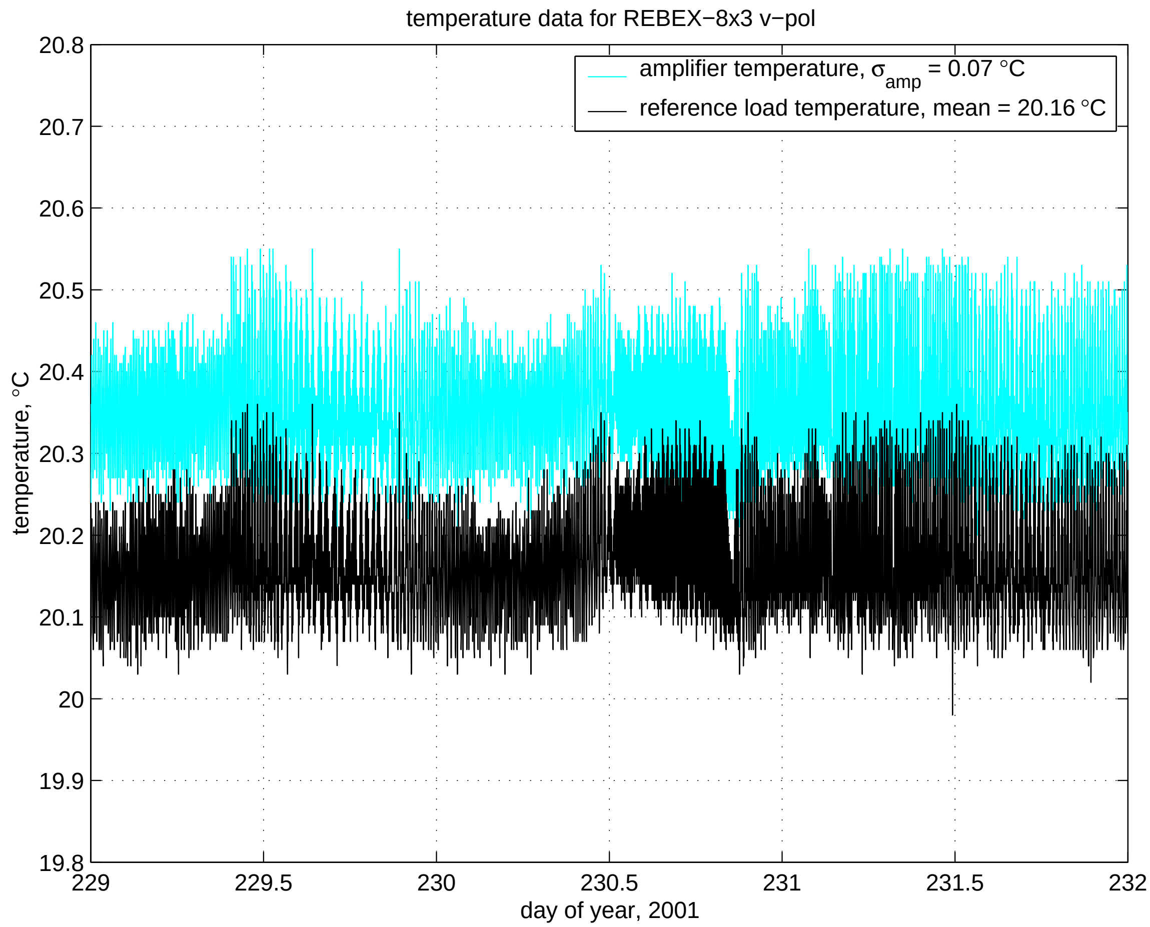

Figure 2.3: Amplifier and reference load temperatures for the V–pol DSDR during REBEX–8x3.

during REBEX–8x3). Actual V–pol DSDR T_{sys} may also have been lower than the rough estimate of 400 K, and may have changed over time. At H–pol, $NE\Delta T$ was considerably higher because of the poor temperature control experienced by the H–pol DSDR during REBEX–8x4 ($\sigma_{amp} \approx 0.3$ °C). Table 2.2 lists σ_{amp} for all REBEXs. Note that save for REBEX–8x4, σ_{amp} for both DSDRs was always < 0.1 K and $NE\Delta T$ was at most 0.5 K.

Table 2.2: Amplifier temperature variation, σ_{amp}, and approximate $NE\Delta T$ during REBEX–8 and –8x assuming $T_{sys} = 400$ K.

	R8 (H)	R8x1 (V)	R8x2 (V)	R8x3 (H, V)	R8x4 (H, V)
σ_{amp}, °C	0.06	0.08	0.07	0.08, 0.07	0.30, 0.09
$NE\Delta T$, K	0.4	0.5	0.4	0.5, 0.4	1.7, 0.5

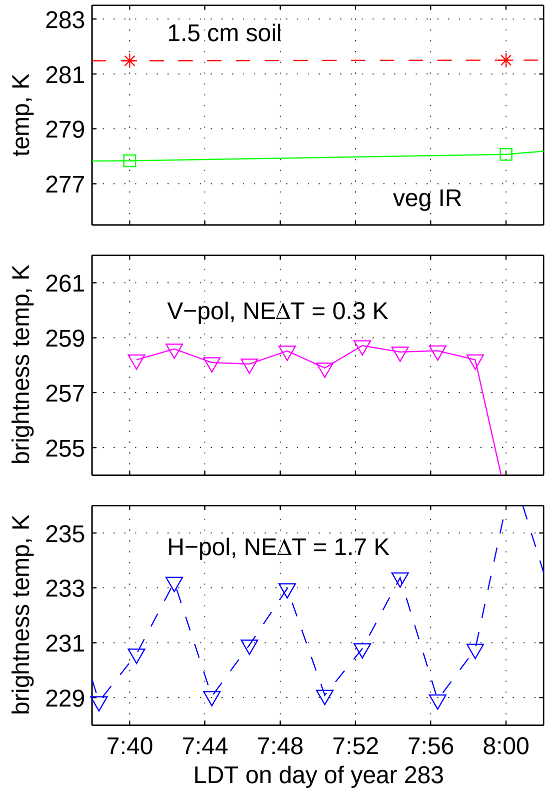

Figure 2.4: An example of radiometer precision during REBEX–8x4. Soil and vegetation temperatures and soil moisture (not shown) were essentially constant during the 20–minute period between 7:40 and 8:00 Local Daylight Time (LDT). Presented NEΔT is for the 10 brightness temperature measurements made during this period.

2.1.3 DSDR Calibration

Typically, microwave radiometers are calibrated by filling the beam of the antenna with objects of known brightness temperature. If the relationship between the radiometer output (a voltage in the case of a traditional radiometer, the r_Q value for a DSDR) and brightness is linear, only two calibration points are needed. Such is the case for both DSDRs used in REBEX–8 and –8x. To make an accurate calibration, the actual brightness of the calibration targets must be measured or found in some other way. It is also desirable to have contrasting brightnesses, very "cold" and very "hot" brightness temperatures.

The sky is a perfect calibration load at 1.4 GHz because it is very cold (about 8 K), beamfilling, and very stable. At the top of the atmosphere, the brightness temperature of the sky has two components: T_{cos}, the cosmic background (2.7 K); and T_{gal}, the direction–

Figure 2.5: At left: absorber calibration. At right: microwave absorber.

dependent brightness from our own galaxy. T_{gal} was calculated using radioastronomy sky maps at 1.4 GHz and taking into account the position of Earth relative to the galactic center. At the earth's surface, a up–looking radiometer will also measure downwelling atmospheric emission, T_{atm}, as well as the extra–terrestrial radiation attenuated by the atmosphere:

$$T_{sky} = T_{atm} + \left(T_{cos} + T_{gal}\right) \times L \tag{2.11}$$

where L is the atmospheric attenuation. Both T_{atm} and L were calculated with radiosonde measurements of temperature and humidity made twice daily at the National Weather Service office in White Lake, Michigan, about 90 km north and east of the site. At 1.4 GHz, the atmospheric attenuation and emission are small (in the absence of hydrometeors) and does not vary much from day to day.

Usually a microwave absorber is used as the "hot" source. If the absorber is nearly a blackbody, its brightness temperature can be approximated by its physical temperature. Figure 2.5 illustrates the absorber calibration procedure and the piece of absorber used. Absorber calibration was not successful. Two possible reasons were determined. First, the absorber used may not have been appropriate at 1.4 GHz. The pyramids of the absorber may have been too small (much less than a wavelength), its emissivity less than unity, and hence the brightness temperature may have been considerably different from its physical temperature. The absorber also may have had some degree of transparency at 1.4 GHz. Although the absorber was backed with aluminum foil, the backing was not uniform. Second, the absorber may not have been beamfilling. In an attempt to fill the beam, the absorber was held very close to the antenna aperture, well within the near–field of the antenna where the antenna pattern is not known. Because it was manually positioned, the location of the absorber, both in terms of its coverage of the aperture and its distance from the antenna rim, changed during each calibration attempt. In contrast to when the antennae were pointed at the sky, consecutive r_Q measurements of the absorber varied considerably.

In its place, the internal reference loads were used to calibrate the DSDRs. Although reference load physical temperature was well known, small electrical losses associated with the antenna and the coaxial cable connecting the antenna to the radiometer result in some error so that if the brightness of both the reference load and the scene viewed by the antenna were actually the same, they would be recorded as two different brightnesses. Given these circumstances, the accuracy of both DSDRs were estimated to be within ± 2 K.

The internal reference load was also used to adjust the calibration for changes in system gain observed during the experiments. Two types of gain change were observed: a slow change likely due to diurnal temperature fluctuations of the radiometer components; and sharp changes resulting from changes in radiometer orientation. Although the temperature of the electronics close to the amplifier was stable, the other parts of the radiometer experienced changes in temperature. As coaxial cables and connectors warm and cool, their electrical properties change slightly. Most of the evidence collected point to an A/D converter temperature dependence. Sharp changes in gain were observed when the incidence angle of the radiometer was adjusted. Possible explanations include redistribution of heat within the radiometer and mechanical stress on the radiometer electronics. As is demonstrated in later chapters by the quality of the resulting brightness temperature observations, the gain–change compensation procedure described below worked well.

Figure 2.6 illustrates the compensation procedure. Brightness temperature measure-

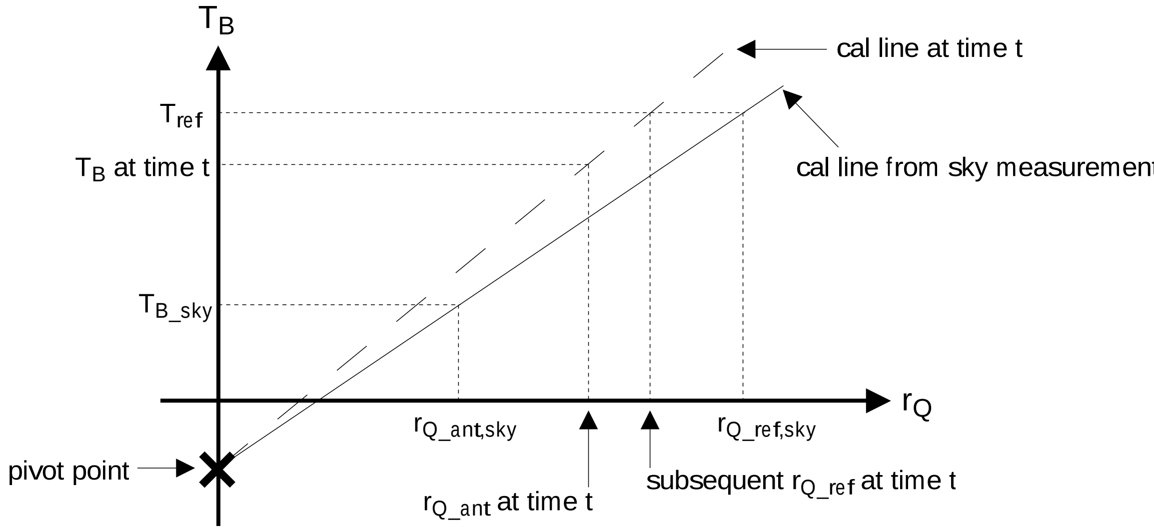

Figure 2.6: DSDR calibration procedure.

ments of both the antenna and internal reference load were made during every measurement cycle. The initial calibration line was established during the sky measurement. Two pairs of r_Q and brightness temperature, from the sky ($r_{Q\_ant,sky}$ and T_{B_sky}) and from the reference load ($r_{Q\_ref,sky}$ and T_{ref}), specified the slope and y–intercept of the line. At a later time t, r_{Q_ref} would change despite the fact that T_{ref} had not, signaling a change in system gain. The new r_{Q_ref} and T_{ref} (which was assumed to be constant) were used to find the slope of a new calibration line, the dashed line in Figure 2.6. The y–intercept (marked "pivot point") was not allowed to change. It represents the amount of "negative brightness" that would have to be captured by the antenna to completely cancel the self emission, or noise of the radiometer. This noise, denoted T_{rec} in the microwave remote sensing literature, actually does change with temperature but the effect on the output is small relative to temperature–induced gain changes. Here the change in T_{rec} was assumed to be zero. At $r_Q = 0$, gain change is of no consequence and this hypothetical negative brightness is constant. The x–intercept (the r_Q value when $T_B = 0$ K) represents the self–emission of the radiometer since this is the power measured when no power is intercepted by the antenna, i.e. the scene brightness temperature is 0 K. This self emission *does* change with system gain, and hence the x–intercept changes over time.

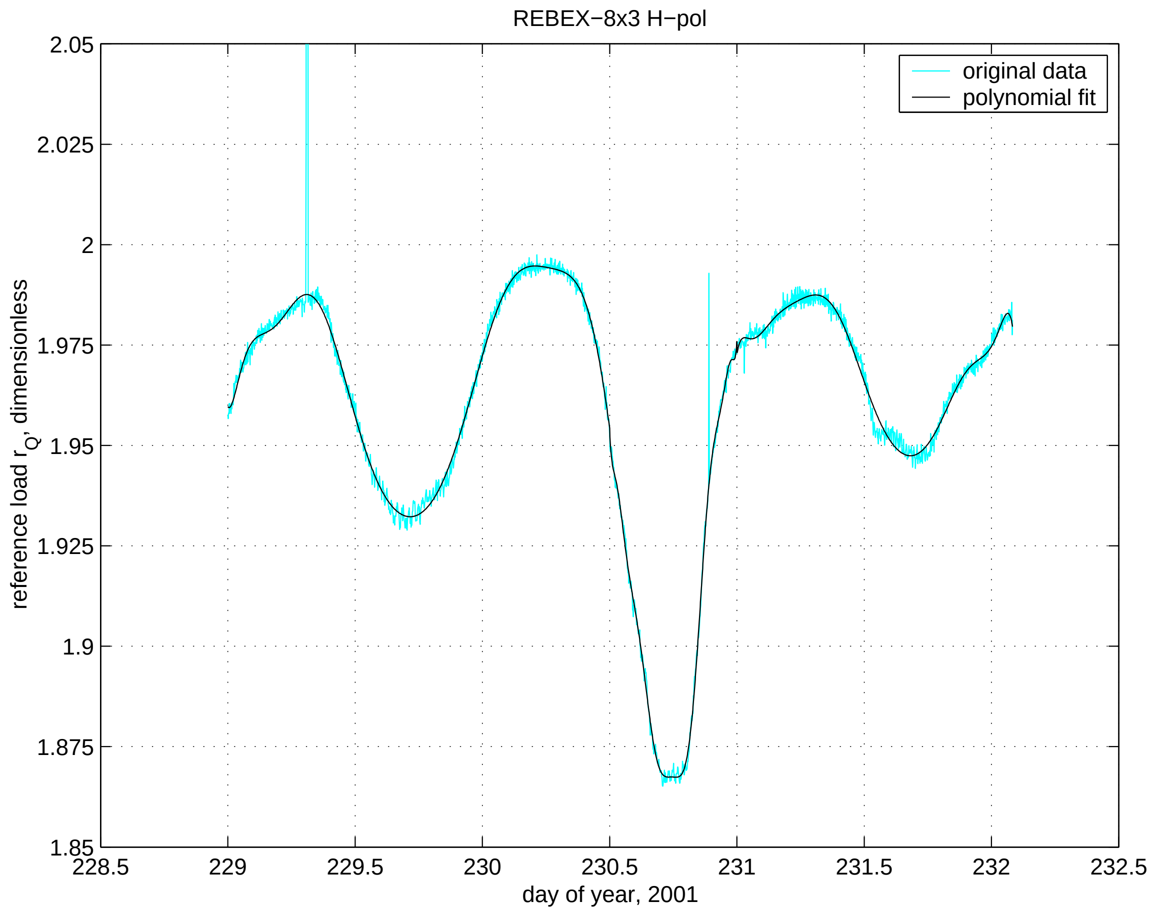

Figure 2.7: Recorded reference load r_Q and fitted polynomial for the H–pol DSDR during REBEX–8x3.

As stated above, the temperature of the reference load was assumed to be constant. From Figure 2.3, it can be seen that this is a good assumption over long periods of time, but there is considerable variation from measurement to measurement. This variation is close to the σ_{amp} described above, but not exactly because the amplifiers and reference load were not subjected to exactly the same thermal environment as evidenced by the slight, but consistent, temperature difference. If not taken into account, this thermal noise would degrade $NE\Delta T$. To compensate for these short temperature fluctuations of the reference load, a polynomial fit of r_{Q_ref}, instead of the actual r_{Q_ref} measurements, was used to adjust the slope of the calibration line. Figure 2.7 shows actual r_{Q_ref} measurements and the polynomial fit for the H–pol DSDR during REBEX–8x3. Note the rapid changes in short–term

Figure 2.8: Laser profiler.

temperature on top of a smooth, slow variation, obviously the result of a diurnal temperature change. This was typical of the H–pol DSDR. The V–pol DSDR, on the other hand, was more susceptible to sharp changes in gain associated with rotation of the radiometer. The same polynomial fitting procedure was used to smooth the V–pol r_{Q_ref} variations. This compensation procedure is valid because the reference load was not subject to direct thermal control as were the amplifiers. The time constant of the reference load temperature change is much greater than the integration period.

2.2 Laser Profiler

A laser profiler was used to measure soil surface height variations during REBEX–7. It is pictured in Figure 2.8. The profiler had a horizontal resolution of 1 mm and a vertical precision on the order of 10^{-2} mm. Four one–meter transects perpendicular to row direction of undisturbed soil in the REBEX–7 field were measured on August 25, 2000, (day of year 238) under conditions very similar to what was present during REBEX–8x3. These four transects were oriented end–to–end and covered seven rows.

Two examples of the surface height profile are shown in Figure 2.9. The depression

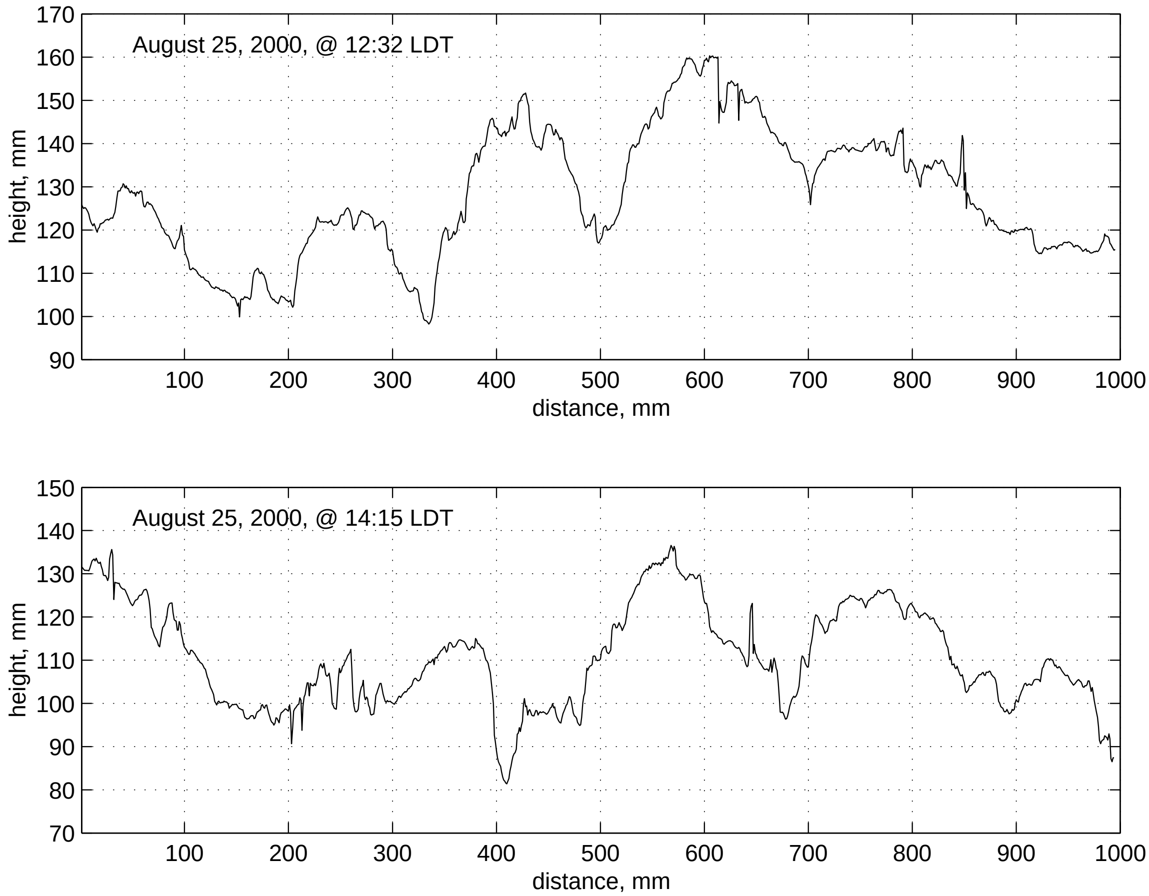

Figure 2.9: Two examples of recorded soil surface profile.

at 500 mm in the top profile is the row, the point at which a stem of a corn plant would be. Recall that the average row spacing was 0.77 m. Note the generally "high" area from approximately 400 to 850 mm. The bump between 200 and 300 mm may have been a clod or vegetation debris. In the bottom figure, the row depression is just before 700 mm, and the 0 to 700 mm region represents almost an entire row space. The depression at 400 mm was likely a crack in the soil.

There are two quantities often used to characterize a rough surface. The first is the standard deviation of the surface height (or rms roughness), σ_s. The second is the correlation length, l_c, which describes the similarity in height of two points separated by a certain distance, or *lag*. A surface with a high level of large–scale roughness would have a short l_c, meaning that the surface height changes quickly as you move away from a given point.

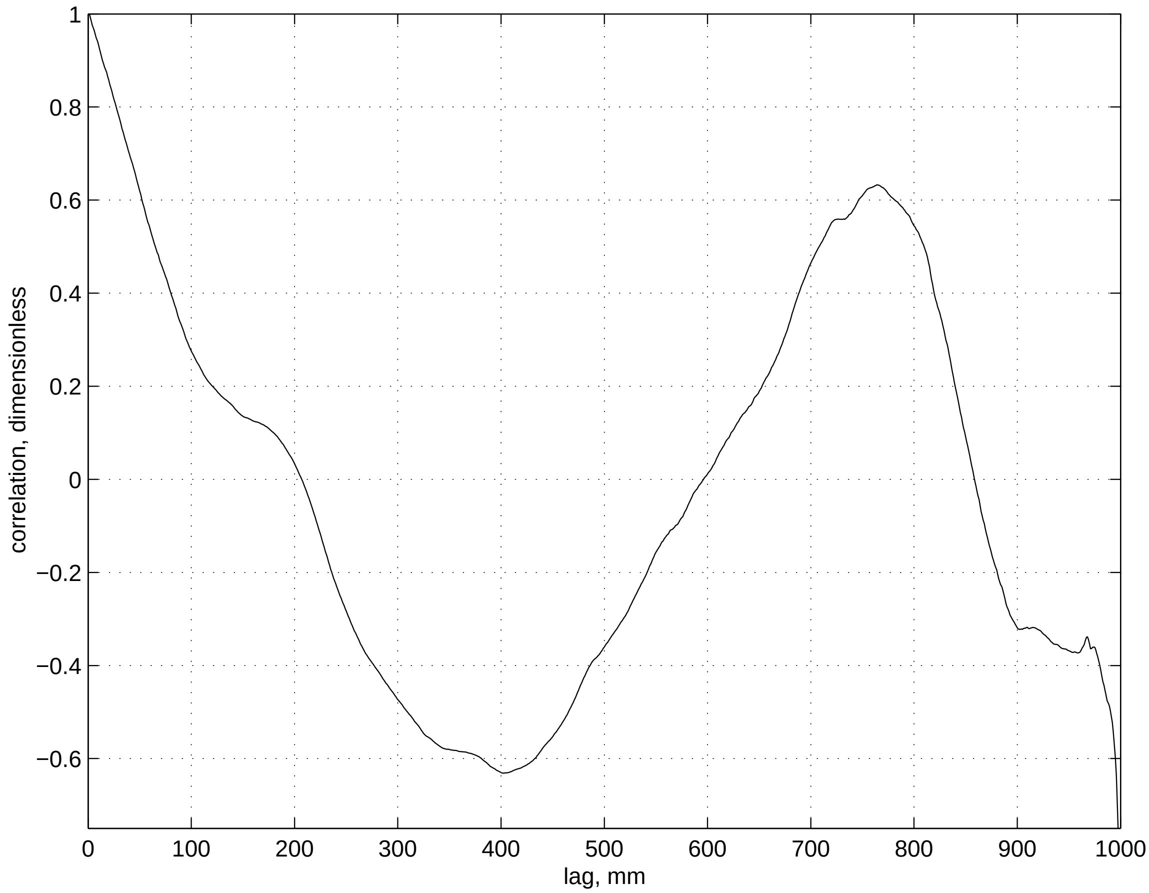

Figure 2.10: Computed correlation function.

One example would be freshly tilled soil, where the height variation changes quickly due to large, broken clods. An example of a surface with a long correlation length is a large body of water. The ratio σ/l_c is a measure of the average slope of a surface.

Calculation of σ_s, is straight–forward. The correlation function, ρ, is computed:

$$\rho(n) = \frac{\frac{1}{(N-n)-1}\sum_{j=1}^{N-n} z(j)\, z(j+n)}{\frac{1}{N-1}\sum_{j=1}^{N} z(j)^2} \tag{2.12}$$

where n is the lag, N is the total number of points measured, and $z(j)$ is the height of the j^{th} point along the transect. The correlation length is defined as $\rho(l_c) = 1/e \approx 0.3679$. The numerator of (2.12) is the (unbiased) estimate of the height correlation between two points along the transect separated by a lag of n. This correlation is normalized by the height correlation of zero lag (which is the surface height variance $\sigma_s{}^2$).

Figure 2.10 is a plot of the average correlation function $\rho(n)$. For the soil surface in

REBEX–7, the average surface height standard deviation was $\sigma_s = 14$ mm and the average correlation length was $l_c = 85$ mm. The periodic nature of the row structure is evident: note that ρ peaks again at precisely the average row width of 0.77 m. In the case of a periodic surface, the total roughness can be thought of as a random roughness superimposed on a periodic function. Because the random roughness is uncorrelated to the periodic variation, the difference between the two peaks in Figure 2.10 represents this random roughness. The peak of the correlation function at 0.77 m corresponds to a rms height of $\sqrt{0.63 \times 14^2} \approx$ 11 mm. This is the rms height of the periodic variation. The rms value of the random roughness is $\sqrt{14^2 - 11^2} \approx 9$ mm

According to *Oh and Kay* [1998], surface segments totaling $40\sigma_s$ and $200l_c$ must be used to accurately characterize these surface parameters. While this condition was satisfied for σ_s, l_c must be considered a rough estimate. On the other hand, these values match well those measured by *Wigneron et al.* [2001] for tilled agricultural fields, particularly their field 18 with $\sigma_s = 19$ mm and $l_c = 66$ mm.

2.3 Soil Moisture

The accurate and precise measurements of near–surface soil moisture made on the plot–scale were one of the highlights of REBEX–8 and –8x. Not only was this the first time that members of the Microwave Geophysics Group had successfully made continuous soil moisture measurements, this data set is now one of a very few known data sets of soil moisture through the emitting depth at 1.4 GHz under a vegetation canopy. A soil–specific calibration of a hand–held impedance probe was made with gravimetric samples and bulk density measurements. Approximately one thousand impedance probe measurements were made over the course of the experiments to calibrate continuous measurements of volumetric soil moisture made made by buried time domain reflectometry (TDR) instruments. The TDR instruments were buried at appropriate depths to match the sample depth of the impedance probe. When grouped together, the TDR measured 0–3 and 3–6 cm volumetric

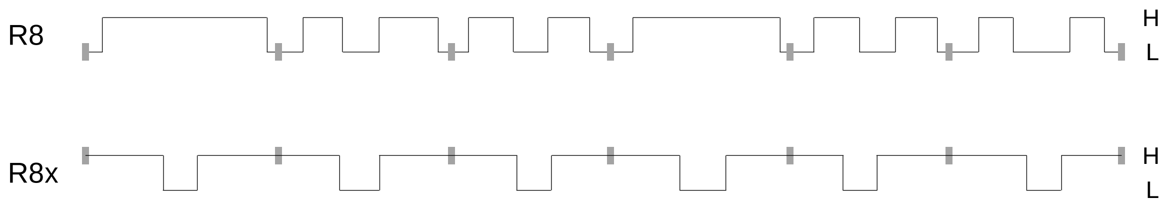

Figure 2.11: Soil topography during REBEX–8 and REBEX–8x reduced to a binary representation.

soil moisture. In the following sections, the methods and materials used to make these measurements are presented along with error analyses.

2.3.1 Measurement Technique

Planting and cultivation produce distinct localized soil topography in agricultural fields [*Kaspar et al.*, 1995]. This topography was reduced to a binary representation of high (H) and low (L) areas as a practical way to retain this unique row structure. Figure 2.11 illustrates the H and L representation. Although only 2 to 4 cm lower than H areas, L areas were distinct from the rest of the soil surface because of their significantly higher water content (and resulting darker color), bulk density, and smoother surface. They tended to be located in the middle of the row space and in the row during REBEX–8, although absent in every third row space. When the soil was cultivated, the top 5 to 7 cm of the soil in the middle of the row space was effectively "pushed" towards the rows, creating a L area in each row space. No distinction was made between trafficked (wheels of tractor or other machinery) and un–trafficked row spaces. The fractions of H and L areas were determined by sampling several rows with a metric tape measure. During REBEX–8, 36% of the soil surface was classified as L. After cultivation, the this fraction changed to 21%.

To find the overall near–surface soil moisture content, TDR instruments were placed at 1.5 and 4.5 cm below the soil surface in both H and L areas. The sample volume of a TDR instrument has the shape of slightly flattened cylinder of length equivalent to the length of the transmission lines. The sensing volume extends slightly farther in the plane containing the two wires of the transmission line than in the perpendicular direction. According to cal-

Figure 2.12: TDR during REBEX–8: at left, in a high area at 1.5 cm; at right, in a low area at 4.5 cm.

Figure 2.13: Impedance probe. Each of the four tines are 6 cm long.

culations performed by *Knight* [1992], approximately 80% of the sensing volume is within a 2 cm radius, and slightly more than 90% within a 3 cm radius for the particular TDR instruments used in REBEX–8 and –8x. When oriented so that the plane containing the two wires of the transmission line is parallel to the soil surface, *Baker and Lascano* [1989] found that TDR instruments have a vertical resolution of approximately 3 cm. Hence the TDR placed at 1.5 and 4.5 cm measured the 0–3 and 3–6 cm layers, respectively.

Figure 2.12 shows TDR during REBEX–8 placed in an H area at 1.5 cm and in an L area at 4.5 cm. To install a TDR, a sharp vertical face was cut into the soil and the TDR was slowly pushed into the face while keeping it level. During TDR installation at the beginning of REBEX–8 and –8x, the soil was wet and sticky allowing such shallow insertion depths and reducing the probably of large air gaps that degrade TDR sensitivity [*Knight et al.*, 1997]. After insertion, soil was replaced under, over, and around the sensor head.

Twelve total TDR instruments were used, evenly divided among H and L areas and

Figure 2.14: Orientation of impedance probe and TDR. Top: side view. Bottom: plan view. Drawn to scale.

depths of 1.5 and 4.5 cm. Three individual TDR were averaged together to produce measurements at 1.5 and 4.5 cm in H and L areas. The H and L areas were then weighted according to their spatial fractions to obtain an overall 0–3 and 3–6 cm measurement. The TDR were calibrated *in-situ* with a hand–held impedance probe at several points throughout the experiments. The impedance probe is pictured in Figure 2.13, and Figure 2.14 illustrates the relative orientation of the impedance probe and TDR instruments. When TDR at 1.5 and 4.5 cm are combined, their vertical sample depth matches the 0–6 cm sampled by the impedance probe. TDR were not placed directly on top of each other. The diagram in Figure 2.14 illustrates only the concept of combining 1.5 and 4.5 cm measurements to obtain a 0–6 cm value.

Impedance probe measurements were made on eight days over the course of the summer (days of year 143, 144, 145, 185, 187, 194, 229, and 270). On each day, 10 measurements were made in H areas and 10 measurements were made in L areas at 7 randomly chosen sites in the experiment area, for a total of 140 measurements (70 H and 70 L) per day. Each set of ten impedance probe measurements were made at random locations within an approximately four meter square area. The sites were located on either side of the path through the field which led from the head of the lane to the micrometeorological station tower (Figure 2.2). Foot traffic in the field was restricted to this path only. Averaging the H and L impedance probe measurements calibrated the TDR instruments, buried in adjacent rows to the north and south of the tower, to the *field–average* near–surface soil moisture. According to the theory of time–stability [*Vachaud et al.*, 1985], the spatial pattern of soil moisture persists and hence soil moisture measured at the tower changes in concert with soil moisture in other parts of the field. Due to the extreme uniformity of the site, the differences in average soil moisture among sites within the field along the path leading to the tower were low, always less than 0.04 $m^3\ m^{-3}$ and typically less than 0.02 $m^3\ m^{-3}$. As a result, soil moisture within the footprints of the radiometers is assumed to be accurately measured with TDR buried a considerable distance away near the tower.

2.3.2 Impedance Probe

At frequencies of less than 1 MHz, a variety of factors such as the bulk density, water content, water salinity and chemistry, oxidation-reduction reactions, cation exchange processes, corrosion processes, chemical concentration gradients, clay–organic reactions, and other phenomena can affect the electrical properties of soil [*Olhoeft*, 1989]. At higher frequencies in the MHz and GHz range, water content primarily determines soil electromagnetic properties. In non ferro–magnetic soils, it is the soil's relative permittivity, ε_r, which changes with water content. For frequencies below about 20 GHz, the real part of the relative permittivity of liquid water is about 80 while for the types of minerals typically found in soil it is around 3 to 5. Moist soil is a combination of water and minerals (as well as organic matter) and can have a relative permittivity between 3 and 30 in the microwave region [*Hallikainen et al.*, 1985]. Strong linear relationships between the refractive index, $n = \sqrt{\varepsilon_r}$, and water content for many types of soils have been observed [*Topp et al.*, 1980; *Whalley*, 1993; *White et al.*, 1994; *Curtis*, 2001].

A ThetaProbe ML2x (Delta–T Devices, Cambridge, UK) impedance probe was used to measure soil water content and subsequently calibrate buried TDR instruments. It consists of four 6 cm sharpened stainless steel rods that protrude from a 40 mm diameter and 112 cm long PVC cylinder (Figure 2.13). Three shield rods are spaced equally on a 26.5 mm circle surround the center signal rod. The diameter of each rod is 3 mm. The approximate volume of soil sampled by the ThetaProbe, a 4 cm diameter, 6 cm long cylinder surrounding the signal rod, is approximately 75 cm^3. This impedance probe generates a 100 MHz electrical signal on an internal transmission line. When inserted into the ground, the four rods form another transmission line whose characteristic impedance depends on the relative permittivity of the soil. Reflections at the interface between the internal transmission line and the rod array produce a standing wave. The voltage output is proportional to the voltage standing–wave ratio, VSWR $= (1+ \mid \Gamma \mid) / (1- \mid \Gamma \mid)$. Here Γ is the reflection coefficient:

$$\Gamma = \frac{Z_{array} - Z_o}{Z_{array} + Z_o} \tag{2.13}$$

where Z_o is the characteristic impedance of the internal transmission line and Z_{array} is the impedance of the load formed by the rod array. Z_{array} is a function of n_{soil}, the soil refractive index, and the geometry of the rod array. The ThetaProbe ML2x has been carefully designed so that there is a linear relationship between the output of the impedance probe, V, and n_{soil} [*Delta–T Devices Ltd.*, 1999]:

$$V = (n_{soil} - 1.1)/4.44. \tag{2.14}$$

The impedance probe was calibrated with gravimetric sampling and bulk density measurements. The equipment used to do this is pictured in Figure 2.15. When calibrations were made, a metal scoop was used to remove a 5 cm by 5 cm by 6 cm = 150 cm^3 rectangular prism surrounding the holes left by the tines of the impedance probe. The soil sample was then placed into a paper cup and immediately weighed on a portable electronic balance. All soil samples were dried in a 105 °C oven for 48 hours and weighed again.

The mass of the paper cups changed significantly during drying. The cups had a waxy coating that slowly evaporated. Cup mass changed rapidly in the first 2 days, and then slowly thereafter. Figure 2.16 presents histograms of cup mass before and after drying. Mean fresh cup mass was 8.7 g with a standard deviation of 0.1 g, which was close to the

Figure 2.15: Equipment used to measure gravimetric water content (at left) and bulk density (at right).

precision of the balance. After drying, mean cup mass was 7.4 g with a slightly larger standard deviation of 0.2 g.

Bulk density was measured using the USDA–ARS technique. The apparatus is shown in Figure 2.15). A plexiglass disc with a cut–out center was fastened to the soil surface with long bolts. Foam underneath the disc conformed to the soil surface. Plastic bags, water, a large syringe, a graduated cylinder, and a hook gauge were used to find the volume within the cavity above the soil surface made by the foam and disc before and after soil was excavated. Approximately the first 6 cm of the soil was excavated. The excavated soil was placed in a paper bag and later weighed on a balance after drying for 48 hours at 105 °C. The soil bulk density, ρ_b, was found by dividing the mass of dry soil, m_{dry}, by the difference between the volumes before and after excavation:

$$\rho_b = m_{dry} / \left(v_{after} - v_{before} \right) . \tag{2.15}$$

The mean and standard deviation of the paper bag masses were found before and after drying in a manner similar to that used for the paper cups. A total of ten bulk density measurements were made, five in H areas and five in L areas. The mean H bulk density

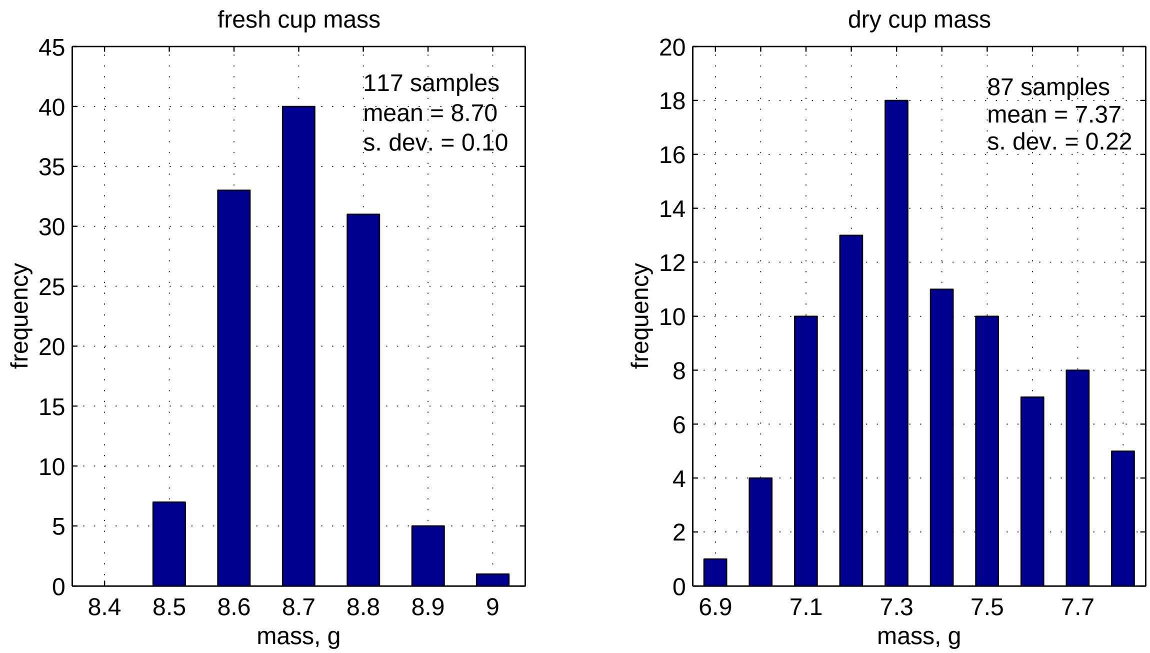

Figure 2.16: Histograms of cup mass before (at left) and after (at right) drying in a 105 °C oven.

was 1.09 g cm^{-3}, while the mean L bulk density was 1.21 g cm^{-3}.

The volumetric water content, θ_v, of a gravimetric sample is:

$$\theta_v = \theta_g \frac{\rho_b}{\rho_{water}} \tag{2.16}$$

where θ_g is the gravimetric water content and ρ_{water} is the density of water. Assuming all variables are normally distributed, the standard deviation of a single volumetric soil moisture measurement made with the scoop, σ_{θ_v}, was found using the method of fractional standard deviations [*Beers*, 1962] to be:

$$\sigma_{\theta_v} = \theta_g \frac{\rho_b}{\rho_{water}} \sqrt{\frac{\sigma^2_{\theta_g}}{\theta^2_g} + \frac{\sigma^2_{\rho_b}}{\rho^2_b}}. \tag{2.17}$$

where σ_{θ_g} is the standard deviation of a gravimetric measurement and σ_{ρ_b} is the standard deviation of the bulk density measurements. The error associated with soil sampling was very small: σ_{θ_v} ranged from 0.003 to 0.008 m^3 m^{-3}.

A total of 37 gravimetric measurements were used to calibrate the impedance probe. Recall that linear relationships between water content and refractive indices for many types

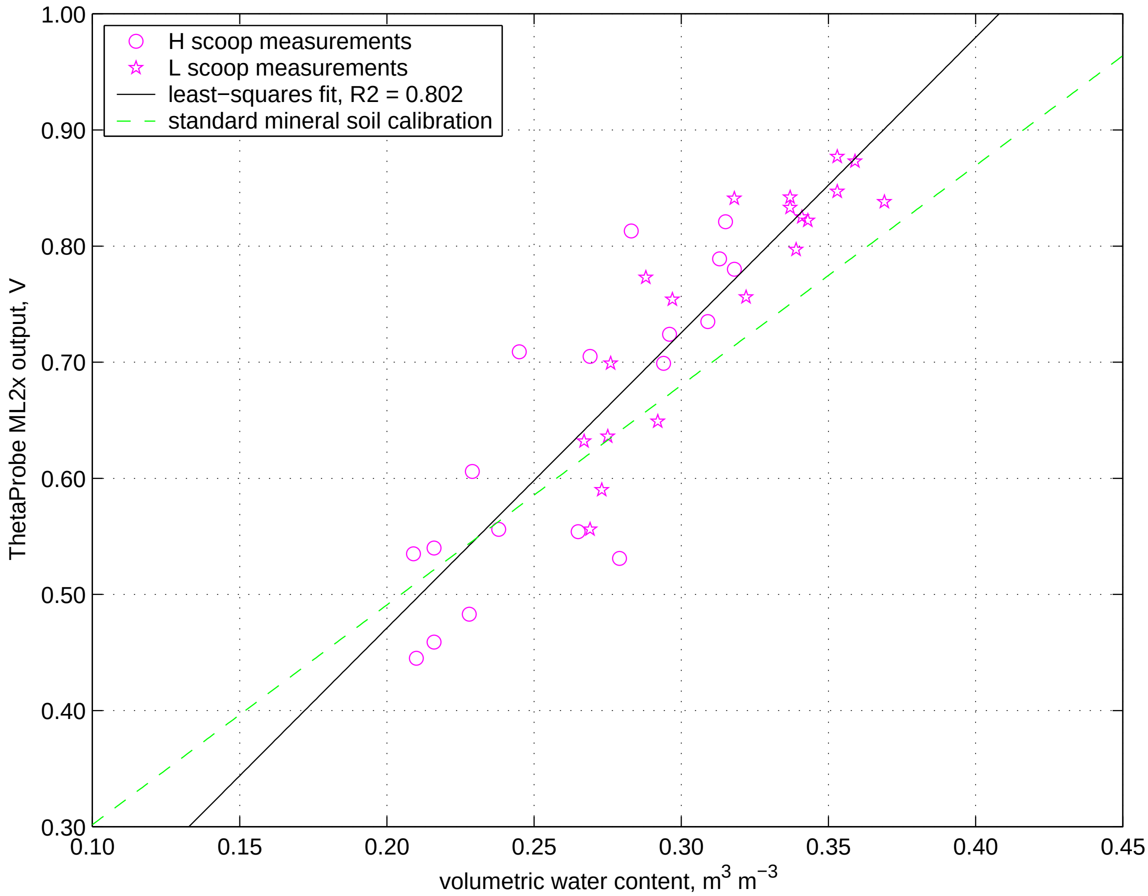

Figure 2.17: Impedance probe calibration.

of soil have been observed by other investigators. Hence

$$n_{soil} = a_0 + a_1 \theta_v. \tag{2.18}$$

As expected from (2.14), the relationship between volumetric water content and impedance probe output voltage is also linear, as shown in Figure 2.17. For the silty clay loam soil in REBEX–8 and –8x, $a_0 = 0.9$ and $a_1 = 11$. These values are significantly different from those established for mineral soil ($a_0 = 1.6$ and $a_1 = 8.4$) and for organic soil ($a_0 = 1.3$ and $a_1 = 7.7$) [*Delta–T Devices Ltd.*, 1999]. The standard calibration line for mineral soil is also included in Figure 2.17. A higher value of a_1 is consistent with the findings of *White et al.* [1994] who found the slope of the line relating water content to the refractive index to increase with clay content (the clay fraction of the REBEX–8 soil was 28.9%).

The standard deviation of the differences between the linear relationship and actual volumetric measurements shown in Figure 2.17 is approximately 0.02 $m^3\ m^{-3}$. This error can be explained by the precision of the ThetaProbe ML2x (about 0.005 $m^3\ m^{-3}$ [*Delta–T Devices Ltd.*, 1999]), the standard deviation of the soil samples (about 0.005 $m^3\ m^{-3}$), and an error of $\approx$ 0.01 or 0.02 $m^3\ m^{-3}$ associated with the difference in the volume of soil sampled by the impedance probe (75 cm^3) and the volume of the gravimetric samples (150 cm^3). This sample size variability is consistent with observed impedance probe measurements. The standard deviation of measurements within one site (four meter square area) varied from 0.01 to 0.06 $m^3\ m^{-3}$ for both H and L areas. Any temperature dependence due to the variation of water's relative permittivity with temperature was ignored. This simplification may also have contributed to the error.

2.3.3 Time Domain Reflectometry Instruments

Water Content Reflectometers (WCRs) manufactured by Campbell Scientific (model CS615 8221-07) were used to make continuous measurements of soil volumetric water content. Many researchers have been confused by inaccurate descriptions of the WCR: they are *not* "frequency domain reflectometers" nor are they capacitance soil water sensors [*Seyfried and Murdock*, 2001]. They are in fact a type of automated TDR instrument. Each WCR consists of a two–wire transmission line and a circuit board encapsulated within its epoxy head. The transmission line is 30 cm long, each wire has a radius of 1.6 mm, and the wires are separated by 3.2 cm. The circuit is essentially a bistable multivibrator that transitions from one voltage level to another [personal communication, Jim Bilskie, Campbell Scientific, 2002]. This transition, which occurs within a few nanoseconds, propagates down the length of the transmission line, is reflected by the open circuit at the end, and travels back to the sensor head. The reflected transition triggers the multivibrator to transition again, and the process is repeated. The output of a WCR is a frequency–scaled square wave whose period corresponds to the length of time between the multivibrator's transitions, which corresponds to the time it takes the pulse to make a round–trip on the

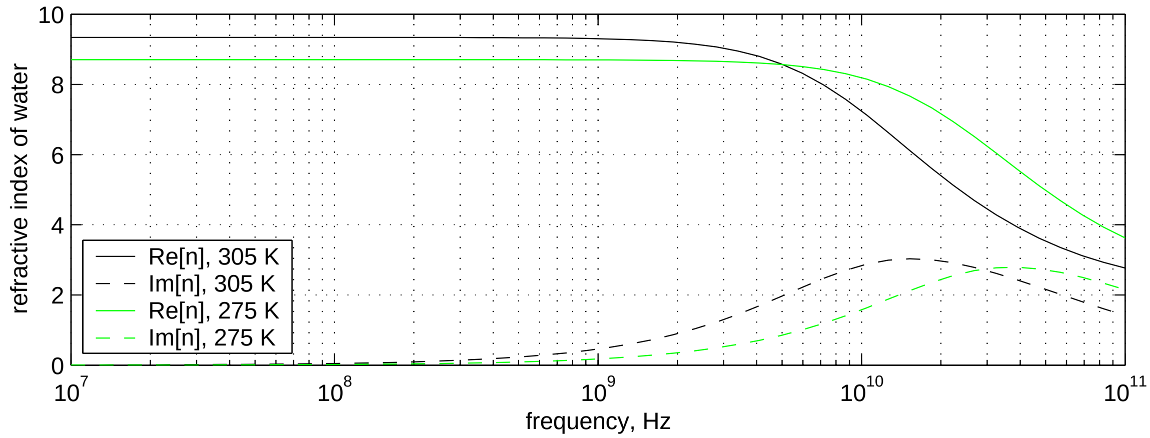

Figure 2.18: The index of refraction of pure water ($\sigma_e = 0$) at 305 K and 275 K.

transmission line. As soil relative permittivity increases with water content, so does the round–trip travel time.

A soil's relative permittivity is a function of its electric susceptibility, χ_e and electrical conductivity, σ_e [*Bohren and Huffman*, 1998]:

$$\varepsilon_r = (1+\chi_e) - j\,\frac{\sigma_e}{\omega\varepsilon_o} = \varepsilon_r' - j\,\varepsilon_r'' \tag{2.19}$$

where $\omega = 2\pi f$ is the angular velocity, f is the frequency, and ε_o is the free–space permittivity. The general form of a homogeneous plane wave for the electric field, $\vec{E}$, propagating in the z direction is:

$$\vec{E} = \vec{E_o}\,\exp\left[-\left(\frac{2\pi}{\lambda}n''z\right) - \ j\left(\frac{2\pi}{\lambda}n'z - \omega t\right)\right] \tag{2.20}$$

where $\vec{E_o}$ is a constant vector compatible with Maxwell's equations, λ is the free–space wavelength, and $n = n' - j\,n''$. The real and imaginary parts of the index of refraction are related to the real and imaginary parts of ε_r as follows:

$$n' = \sqrt{\left(\sqrt{\varepsilon_r'^{\,2} + \varepsilon_r''^{2}} + \varepsilon_r'\right)/\ 2}, \tag{2.21}$$

$$n'' = \sqrt{\left(\sqrt{\varepsilon_r'^{\,2} + \varepsilon_r''^{2}} - \varepsilon_r'\right)/\ 2}. \tag{2.22}$$

In general, χ_e is complex. Due to its highly polar molecular structure, pure water exhibits a dielectric relaxation between 5 and 30 GHz [*Debye*, 1929; *Cole and Cole*, 1952]. Above this relaxation frequency, the water molecules do not rotate and the relative permittivity (and refractive index) decreases. Figure 2.18 illustrates this relaxation at two different temperatures [*Stogryn*, 1971]. Using (2.20) it can be shown that the phase (propagation) velocity of an electromagnetic wave is $u_p = c/n'$ where c is the speed of light in a vacuum. Waves propagating through a medium are also attenuated according to the magnitude of n''. Hence waves traveling on the TDR transmission line, whose Fourier components range from the tens of MHz to the tens of GHz, will exhibit *dispersion* due to the frequency dependence of the real and imaginary parts of the refractive index. The degree of dispersion depends primarily on two factors: the fraction and degree to which soil water is held, or *bound*, to the soil matrix [*De Loor*, 1956; *Hoekstra and Doyle*, 1972]; and the bulk soil electrical conductivity [*Hoekstra and Delaney*, 1974]. Both effects are not well understood. Bulk soil electrical conductivity increases linearly with water content in most soils [*Rhoades et al.*, 1989]. There is still much debate on the nature of bound water [*Grant et al.*, 1957; *Wang*, 1980; *Dobson et al.*, 1985; *Or and Wraith*, 1999; *Hillhorst et al.*, 2001] and its effect on TDR measurements, particularly in clayey soils [*Dasberg and Hopmans*, 1992; *Dirksen and Dasberg*, 1993]. As a result, no universal calibration for TDR exists.

TDR measurements are also affected by temperature. *Pepin et al.* [1995] noted that since pure water relative permittivity decreases with temperature (Figure 2.18), soil moisture can be overestimated at higher soil temperatures. Their simple refractive mixing model did not take into account soil type and they found that measured temperature change was not as great as predicted. For the soils tested, sand had the greatest change with temperature, while loam and peat were much less. *Persson and Berndtsson* [1998] also measured TDR temperature dependence, taking note of the temperature dependence of electrical conductivity. The soils with large surface areas, high clay contents, and high electrical conductivity had *positive* temperature correction factors. The other soils (which were mostly

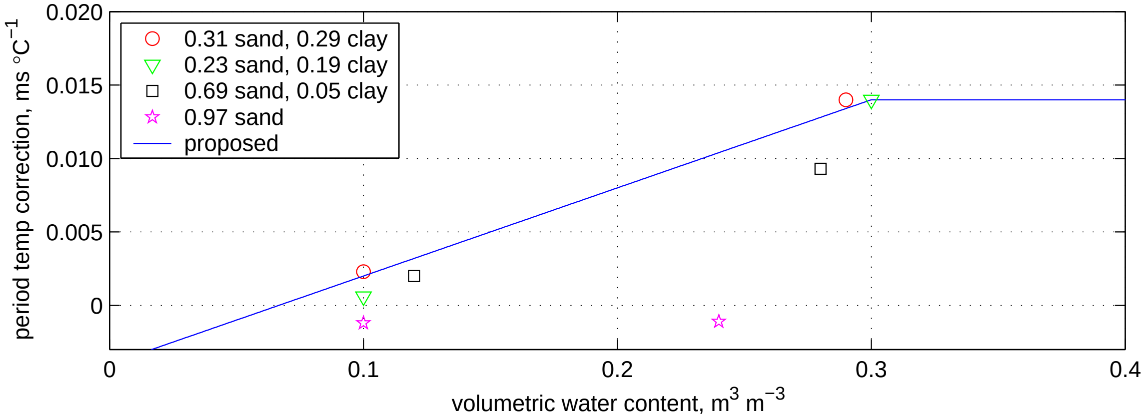

Figure 2.19: Proposed WCR period temperature correction based on *Seyfried and Murdock* [2001].

sands) had *negative* correction factors, as predicted by the temperature dependence of pure water. *Wraith and Or* [1999] measured TDR pulse travel time as a function of temperature for four soils. They found that high surface area and low water content are conditions favorable for an increase in measured travel time with increasing temperature and speculated there is a "release" of bound water with temperature in soils with low water contents and in soils with high surface areas.

Seyfried and Murdock [2001] tested the CS615 model 8221-07 WCR in air, water, sand, and three soils to evaluate its temperature dependence. They found that the WCR is extremely precise. There is also a small but significant unique sensor bias that can be measured and corrected. The WCR electronics by themselves exhibit a small but consistent temperature effect of -0.000533 ms $^{\circ}$C^{-1}. Following their example, the raw WCR pulse periods were corrected for the electronics temperature effect. Inter–sensor variability was ignored since three WCRs were averaged together at each combination H and L and depth. The corrected period, P, was then fit to a second–order polynomial:

$$P = A + C_1\,\theta_v + C_2\,\theta_v^2 \qquad (2.23)$$

where A, C_1, and C_2 were found by the method of least squares using the impedance probe measurements. The parameter A was forced to be 0.760 ms as found by *Seyfried and Mur-*

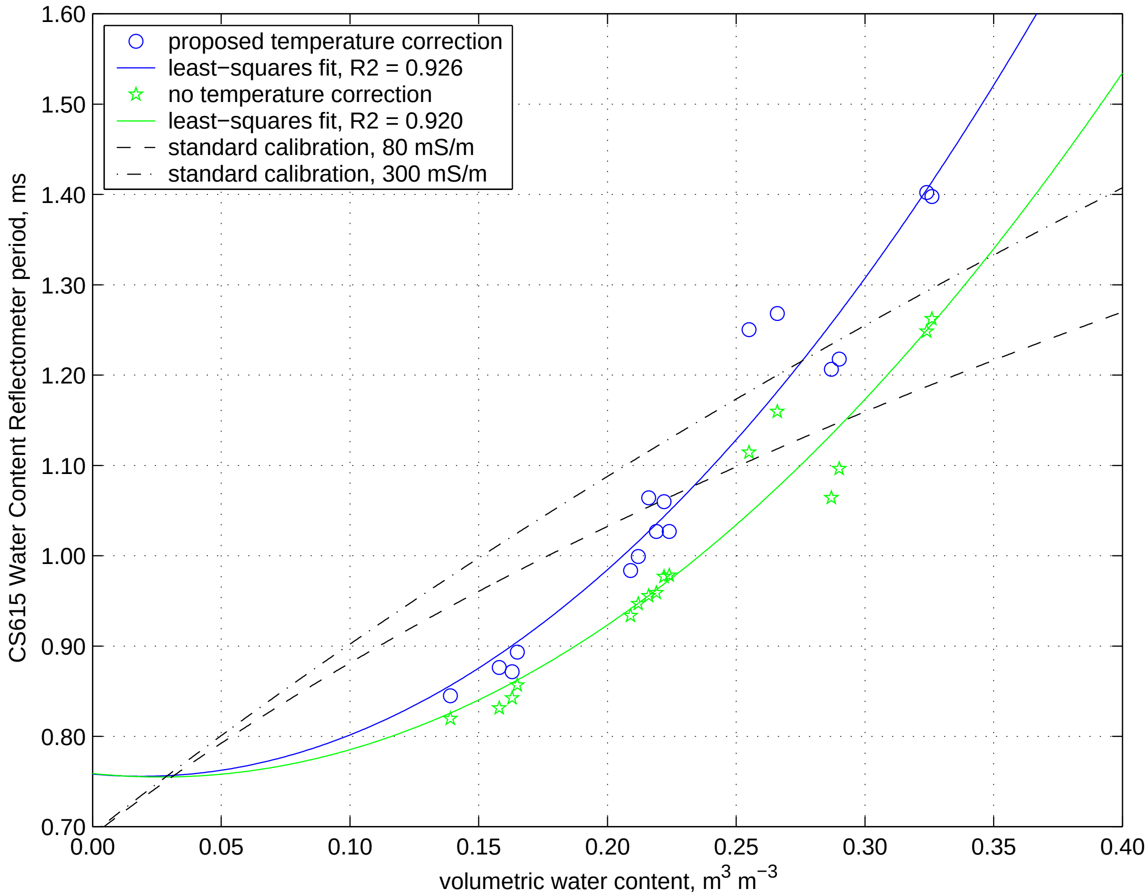

Figure 2.20: TDR calibration.

dock [2001] for oven–dry soil, independent of soil type. The three soils tested in *Seyfried and Murdock* [2001] each had significant positive temperature dependencies. Figure 2.19 shows measured temperature effects and a proposed temperature correction based upon these observations for the soil in REBEX–8 whose clay content was very similar to the first test soil. The temperature dependency for sand is also shown. Note that it is slightly negative.

Two calibration curves for the WCRs are shown in Figure 2.20, one assuming the proposed positive temperature dependence, and the other no temperature dependence. The standard calibration curves provided by the manufacturer for soils with low and high electrical conductivities are also included. The fit for both curves is good, except for the four points between 0.25 and 0.30 m^3 m^{-3}. Table 2.3 lists the temperature gradients in the soil for eight impedance probe measurements, including three of the four poor points. (Recall that each impedance probe measurement is the average of 70 individual measurements.) The fourth, in H areas on day of year 145, was made just after a precipitation event and hence is likely due to a sharp soil moisture gradient in the 0–6 cm soil layer. Table 2.3 also includes day of year 185 when each H and L measurement fit the calibration curve well. For day 143, during REBEX–8 when the vegetation cover was minimal, larger temperature gradients were recorded than on day 185 during REBEX–8x. The temperature gradient was also slightly larger in L areas where the poor calibration point was made. Day of year 270 was the only day on which impedance probe measurements were made in the afternoon when temperature gradients tend to be greatest. Hence it is possible that temperature gradients within the 0–6 cm layer caused the poor calibration points on days 143 and 270. It is not known what caused the poor point on day 144.

Incident solar radiation, precipitation, and soil temperature at 1.5 cm, along with the 0–3 cm soil moisture in H areas during REBEX–8 using both the proposed temperature correction from Figure 2.19 and no temperature correction is plotted in Figure 2.21. It appears that despite the high clay content of the soil, no temperature correction is warranted. The curve with the proposed temperature dependence shows a large diurnal variation, with unrealistic increases in soil moisture, particularly after each precipitation event. The use of no temperature correction can also be justified by examining the taxonomic class of the

Table 2.3: Soil temperature gradients observed during impedance probe measurements.

day of year	time	H / L	θ_v, m^3 m^{-3}	soil IR – 1.5 cm, K	1.5 – 4.5 cm, K	poor cal point?
143	10:00	H	0.22	1.4	3.4	no
143	10:00	L	0.27	1.6	3.3	yes
144	8:40	H	0.22	-0.5	-0.2	no
144	8:40	L	0.26	-0.8	-0.2	yes
185	10:00	H	0.16	0.2	0.4	no
185	10:00	L	0.22	0.3	0.2	no
270	16:00	H	0.29	-0.3	1.9	yes
270	16:00	L	0.32	0.1	1.5	no

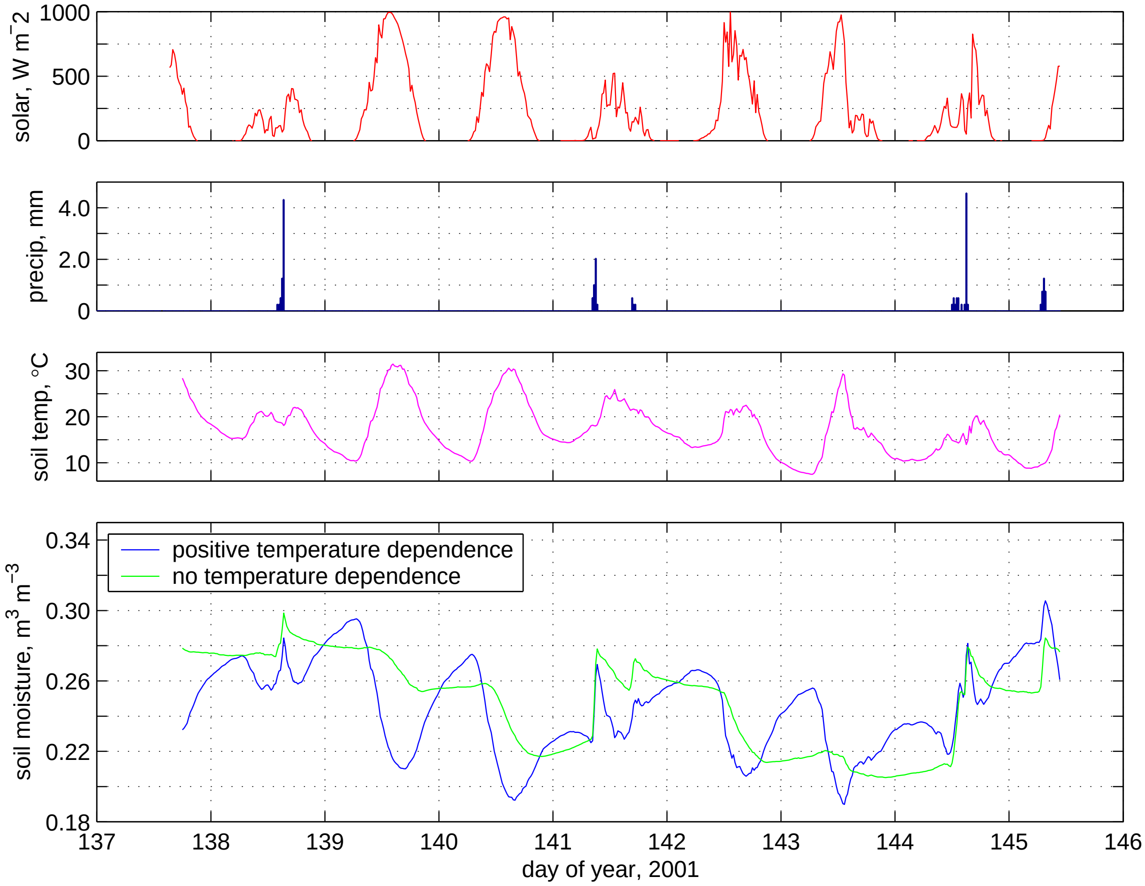

Figure 2.21: Solar radiation, precipitation, soil temperature at 1.5 cm, and 0–3 cm soil moisture in H areas during REBEX–8. Local Daylight Time.

soils in question. The three soils in *Seyfried and Murdock* [2001] occur in arid climates and all have high cation exchange capacities (CECs), or in other words, high electrical conductivity. The Lenawee silty clay loam at the experiment site (28.9% clay content), on the other hand, exists in a more humid climate which tends to wash out salts, and as a result has a low CEC. It is described as a fine, mixed, nonacid, mesic Mollic Epiaquepts [USDA–NRCS Official Soil Series Descriptions, http://soils.usda.gov/classification/main.htm]. The mixed minearology indicates that there is not one dominant type of clay that would favor a high CEC. Although high clay content favors a positive temperature dependence, the type of clay and its charge is equally important [personal communication, Sally Logsdon, USDA–ARS, 2002]. For the soil in REBEX–8, any positive temperature dependence is probably insignificant, or in any case balanced by the negative free water change with temperature.

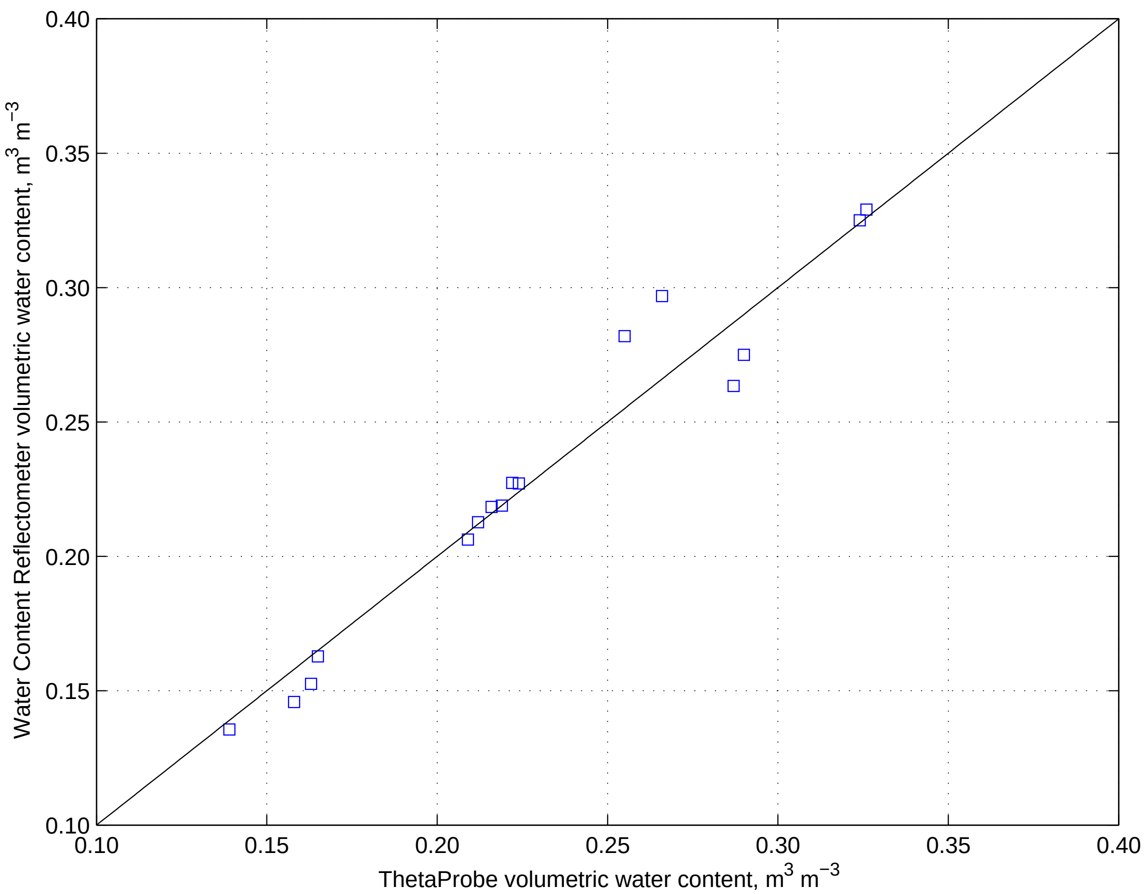

Figure 2.22: Comparison of 0–6 cm volumetric soil water content measured by the ThetaProbe with the average of 0–3 cm and 3–6 cm volumetric soil water content measured by the Water Content Reflectometers.

For no temperature correction due to clay content, the values of the parameters in (2.23) were $A = 0.760$, $C_1 = -0.295$, and $C_2 = 5.584$. The accuracy of WCR measurements are estimated to be < 0.02 m^3 m^{-3} based upon the uniformity of the site. Their precision is $<< 0.01$ m^3 m^{-3}.

A comparison of 0–6 cm volumetric soil water content measured by the ThetaProbe with the average of 0–3 cm and 3–6 cm volumetric soil water content measured by the Water Content Reflectometers with no temperature correction is shown in Figure 2.22. The solid line is the one–to–one line.

2.4 Micrometeorology

A micrometeorological station on a tower (Figure 2.1) was located at the approximate center of the field. The tower was west of the truck by $\approx$ 50 m during REBEX–8 and by $\approx$ 150 m during REBEX–8x (Figure 2.2). Near–surface soil moisture and temperature, soil infrared temperature, vegetation infrared temperature, precipitation, wind speed and direction, relative humidity, air temperature, and incident solar and atmospheric radiation were measured by the instruments listed in Table 2.4 and recorded on a datalogger system. Except for the soil moisture sensors and the thermocouple instruments, the accuracy and precision of each instrument listed comes from the manufacturer. Twenty–minute averages of micrometeorological variables sampled once every ten seconds were recorded.

The tipping bucket rain gauge was located approximately halfway between the truck and the tower. During REBEX–8 when the soil was nearly bare, the gauge was placed within a wind skirt in order to improve its accuracy. In REBEX–8x, the gauge was supported by a large tripod and positioned so that its rim was at the same height of the canopy. An anemometer measured wind speed at 4.0 m during REBEX–8 and 10.0 m during REBEX–8x. Air temperature and relative humidity were measured at 3.2 m during REBEX–8 and 7.8 m during REBEX–8x. These heights are above the roughness sublayer.

The height of the tower's "hazer", a structure that could slide up and down the tower, was controlled with a winch at the tower base. The hazer remained at one fixed position during REBEX–8 and another fixed position above the canopy during all of REBEX–8x, accept during periods of equipment maintenance. The enclosures containing the datalogger, battery, and power control, along with two pairs of metal arms were all mounted on the hazer. The arms pointed E–W during REBEX–8 and N–S during REBEX–8x. The arms supported a pyranometer, a pyrgeometer, an infrared thermometer viewing the canopy, a wind–direction sensor, and a back–up anemometer.

The arms allowed the pyranometer and pyrgeometer to be placed as far away from the tower as possible, reducing any of its influence on the measurements. Both the pyranometer and pyrgeometer were ventilated. Negative values of irradiance recorded by the pyranometer at night due to different cooling rates between the dome and detector [*Dutton et al.*, 2001] were set to zero. Case temperature corrections were made to the pyrgeometer using the case thermistor measurement and not the optional voltage output. Dome temperature was not measured and hence a correction was not made. This correction is small in general [personal communication, Thomas Kirk, The Eppley Laboratory, 2002] and strongly dependent on each pyrgeometer's unique temperature–dependent calibration factor [*Fairall et al.*, 1998; *Reda et al.*, 2002]. This calibration factor was not known and assuming an average value would not have improved the measurement accuracy.

2.4.1 Infrared Thermometers

An infrared (IR) thermometer was positioned approximately 1 m above the canopy and pointed at nadir. An identical IR thermometer underneath the canopy approximately 20 cm above the ground and pointed at nadir measured the soil surface temperature. The IR thermometers consist of two thermocouples: one that measures the detector temperature; and another that measures the sensor body temperature used to correct the detector temperature. The thermocouple measurements were subject to errors in: the reference junction temperature; deviations in the thermocouple output from published standards; the thermocouple voltage measurement; and the datalogger polynomial approximation [*Campbell Scientific, Inc.*, 2001]. A thermistor was used to measure the reference junction of the thermocouples. This thermistor has a ± 0.2 K interchangeability error and a ± 0.1 K polynomial error, resulting in a total accuracy error of ± 0.3 K. The temperature difference between the thermistor (placed on the wiring panel of the datalogger) and the actual temperature of the reference junctions (on the panel of a multiplexor) is small and can be neglected. since the datalogger and multiplexor were approximately 10 cm apart within the same enclosure. Deviations of the actual thermocouple wire performance to published standards are about ± 0.1 K. The accuracy of the datalogger voltage measurements and the polynomial relating thermocouple emf to temperature are each ± 0.01 K. The manufacturer's estimate of error with sensor body temperature correction is ± 0.3 K. All of these errors add up to a total accuracy of ± 0.7 K or less. The manufacturer lists the precision of the instrument as 0.05 K between 285 and 310 K. Precision is also affected by the voltage measurement accuracy and changes in the reference thermistor temperature. All in all, the precision of the IR thermometers is < 0.1 K.

In addition to the errors associated with the instrument itself, there is also an error when the object under view has an emissivity different from unity. Although the IR emissivity of the soil changes with roughness and water content, the space within the lower canopy is essentially a blackbody cavity after the fraction of cover has reached unity. As a result, changes in soil emissivity are of no consequence and the radiometric temperature measured by the IR thermometer is close to the true radiometric temperature, which closely approximates the thermodynamic temperature of the soil surface. On the other hand, despite the fact that the emissivity of a continuous vegetation canopy is between 0.98 and 0.99 [*Campbell and Norman*, 1998], emission from the sky at IR wavelengths is considerably different than emission from the canopy. At microwave wavelengths, sky emission is small enough to be considered negligible. This is not the case at IR wavelengths and reflected sky brightness should be considered.

A vegetation canopy can be modeled as a Lambertian (perfectly rough) surface. To find the expected difference between the radiometric temperature measured by the IR thermometer above the canopy and the true radiometric temperature of the canopy, consider a Lambertian surface of temperature $T_s = 300$ K and emissivity e_s. The irradiance, I, emitted by this surface is:

$$I = e_s\, I_{Bs} \;+\; (1 - e_s)\, I_{sky} \tag{2.24}$$

where I_{Bs} is the blackbody irradiance of the surface and I_{sky} is the downwelling sky irradiance. Since emission from a Lambertian surface is independent of angle,

$$I = \pi\, R \tag{2.25}$$

where R is the radiance of the surface. The radiometric temperature of the surface is a measure of this radiance R. Here the terms irradiance and radiance, instead of power density and brightness, have been used in order to follow the terminology used in the thermal IR remote sensing literature (see *Norman and Becker* [1995]). The units of irradiance (also called radiant flux density) and radiance are W m^{-2} and W m^{-2} sr^{-1}, respectively. Although true for all wavelengths, in the following discussion the irradiances I, I_{Bs}, and I_{sky} and the radiance R are all considered to be within the band of the IR thermometer, 6.5 to 14 μm.

If sky irradiance and irradiance from the surface were the same, then the emissivity of the surface is of no consequence and $I = I_{Bs}$ (as for the IR thermometer below the canopy). In reality, $I_{sky} < I_{Bs}$ so that $I < I_{Bs}$. In other words, the radiometric temperature of this Lambertian surface as measured by the IR thermometer will always be *less* than its true radiometric temperature. Furthermore, sky irradiance is greatest on cloudy days due to the large amount of water vapor in the atmosphere. Hence the difference between I and I_{Bs} (the measured and true radiometric temperature of the surface) will be largest on clear days.

Sky irradiance in the 4 to 50 μm band, $I_{sky,4-50}$, was measured by the pyrgeometer. Sky irradiance in the IR thermometer's wavelength band, I_{sky}, can be calculated as follows. The emissivity of the sky over all wavelengths, $e_{sky,\infty}$, can be approximated

$$e_{sky,\infty} = \frac{I_{sky,4-50}}{\sigma T_{sky}^4} \tag{2.26}$$

where: σ is the Stefan–Boltzmann constant; and T_{sky} is the effective emitting temperature of the sky, both within the band of the IR thermometer and at all wavelengths. This approximation can be made because the irradiance above 50 μm is small and can be neglected. For a clear sky [*Brutsaert*, 1984],

$$e_{sky,\infty} = 1.72 \left(\frac{w_{air}}{T_{air}} \right)^{1/7} \tag{2.27}$$

where w_{air} and T_{air} are the water vapor pressure (in kPa) and the air temperature (in K), respectively, near the surface. For clear days, the effective temperature of the sky can be

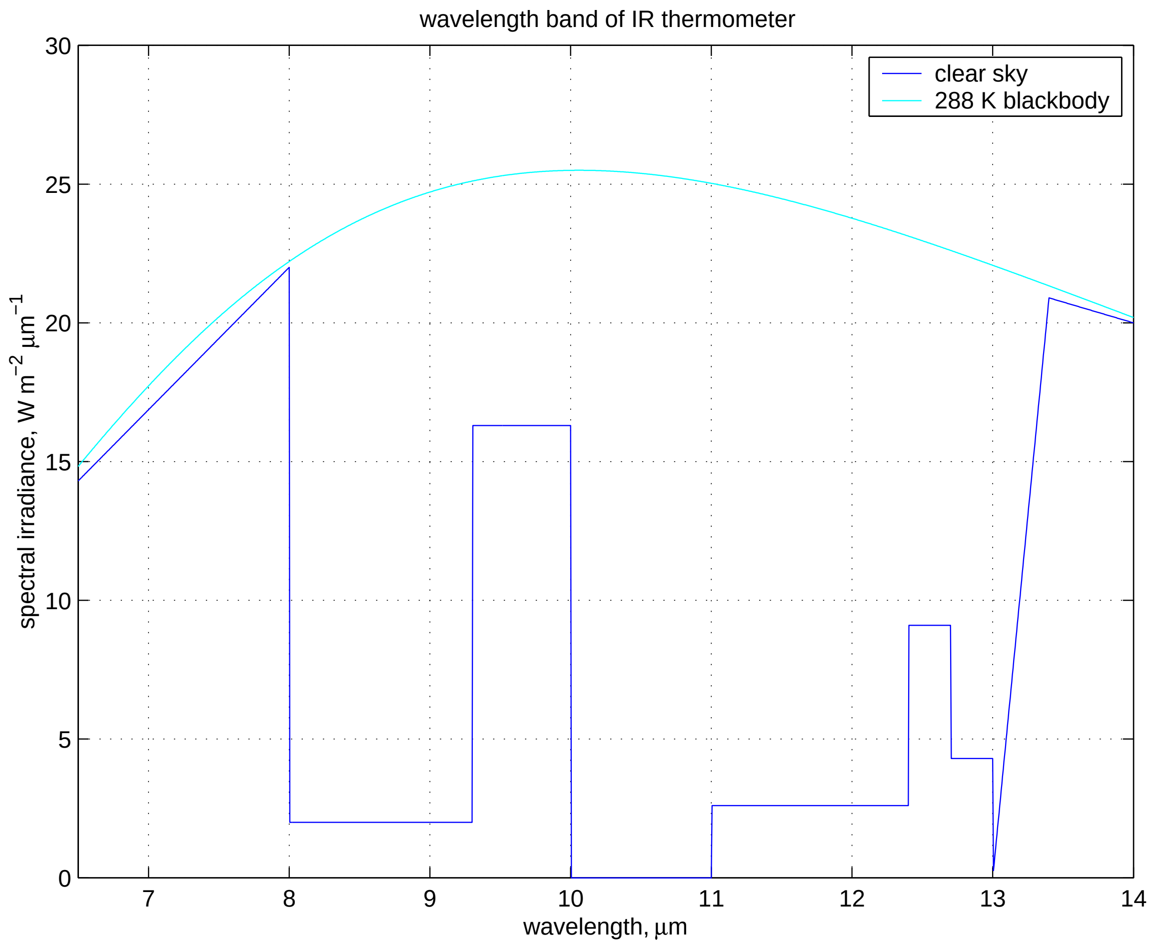

Figure 2.23: Spectral irradiance of a clear sky of effective temperature $T_{sky} = 288$ K within the band of the IR thermometer. Approximated from Figure 10.6 of *Campbell and Norman* [1998]. Blackbody irradiance is also plotted.

found from (2.26) and (2.27):

$$T_{sky} = \left[\frac{I_{sky,4-50}}{1.72\sigma \left(w_{air}/T_{air} \right)^{1/7}} \right]^{1/4}. \tag{2.28}$$

All of the variables in (2.28) were measured in REBEX–8 and –8x: $I_{sky,4-50}$ by the pyrgeometer; and w_{air} and T_{air} by the air temperature / relative humidity probe at 7.8 m.

The emissivity of the sky in the band of the IR thermometer, e_{sky}, was found using the graph of clear sky spectral irradiance versus wavelength when $T_{sky} = 288$ K in Figure 10.6 of *Campbell and Norman* [1998]. An approximation of the 6.5 to 14 μm band of this figure is reproduced here in Figure 2.23. Integrating the total irradiance from the atmosphere in the 6.5 to 14 μm band and dividing by the irradiance of a 288 K blackbody in the same

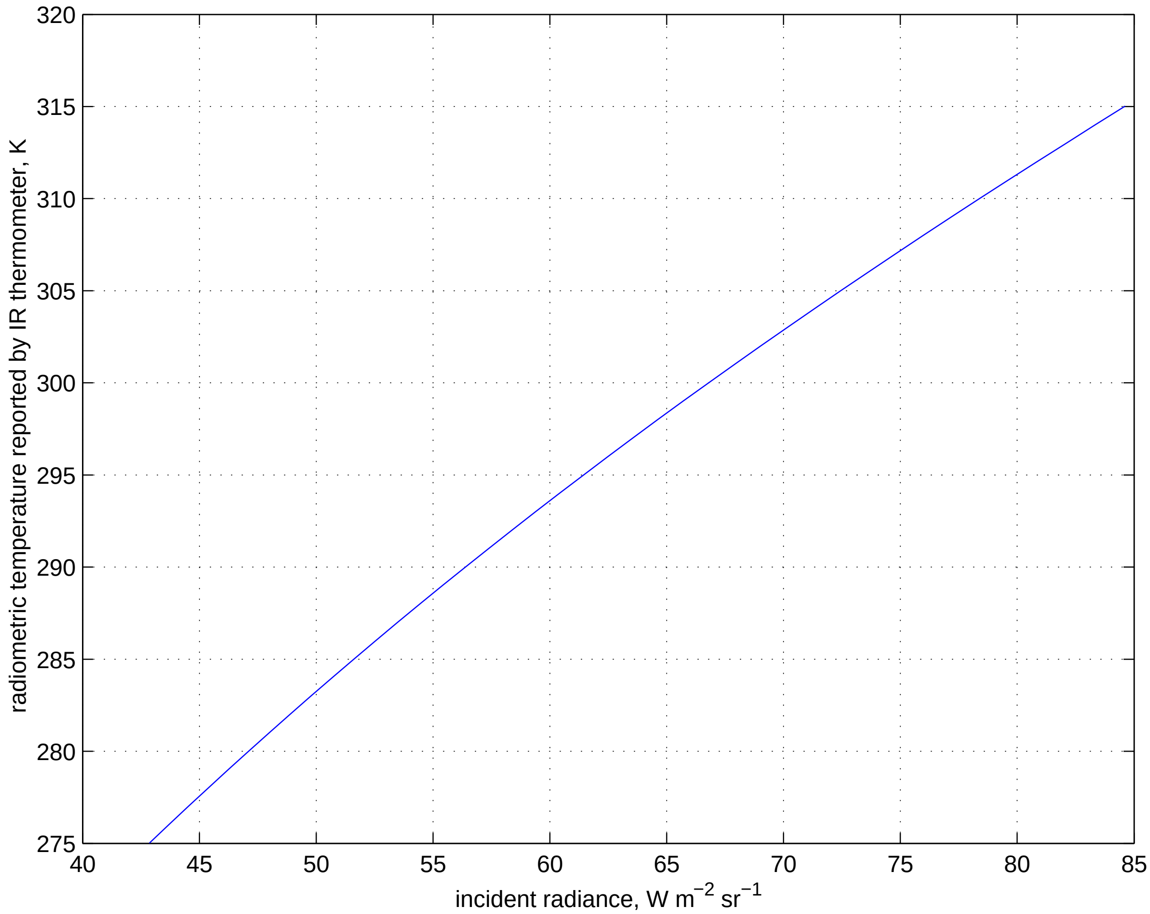

Figure 2.24: Radiometric temperature reported by an IR thermometer as a function of incident radiance.

band resulted in $e_{sky} = 0.383$. Finally,

$$I_{sky} = e_{sky} I_B(T_{sky}) \tag{2.29}$$

where $I_B(T_{sky})$ is the irradiance of a blackbody of temperature T_{sky} in the band of the IR thermometer.

Blackbody radiance at temperature T within a specific band λ_1 to λ_2 can be found by using an equivalent form of (1.5) in terms of wavelength instead of frequency:

$$R_B = \int_{\lambda_1}^{\lambda_2} \frac{2hc^2/\lambda^5}{\exp\left(hc/\lambda kT\right) - 1}\, d\lambda. \tag{2.30}$$

Since blackbody radiance is independent of angle, $I_B = \pi R_B$. To find the apparent radiometric temperature reported by the IR thermometer, (2.30) must be inverted: given an incident radiance, a blackbody of what temperature would produce this radiance? The relationship between the radiometric temperature reported by the IR thermometer as a function of incident radiance was computed numerically and is shown in Figure 2.24.

From analysis of downwelling solar radiation measured by the pyranometer, thirteen clear sky days were identified during REBEX–8x. The coolest effective sky temperature, T_{sky}, calculated for these clear days was 279 K. This occurred the morning of a microwave radiometer calibration. Field notes confirm a clear sky that morning. The warmest effective sky temperature calculated for these clear days was 307 K. The maximum difference between R and R_B in (2.25) will be for the lowest possible value of e_s and the lowest value of T_{sky}. For a Lambertian surface of temperature $T_s = 300$ K, emissivity $e_s = 0.98$, and sky effective temperature $T_{sky} = 279$ K, the radiometric temperature reported by an IR thermometer would be 299.1 K. The smallest difference between R and R_B in (2.25) will be for the *highest* possible value of e_s and the *highest* value of T_{sky}. For a Lambertian surface of temperature $T_s = 300$ K, emissivity $e_s = 0.99$, and sky effective temperature $T_{sky} = 307$ K, the radiometric temperature reported by an IR thermometer would be 299.7 K. Hence, the maximum difference between the actual radiometric temperature of the vegetation canopy and the radiometric temperature reported by the IR thermometer is about 0.9 K. This difference will always be at least 0.3 K on clear sky days.

2.4.2 Soil Temperature

Soil temperature measurements at 1.5 and 4.5 cm were made with thermocouples and thermistors, respectively. Four thermocouple measurements, made in adjacent rows, were averaged together to measure soil temperature at 1.5 cm in both H and L areas. The thermocouples were encased in metal rods less than 3 mm in diameter. They were subject to the same thermocouple errors as the IR thermometers, resulting in an accuracy of ± 0.4 K or less and a precision of < 0.1 K. Each H and L measurement at 4.5 cm was the average of 3 separate measurements made in adjacent rows.

2.4.3 Summary

Table 2.4 lists the accuracy and precision of instruments during REBEX–8 and –8x. In some cases, more than one of the same type of instrument were used to measure a specific variable. For these cases, a second row lists the accuracy and precision of the averaged data on the plot–scale. For example, three 107 temperature probes were used to measure 4.5 cm soil temperature. If the accuracy of one probe is $< \pm 0.2$ K, then the accuracy of the average of three of these probes is less than $\pm 0.2/\sqrt{3} = \pm 0.1$ K. The accuracy and precision of individual CS615 Water Content Reflectometers were not determined. For the vegetation IR temperature, only instrument, and not emissivity, errors are given.

Table 2.4: Accuracy and precision of instruments used in REBEX–8 and –8x. In some cases, more than one of the same type of instrument were used to measure a specific variable. For these cases, a second row lists the accuracy and precision of the averaged data on the plot–scale.

Instrument	*Manufacturer*	*Variable*	*Accuracy*	*Precision*
microwave radiometers	Univ. of Michigan	1.4 GHz brightness	± 2 K	0.4–1.7 K
ThetaProbe ML2x	Delta–T Devices	0–6 cm volumetric soil moisture	± 0.01 m^3 m^{-3}	0.02 m^3 m^{-3}
			± 0.01 m^3 m^{-3}	$<< 0.01$ m^3 m^{-3}
CS615 Water Content Reflectometers	Campbell Scientific	0–3 & 3–6 cm vol. soil moisture		
			$< \pm 0.02$ m^3 m^{-3}	$<< 0.01$ m^3 m^{-3}
107 Temperature Probes	Campbell Scientific	soil temperature @ 4.5 cm	$< \pm 0.2$ K	< 0.1 K
			$< \pm 0.1$ K	< 0.1 K
TCAV Soil Thermocouple Probes	Campbell Scientific	soil temperature @ 1.5 cm	$< \pm 0.4$ K	< 0.1 K
			$< \pm 0.3$ K	< 0.1 K
TE525 Tipping Bucket Rain Gauge	Texas Electronics	precipitation	$\pm 1\%$	± 0.3 mm
PSP pyranometer	Eppley	downwelling solar radiation	± 1–2%	< 1 W m^{-2}
PIR pyrgeometer	Eppley	downwelling atmospheric radiation	$\pm 3\%$	< 1 W m^{-2}
014A anemometer	Met–One	wind speed @ 10 m	$\pm 1.5\%$	< 0.1 m s^{-1}
HMP35C Air Temp. / RH Probe	Vaisala	air temperature @ 7.8 m	$< \pm 0.4$ K	< 0.1 K
HMP35C Air Temp. / RH Probe	Vaisala	relative humidity @ 7.8 m	± 2–3% RH	$< 0.1\%$ RH
Precision IR Thermocouple Transducers	Apogee	soil & vegetation IR temperature	$< \pm 0.7$ K	< 0.1 K

CHAPTER 3

The Nature of Absorption, Emission, and Volume Scattering in Field Corn at 1.4 GHz

Chapter 3 begins with a discussion of the dielectric properties of a field corn canopy as a function of orientation, both in azimuth and elevation. It also includes the procedure used to show that the zero–order radiative transfer model is unable to predict the correct change in brightness temperature with incidence angle unless some degree of scattering is allowed and the canopy is considered to be anisotropic in elevation. Finally, a new semi–empirical zero–order model is formulated for mature corn and the variation of its parameters with incidence angle and polarization is discussed.

3.1 Row Anisotropy

Although spatially heterogeneous on meter scales due to the variable size of plant constituents such as stems, leaves, and ears, a field corn canopy can be considered quasi–continuous at 1.4 GHz [*Ulaby et al.*, 1987] and hence treated as a single dielectric layer. Dielectric anisotropy can result in the polarization of electromagnetic waves. As a result, emitted brightness of anisotropic media can depend upon the propagation direction. Is a field corn canopy anisotropic in azimuth at 1.4 GHz? Or, in other words, is the brightness temperature a function of row direction?

Because of the significant row structure of field corn, it would seem so. The stems and ears, essentially moist dielectric rods with thicknesses a significant fraction of the wave-

Figure 3.1: Truck–mounted radiometers on day of year 178. Antennae oriented at $\theta = 35°, \phi = 60°$. Micro–meteorological station tower can be seen in the background.

length, are arranged in uniform rows with row spacings of three to four wavelengths at 1.4 GHz. This arrangement is expected to enhance polarization within the row. For example, *O'Neill et al.* [1984] presented 1.4 GHz brightness temperature data of mature corn as a function of the orientation of cut stalks stripped of leaves and laid on the ground. *Lee and Kong* [1985] used an anisotropic random medium model to analyze a subset of the data and were able to reproduce the general trends observed. For horizontally–polarized (H–pol) brightness temperature, approximately +12 K and +23 K differences between plants oriented perpendicular ($\phi = 90°$) and parallel ($\phi = 0°$) to the look direction at incidence angles of $\theta = 10°$ and $\theta = 40°$, respectively, were observed. For vertically–polarized (V–pol), plants oriented parallel to the look direction had higher brightness temperatures. Differences between plants oriented perpendicular and parallel to look direction were approximately -20 K and -14 K at incidence angles of $\theta = 10°$ and $\theta = 30°$, respectively.

In another study, *Macelloni et al.* [1996] arranged thin dielectric cylinders (0.27 cm

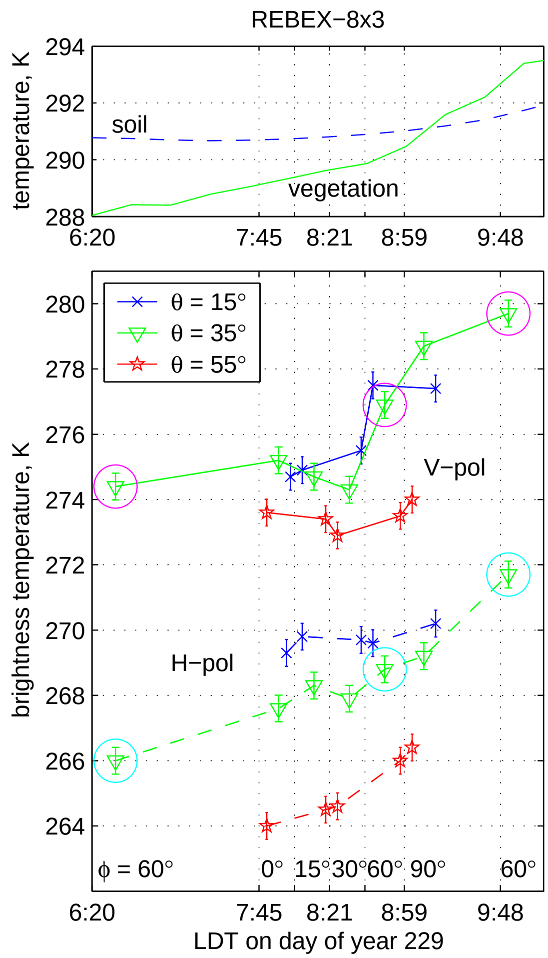

Figure 3.2: Time sequence of H–pol and V–pol brightness temperature as a function of angle with respect to row direction (ϕ) during REBEX–8x3. Errorbars of $\pm$NEΔT are included. The measurements at $\phi = 60°$ and $\theta = 35°$ are circled. Soil temperature at 1.5 cm and vegetation IR temperature are also plotted.

diameter, 20 cm length) in periodic rows on a reflecting background. At 10 GHz they found: no difference in brightness temperature between $\phi = 0°$ and $\phi = 90°$ at $\theta = 20°$ for both vertical and horizontal polarizations; +12 K and +8 K difference for V– and H–pol, respectively, at $\theta = 30°$; a +10 K and +8 K difference at $\theta = 40°$, and a +10 K and +6 K difference at $\theta = 50°$. Although the frequency of observation was 10 GHz, the electrical size of the dielectric cylinders used in this study is similar to the electrical size of stems and ears at 1.4 GHz.

Only one direct measurement of the brightness temperature of a field corn canopy with

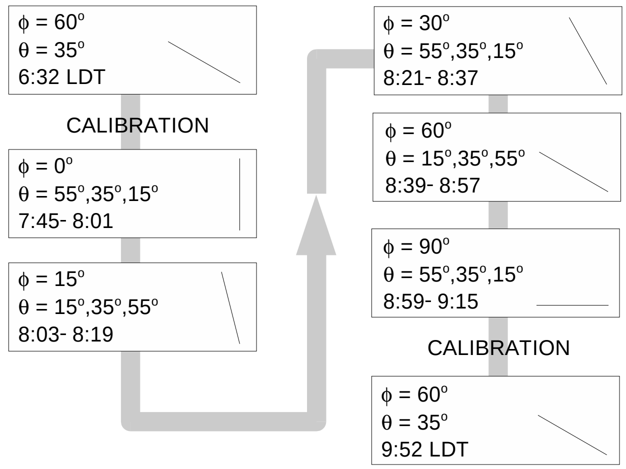

Figure 3.3: Measurement procedure during REBEX–8x3.

respect to row direction has been reported. *Brunfeldt and Ulaby* [1986] observed a $+10$ K difference between $\phi = 90^\circ$ and $\phi = 0^\circ$ for V–pol brightness temperature at 2.7 GHz for a 5.5 kg m^{-2} vegetation column density corn crop. Row direction experiments were conducted at several points during REBEX–8 and REBEX–8x (Figure 3.1). Measurements of H–pol and V–pol brightness at 1.4 GHz collected during REBEX–8x3 for a mature corn canopy (vegetation column density of 8.0 kg m^{-2}) at several different angles with respect to row direction and angles of incidence are plotted in Figure 3.2. These measurements were made during a period of three and a half hours starting at 6:30 LDT (Local Daylight Time) on day of year 229. During the previous night, the radiometers had been left recording data at $\phi = 60^\circ$ and $\theta = 35^\circ$. The last measurements at this position, at 6:32, are the first two points on the left in Figure 3.2. See Figure 3.3 for a description of the measurement procedure. Three measurements of brightness temperature, each separated by two minutes, were made at each combination of ϕ and θ in order to verify the measurement precision. See Table 3.1 for a description of footprint size relative to row spacing.

The general increase in brightness temperatures over the measurement period evident in Figure 3.2 was due to slowly changing soil and vegetation temperatures. In order to remove this effect, the three $\phi = 60^\circ$ and $\theta = 35^\circ$ points for both H–pol and V–pol at 6:32, 8:49, and 9:52 LDT were used to construct two second–degree polynomials. These two

Table 3.1: Radiometer footprint size in terms of the number of rows of corn that would lie inside of the footprint. Maximum canopy height was 3.0 m.

	$\phi = 0°$		$\phi = 90°$	
	$z = 0$ m	$z = 3.0$ m	$z = 0$ m	$z = 3.0$ m
$\theta = 15°$	6 rows	4 rows	6 rows	5 rows
$\theta = 35°$	6 rows	4 rows	9 rows	7 rows
$\theta = 55°$	5 rows	3 rows	15 rows	10 rows

polynomials are an approximation of the change in brightness temperature over time at $\phi = 60°$ and $\theta = 35°$ for each polarization. Subtracting these polynomials from the measured brightness temperatures revealed the variation in microwave brightness as a function of row direction, referenced to the brightness temperature at $\phi = 60°$. In order to remove the temperature change effects from the $\theta = 15°$ and $\theta = 55°$ data, the relevant polynomial, according to polarization, was shifted either up or down in order to match the recorded data at $\phi = 60°$ and $\theta = 15°$ and 55°. In using this compensation procedure derived at $\theta = 35°$ the assumption is made that the weighting of soil and vegetation temperatures is the same at $\theta = 15°$ and $\theta = 55°$. This is not exactly true. At $\theta = 15°$, the soil contribution to the brightness temperature is slightly larger than at $\theta = 35°$, while at $\theta = 55°$, the soil contribution is slightly smaller. In either case, the vegetation contribution dominates and the change in relative contribution is small. Figures 3.4 and 3.5 present the results.

Surprisingly, field corn brightness at 1.4 GHz was *not* a strong function of angle with respect to row direction until senescence. As the corn was growing and when it was fully mature, the observed variation in brightness temperature with ϕ was very small, about 1 to 2 K. Since there were no obvious patterns in these variations, they were probably the result of radiometer precision, the vegetation and soil compensation method, and soil and canopy variability. Despite the absence of a complete set of data for REBEX–8x1 and –8x2, there is no reason to doubt that H–pol brightness temperature is also independent of row direction during this period. When the corn was fully senescent in early October during REBEX–8x4, a consistent pattern did emerge at all incidence angles: H–pol brightness temperatures were highest parallel to the rows at $\phi = 0°$, while V–pol brightness temper-

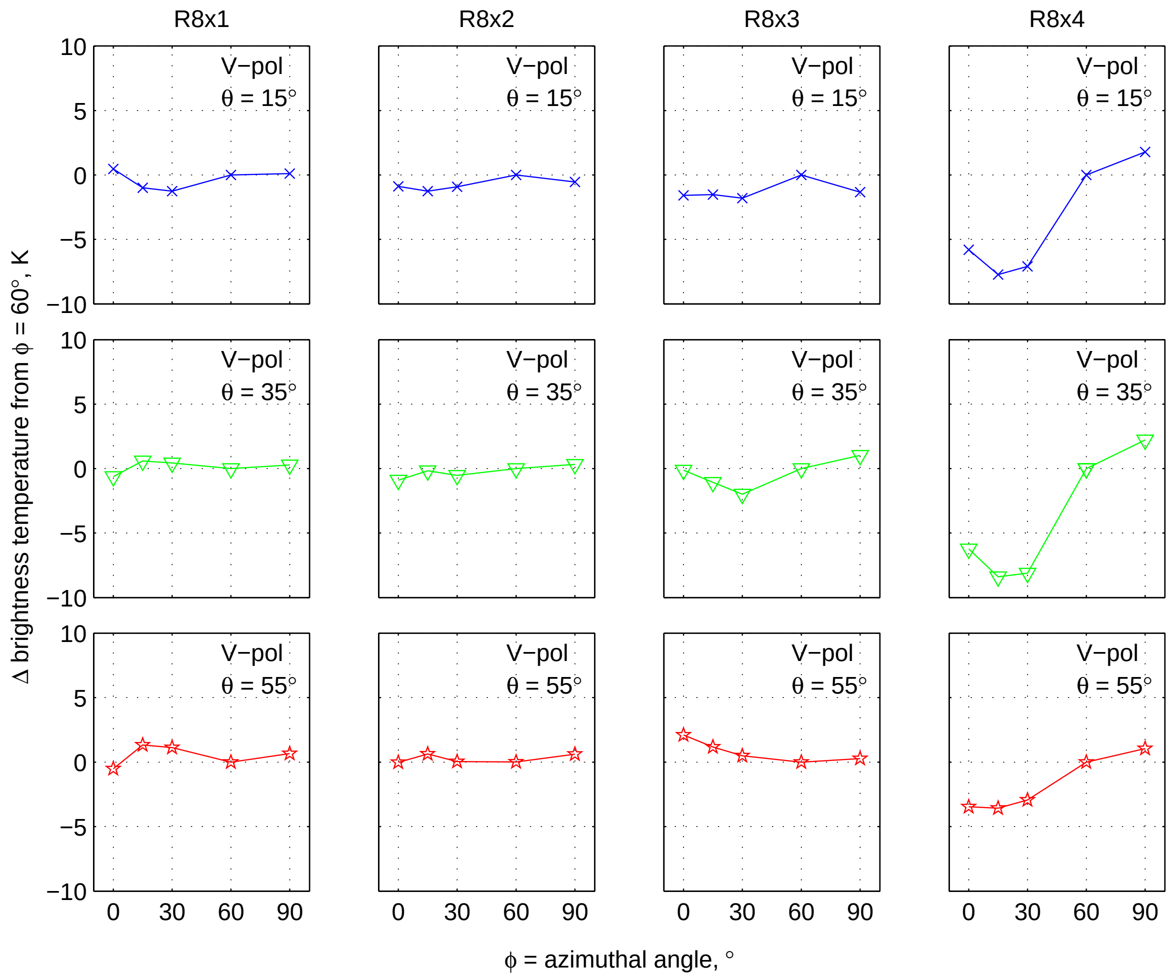

Figure 3.4: Change in V–pol brightness temperature from $\phi = 60^\circ$ as a function of angle with respect to row direction during REBEX–8x1, –8x3, –8x3, and –8x4. The size of the markers on the data are approximately the same size as ±NEΔT and therefore errorbars are not included.

atures were highest perpendicular to the rows at $\phi = 90^\circ$. The V–pol pattern was more complex: although brightness temperatures were lower parallel than perpendicular to the row, the actual minima appeared to be near $\phi = 15^\circ$.

One obvious difference between *O'Neill et al.* [1984] and *Macelloni et al.* [1996] and a real corn canopy is the presence of leaves. At substantially higher frequencies (> 10 GHz), one might in fact expect the brightness temperature to be independent of row direction during the growing season because at shorter wavelengths leaves may "hide" the stems and ears. At 1.4 GHz the leaves are expected to be rather transparent and hence the internal

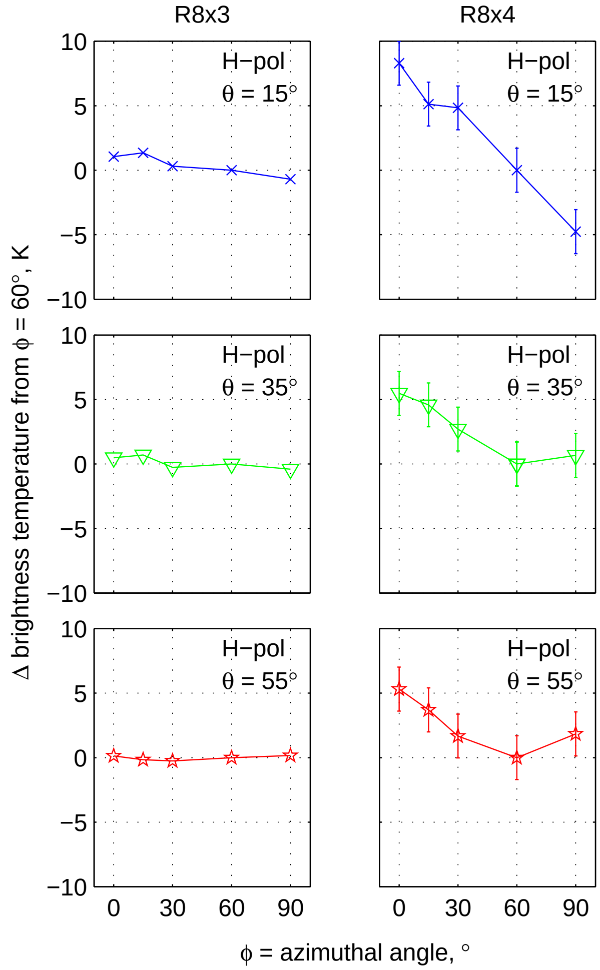

Figure 3.5: Change in H–pol brightness temperature from $\phi = 60^\circ$ as a function of angle with respect to row direction during REBEX–8x3 and –8x4. Errorbars on the REBEX–8x4 data are $\pm$NEΔT. The size of the markers on the REBEX–8x3 data are approximately the same size as $\pm$NEΔT and therefore errorbars are not included.

structure of the canopy should have a significant impact on the brightness temperature. Instead, at 1.4 GHz it appears that leaves either mask the internal, stem–dominated structure within the canopy, or they have a "smoothing" effect. Even the appearance of ears between REBEX–8x2 and REBEX–8x3 did not affect the azimuthal dependence of the brightness temperature. When the canopy dried out after the onset of senescence, the leaves lost their moisture and became essentially invisible at microwave wavelengths (Figure 3.6). The stems and ears, which still contained significant moisture, were left "uncovered" in a row arrangement which was anisotropic in azimuth, as previously expected.

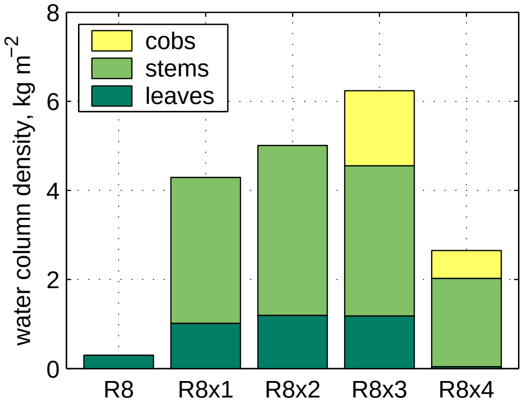

Figure 3.6: Distribution of water column density during each REBEX.

3.2 Volume Scattering

The stems and ears of field corn have sizes of the same order of the wavelength, and hence some degree of scattering within the canopy will occur. What is the nature of this volume scattering? Despite their arrangement in well–defined rows, the location of scatterers relative to one another is random with respect to the wavelength. As a result, the electric field at any one point within the canopy is the superposition of waves that have no coherence with each other. In the soil, changes in the dielectric constant due to changes in moisture, as long as they are gradual and not abrupt, also destroy wave coherence. Under these conditions, it is appropriate to use incoherent radiative transfer to model the microwave brightness.

Within a medium, the incremental change in brightness temperature at each point is the sum of three effects [*Ulaby et al.*, 1981-1986]:

$$dT_B(\hat{s}) = -\kappa_e\, T_B(\hat{s})\, ds + \kappa_a\, T\, ds + \frac{\kappa_s}{4\pi} \int_{4\pi} \psi(\hat{s},\hat{s}')\, T_B(\hat{s}')\, d\Omega'\, ds. \tag{3.1}$$

First, brightness in the $\hat{s}$ direction is attenuated in proportion to the medium's extinction coefficient, κ_e. Extinction is due to both absorption by the medium (κ_a) and scattering by particles within the medium (κ_s). Second, the medium emits according to its physical temperature, T, in order to maintain thermodynamic equilibrium. Finally, brightness from all other directions $\hat{s}'$ is scattered into the $\hat{s}$ direction according to the normalized phase function $\psi(\hat{s}, \hat{s}')$.

In the simplest case, a vegetated surface can be modeled as a single isothermal layer of vegetation with diffuse boundaries over a soil half space. After applying appropriate boundary conditions, the zero–order solution of (3.1) can be written

$$T_B = T_{Bsoil} + T_{Bcanopy\uparrow} + T_{Bcanopy\downarrow} \tag{3.2}$$

where

$$T_{Bsoil} = T_{soil} \times (1 - R_{soil}) \times L \tag{3.3}$$

$$T_{Bcanopy\uparrow} = (1-\alpha)(1-L)T_{canopy} \tag{3.4}$$

$$T_{Bcanopy\downarrow} = (1-\alpha)(1-L)T_{canopy} \times R_{soil} \times L. \tag{3.5}$$

T_{Bsoil} represents the soil contribution to the total brightness temperature. $T_{Bcanopy\uparrow}$ and $T_{Bcanopy\downarrow}$ represent upwelling and reflected downwelling emission from the vegetation canopy, respectively. T_{soil} is the effective soil temperature; R_{soil}, an effective reflectivity of the soil surface; $L = \exp(-\tau/\cos\theta)$, the transmissivity of the vegetation layer; $\tau = (\kappa_a + \kappa_s)\,h = \kappa_e h$, the canopy optical depth; h, the canopy height; $\alpha = \kappa_s/\kappa_e$, the single-scattering albedo; and T_{canopy}, the canopy temperature. Reflected sky brightness, which is only a few Kelvin at 1.4 GHz, is neglected. R_{soil} is a function of volumetric water content. τ and α are determined primarily by the structure and water content of the canopy.

The zero–order solution assumes weak scattering within the canopy: either $\psi(\hat{s}, \hat{s}') \approx 0$, which means little power is scattered into the forward direction; κ_s is very small, meaning either the number or the extinction cross section of the scatterers is small; or $\alpha << 1$, such that $\kappa_s << \kappa_a$. A non–zero single-scattering albedo produces a lower effective vegetation temperature to account for limited volume scattering. Many researchers in the past have used this model for field corn [*Jackson et al.*, 1982; *Mo et al.*, 1982; *Brunfeldt and Ulaby*, 1986; *Jackson and O'Neill*, 1990; *O'Neill et al.*, 1996; *Jackson et al.*, 1997; *Crosson et al.*, 2002] under the assumption that scattering is small at 1.4 GHz. Is this indeed true? Can a

Table 3.2: Canopy and soil properties during brightness temperature measurements at $\phi = 60°$ and $\theta = 15°$, 35°, and 55°.

	R8	-x1	-x2	-x3	-x4
IR vegetation temp, K	284	292	290	290	278
IR soil surface temp, K	284	293	290	291	278
soil temp @ 1.5 cm, K	285	293	289	291	281
soil temp @ 4.5 cm, K	285	293	291	291	283
vol soil moist 0-3 cm, $m^3\ m^{-3}$	0.22	0.13	0.10	0.15	0.25
vol soil moist 3-6 cm, $m^3\ m^{-3}$	0.25	0.20	0.18	0.19	0.28

field corn canopy be considered a weakly–scattering canopy at 1.4 GHz so that (3.2) can be used?

When considering a scattering layer over a homogeneous half–space, *England* [1975] showed that scatter–induced change in brightness temperature can be tens of Kelvin. Volume scattering is a function of the dielectric contrast between the scatterers in the medium, the dielectric loss of the scatterers, the size of scatterers relative to wavelength, and the fraction of volume filled by the scatterers. If the dielectric constant of the half–space is not significantly larger than the dielectric constant of the scattering layer (as in the case of a vegetation layer over a moist soil half–space) the presence of scatterers reduces the brightness temperature. This phenomena is called *scatter darkening*. For example, *Liou et al.* [1999] observed scatter darkening in prairie grass. They were able to accurately model 19 GHz brightness with a purely absorptive volume emission model, but model predictions of 37 GHz brightness were too high.

Most of the experimental validation of the zero–order model has been at incidence angles close to nadir where the effects of scattering in the canopy are least. One way to test the assumption of weak scattering is to examine the change in brightness temperature with incidence angle. As the impact of the canopy on the microwave brightness increases at progressively larger angles of incidence, can the zero–order solution correctly recreate what is observed experimentally?

Observed 1.4 GHz brightness temperature from each REBEX at $\phi = 60°$ and incidence angles of $\theta = 15°$, 35°, and 55° were compared with the predictions of the zero–order model

(3.2). These measurements were made near dawn as part of the row direction experiments. All three incidence angles were measured within a period of less than 20 minutes. Recorded canopy temperatures, soil temperatures, and moisture are listed in Table 3.2. The average of recorded vegetation and soil IR temperatures were used for T_{canopy}. T_{soil} was computed using the parameterization of *Wigneron et al.* [2001]:

$$T_{soil} = T_{\infty} + \left(T_{surf} - T_{\infty}\right)\left(\theta_v / w_0\right)^{B_T} \tag{3.6}$$

where: T_{∞} is a deep soil temperature, typically at 50 cm; T_{surf} is the soil temperature near the surface; θ_v is the soil surface water content; and w_0 and B_T are parameters which depend on the choice of depth for T_{surf} and θ_v. This is a variation the model proposed by *Choudhury et al.* [1982] parameterized specifically for the agricultural fields in which they collected their data. The soil texture of these fields (62% silt, 11% sand, and 27% clay) closely matches that of REBEX–8 (55% silt, 16% sand, and 29% clay). Soil temperature at 50 cm was not measured during REBEX–8 but during the previous summer in a nearly identical corn field planted and cultivated using the same practices 1 km north of the REBEX–8 site. At this depth, soil temperature does not vary diurnally and is almost constant for periods of weeks at a time. Depths of 1.5 cm and 0–3 cm were chosen for T_{surf} and θ_v, respectively, resulting in $w_0 = 0.794$ and $B_T = 0.258$. In all cases, T_{soil} and soil temperature measured at 1.5 cm were within 2 K. A dielectric model [*Dobson et al.*, 1985] and recorded 0–3 cm soil moisture were used to calculate the specular reflectivity of the soil at the site. The optical depth was computed using the model of *Jackson et al.* [1982] and *Schmugge and Jackson* [1992] which relates τ directly to the water column density, M_w, the mass of water in the vegetation per square meter:

$$\tau = b M_w. \tag{3.7}$$

A value of $b = 0.115$, appropriate for corn at 1.4 GHz when $\alpha = 0$, was used [*Jackson and O'Neill*, 1990]. Figures 3.7 and 3.8 compare the observations with the model results.

As an aside, note that the temperatures listed in Table 3.2 are nearly uniform, especially

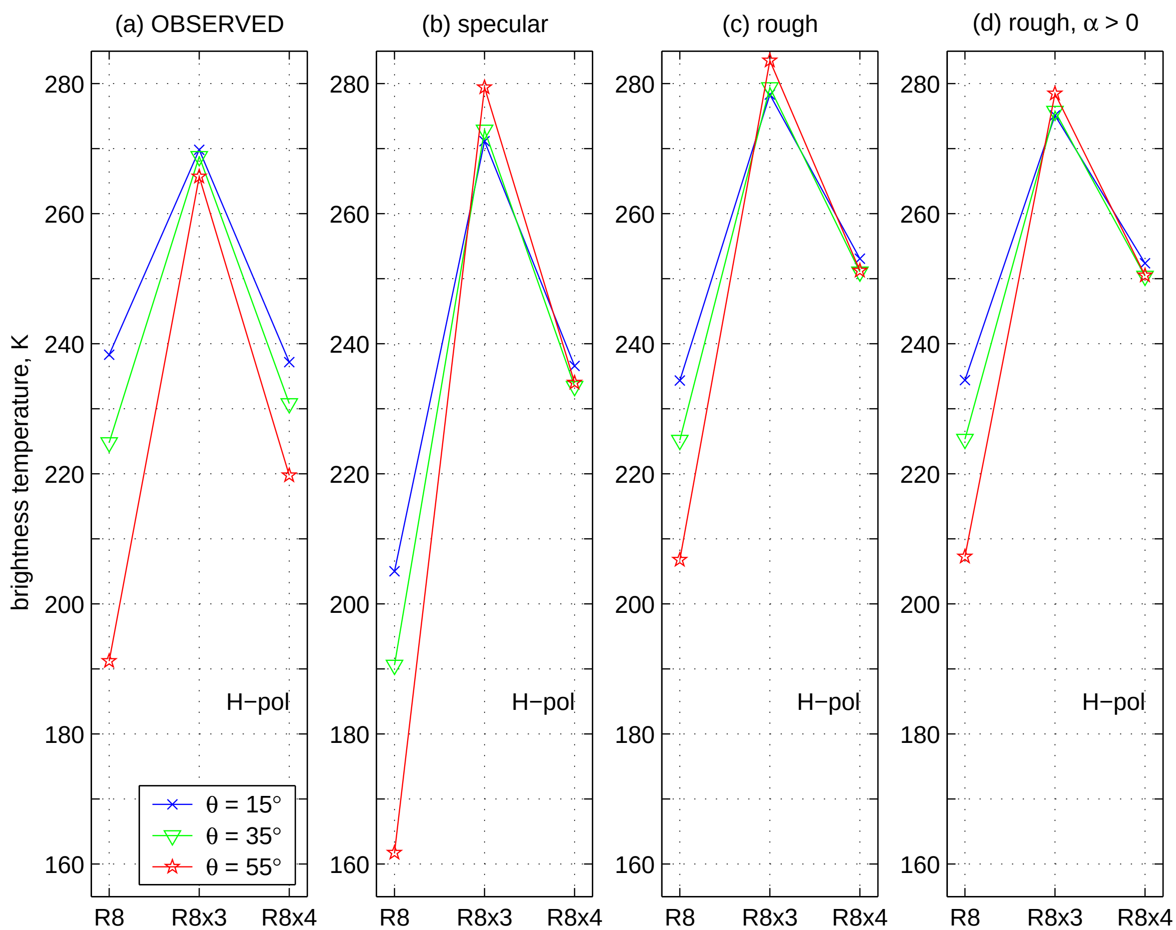

Figure 3.7: Observed (a) and modeled (b, c, and d) H–pol brightness temperature at $\phi = 60°$ during REBEX–8, –8x3, and –8x4. For the model results: (b), the soil surface is specular; (c), the soil surface is rough; and (d), the soil surface is rough and $\alpha > 0$.

during REBEX–8, REBEX–8x1, and –8x3. Thus any effect of temperature gradients within the canopy and soil on the microwave brightness was negligible. The emissivity of the land surface, e, defined as the ratio of brightness temperature to physical temperature, is approximately $e \approx 269$ K / 291 K $= 0.92$ for H–pol and $e \approx 277$ K / 291 K $= 0.95$ for V–pol during REBEX–8x3. The V–pol emissivity during REBEX–8x1 was also about 0.95.

For H–pol, three different versions of the zero–order model were used to illustrate the effect of different physical processes on the brightness temperature. In the first version, part (b) of Figure 3.7, the soil surface was modeled as specular and the single–scattering albedo, α, was set to zero. In comparison to part (a), the observed H–pol brightness temperature, it is obvious that the REBEX–8 predictions are too low, but the change with incidence angle θ is correct. When the amount of vegetation is small, the total brightness temperature is dominated by (3.3). The measurements and model both followed the Fresnel law: the brightness temperature was highest near nadir and gradually decreased as the incidence angle increased.

When the canopy was mature during REBEX–8x3, the zero–order model no longer correctly predicted the change in H–pol brightness temperature as a function of θ. This is illustrated in part (a) and (b) of Figure 3.7 by the lines linking the REBEX–8 and –8x3 brightness temperatures. In the model predictions, the lines cross. At large water column densities, canopy emission composes a higher fraction of the total brightness temperature than emission from the soil. As the path length through the canopy increases at larger angles of θ, the zero–order model predicts canopy emission to increase at a rate which out paces the decrease in soil microwave brightness. The result is that in weakly scattering vegetation canopies, microwave brightness should *increase* with θ when the water column density is large. This is opposite what was observed. For the field corn canopy, the brightness temperature *decreased* with θ, a sign of scatter darkening in the canopy.

In the second version of the zero–order model, part (c) of Figure 3.7, the soil was modeled more realistically as rough surface using the model [*Choudhury et al.*, 1979; *Wang et al.*, 1980a]

$$R_{rough} = R_{spec} \times \exp(-h_s) \tag{3.8}$$

where R_{spec} is the specular reflectivity and h_s is an effective roughness parameter. h_s was computed using the formulation of *Wigneron et al.* [2001]:

$$h_s = A\,\theta_v{}^B (\sigma_s / l_c)^C \tag{3.9}$$

where: $A = 0.5761$, $B = -0.3475$, and $C = 0.4230$ are empirical parameters; θ_v is the volumetric soil moisture in $\mathrm{m}^3\ \mathrm{m}^{-3}$ of the 0–3 cm soil layer; σ_s is the standard deviation of soil surface height; and l_c is the soil surface correlation length. This empirical formulation of h_s was made using data collected in bare agricultural fields of varying roughness at incidence angles of $\theta = 10°$, $20°$, $30°$ and $40°$. Soil surface roughness was measured with a laser profiler the previous summer in late August. Four meter–long transects perpendicular to row direction were used to calculate a σ_s of 14 mm and a l_c of 85 mm, which are representative of the conditions during REBEX–8x3. According to *Oh and Kay* [1998], surface segments totaling $40\sigma_s$ and $200 l_c$ must be used to accurately characterize these surface parameters. While this condition was satisfied for σ_s, l_c must be considered a rough estimate. These values are similar to those measured by *Wigneron et al.* [2001] for their field 18 with $\sigma_s = 19$ mm and $l_c = 66$ mm. Again, the soil texture of the fields in *Wigneron et al.* [2001] was close to the texture of the REBEX–8 field.

As expected, the REBEX–8 model predictions increased since the emissivity of a rough surface is higher than that of a smooth one. The predictions were more in line with the observations of part (a). The large difference in observed and modeled brightness temperatures at $\theta = 55°$ is likely due to different soil roughness conditions during REBEX–8 (before cultivation) and REBEX–8x (after cultivation). The range of data used to calibrate the model did not reach $\theta = 55°$ although *Wang et al.* [1980a] observed that a soil surface with significant row structure did not change the variation of brightness temperature with incidence angle significantly at H–pol. Although the absolute change in H–pol brightness temperature with θ was not correctly predicted by the model, the relative change in brightness, in keeping with the Fresnel law, was the same: brightness still decreased as the incidence angle increased.

In the the third version of the zero–order model, part (d) of Figure 3.7, α is set to 0.03 [*Jackson and O'Neill*, 1990] and the soil surface remains rough. A non–zero single–scattering albedo did decrease the difference between the three incidence angles, but the modeled change with incidence angle was still opposite that of the observations. Neither a rough soil surface nor the addition of a non–zero single–scattering albedo altered the relative position of the predictions. Furthermore, the modeled change with incidence angle

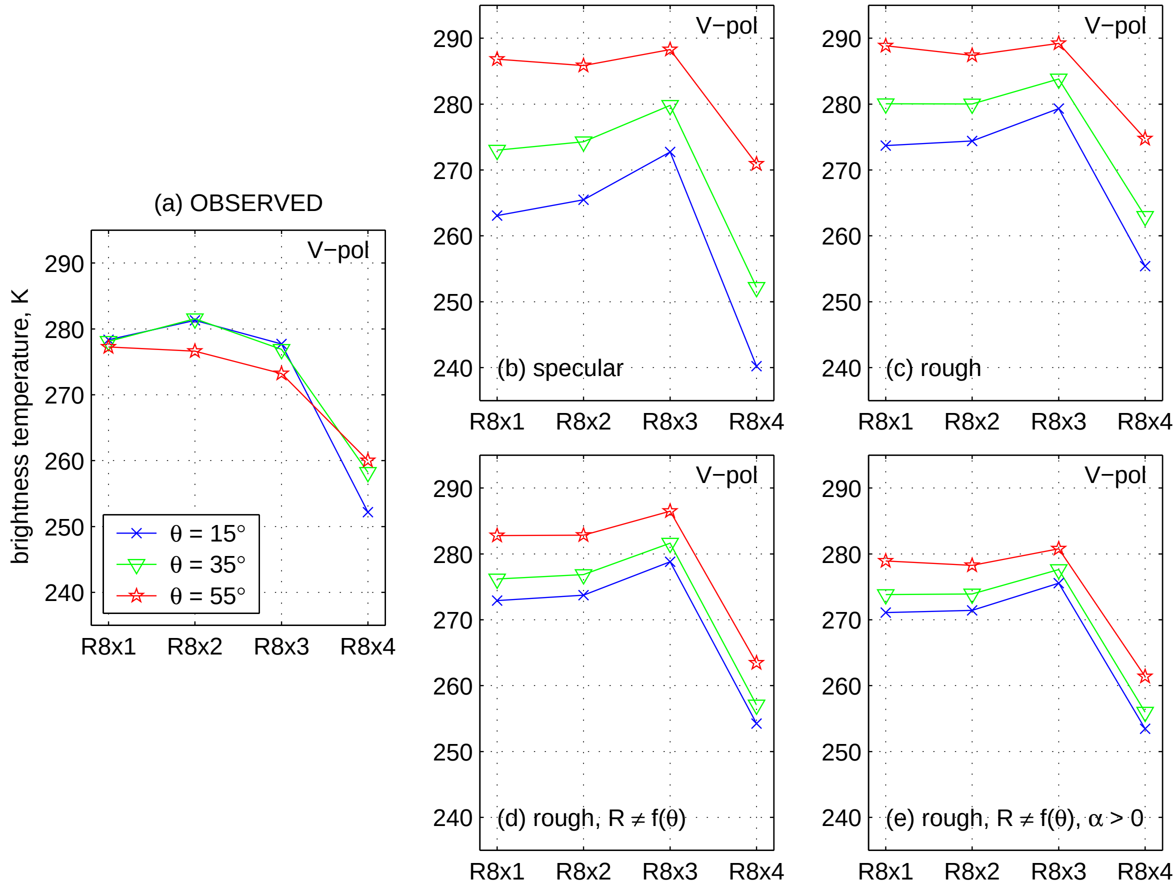

Figure 3.8: Observed (a) and modeled (b, c, d, and e) V–pol brightness temperature at $\phi = 60^\circ$ during REBEX–8x1, –8x2, –8x3, and –8x4. For the model results: (b), the soil surface is specular; (c), the soil surface is rough; (d), the soil surface is rough and R is not a function of θ; and (e), the soil surface is rough, R is not a function of θ, and $\alpha > 0$.

was opposite that predicted by the Fresnel law for brightness originating from the soil and hence must be contributed solely to the canopy. On the other hand, for REBEX–8x4 the model predicted a much smaller change in H–pol brightness temperature with incidence angle than what was observed. Evidently, when the canopy is *senescent* it is more *transparent* than predicted by the model. The change with incidence angle is more similar to that of a bare soil surface than that of a vegetation canopy.

At V–pol, volume scattering is more pronounced. Observations during REBEX–8x1, –8x2, –8x3, and –8x4 are compared with model predictions in Figure 3.8. Besides the model versions used to compare H–pol data with observations, a fourth version is used.

According to the Fresnel law, V–pol soil microwave brightness increases with θ up to the Brewster angle. The Brewster angle changes with soil moisture and roughness, but it was larger or at least very close to $\theta = 55°$ for each data point in part (a) of Figure 3.8. *Wang et al.* [1980a] observed that a soil surface with significant row structure removed much of this effect. As such, in part (d) the strong variation of the soil reflectivity with incidence angle at V–pol was removed by setting the reflectivity at $\theta = 15°, 35°$ and $55°$ equivalent to the reflectivity at $\theta = 0°$. In doing this, it also became obvious that the relative change among incidence angle must be attributed to canopy properties and not the soil.

Although a rough soil surface, removal of the Brewster angle effect, and a non–zero single–scattering albedo all reduced the differences in V–pol brightness temperature between $\theta = 15°$, $\theta = 35°$, and $55°$, the zero–order model predictions were still opposite to what was observed. The observations show the brightness decreased with incidence angle, while the model predicted brightness to increase with incidence angle. On the other hand, the model again correctly predicted the relative change with incidence angle for senescent field corn.

In summary, the zero–order model (3.2) was not able to reproduce the observed brightness temperature change with incidence angle in field corn. Significant scatter darkening was observed when the canopy was growing and mature and this darkening increased with incidence angle. At H–pol, brightness temperatures modeled with no scattering were 2 to 3 K too high at $\theta = 35°$ and 7 to 12 K too high at $\theta = 55°$ for mature corn assuming that the zero–order model can be fit to observations at $\theta = 15°$ by adjusting the semi–empirical parameters α and h_s. At V–pol, modeled brightness temperatures were 3 to 8 K too high at $\theta = 35°$ as compared to $\theta = 15°$, and 10 to 20 K too high at $\theta = 55°$ for growing and mature corn.

Table 3.3: Values of the volume scattering coefficient, κ_s in Np m^{-1}, and the single–scattering albedo, α, for a mature field corn canopy.

	H–pol		V–pol, $R_v = f(\theta)$		V–pol, $R_v \neq f(\theta)$	
	κ_s	α	κ_s	α	κ_s	α
$\theta = 0°$	0.008	0.03	0.008	0.03	0.008	0.03
$\theta = 15°$	0.017	0.060	0.005	0.019	0.004	0.015
$\theta = 35°$	0.019	0.067	0.012	0.043	0.009	0.033
$\theta = 55°$	0.025	0.086	0.021	0.074	0.018	0.064

3.3 Weakly–Scattering Zero–Order Model

If the zero–order model is to be used, a mature corn canopy must be considered anisotropic not in azimuth, but in *elevation*. The zero–order model (3.2) was adjusted to fit the REBEX–8x3 data by allowing the volume scattering coefficient, κ_s, to be non–zero and to change with incidence angle. The value of b in (3.7) was changed to 0.130 as found by *Jackson and O'Neill* [1990] for corn when using a non–zero single–scattering albedo. κ_s was increased until the model matched the data. When $\alpha \neq 0$, $\kappa_a = (1-\alpha)\, b\, M_w/h$ and $\kappa_s = \frac{\alpha}{1-\alpha}\kappa_a$. The results are presented in Table 3.3.

Jackson and O'Neill [1990] suggested a value of $\alpha = 0.03$, equivalent to $\kappa_s = 0.008$ Np m^{-1} for the canopy in REBEX–8x3. At H–pol, κ_s is found to be significantly higher and to increase with incidence angle. V–pol values are uniformly less than H–pol values at each incidence angle, both when the soil reflection coefficient is allowed to change with incidence angle, and when it is not. V–pol κ_s also increases with incidence angle. There is one inconsistency: the value of κ_s at $\theta = 15°$ was found to be less than that assumed at $\theta = 0°$. All of the values are small, satisfying the assumptions of (3.2) for a weakly–scattering canopy.

The larger values of κ_s at H–pol than at V–pol is unexpected. Since the stems are perpendicular to the plane of the soil surface, the electric field vector of V–pol brightness is parallel to the stems. Stem width is a few centimeters, a significant fraction of the 21 cm wavelength at 1.4 GHz. Hence more scattering would be expected at V–pol than at H–pol. This reasoning would also support the increase of κ_s with θ at V–pol since the cross–sectional area of the stems also increases at greater incidence angles. But scattering appears to be much more important at H–pol. Given that the stems and ears are scatterers, the leaves must be even greater scatterers, and the effect of the leaves appears to be much greater at H–pol than at V–pol.

When the leaves effectively “disappear” as the canopy senesces, the change with incidence angle at H–pol increases, almost to that of a bare soil surface. The nonscattering model in Figure 3.7 did not predict the change to be as great. There are two possible explanations. First, scattering must increase as the canopy senesces in order for the brightness to decrease at this rate with incidence angle. But if the leaves are such significant scatters at H–pol, this can not be the case. The second, and more plausible explanation, is that the canopy is simply more transparent than predicted than the nonscattering model when it is senescent and the Fresnel change with incidence angle associated with the soil surface is more apparent. Thus the leaves play important roles in both volume scattering and absorption at H–pol. These observations support the modeling results of *Wigneron et al.* [1993], who found for a soybean canopy that 1.4 GHz brightness increases with leaf volume fraction and has a significant sensitivity to vegetation gravimetric water content. At 5 GHz, when soybean leaves are electrically similar to corn leaves at 1.4 GHz, brightness was found to increase initially with leaf volume fraction, then saturate, while also being sensitive to gravimetric water content.

The volume scattering coefficients and extinction coefficients for both H– and V–pol are plotted in Figure 3.9. The behavior of κ_e is different than that observed previously. Using measurements of electromagnetic propagation through a corn canopy at 1.6 GHz, *Ulaby et al.* [1987] found that κ_e increased with incidence angle at V–pol and was constant at H–pol. Here, κ_e increases with incidence angle at *both* V–pol and H–pol.

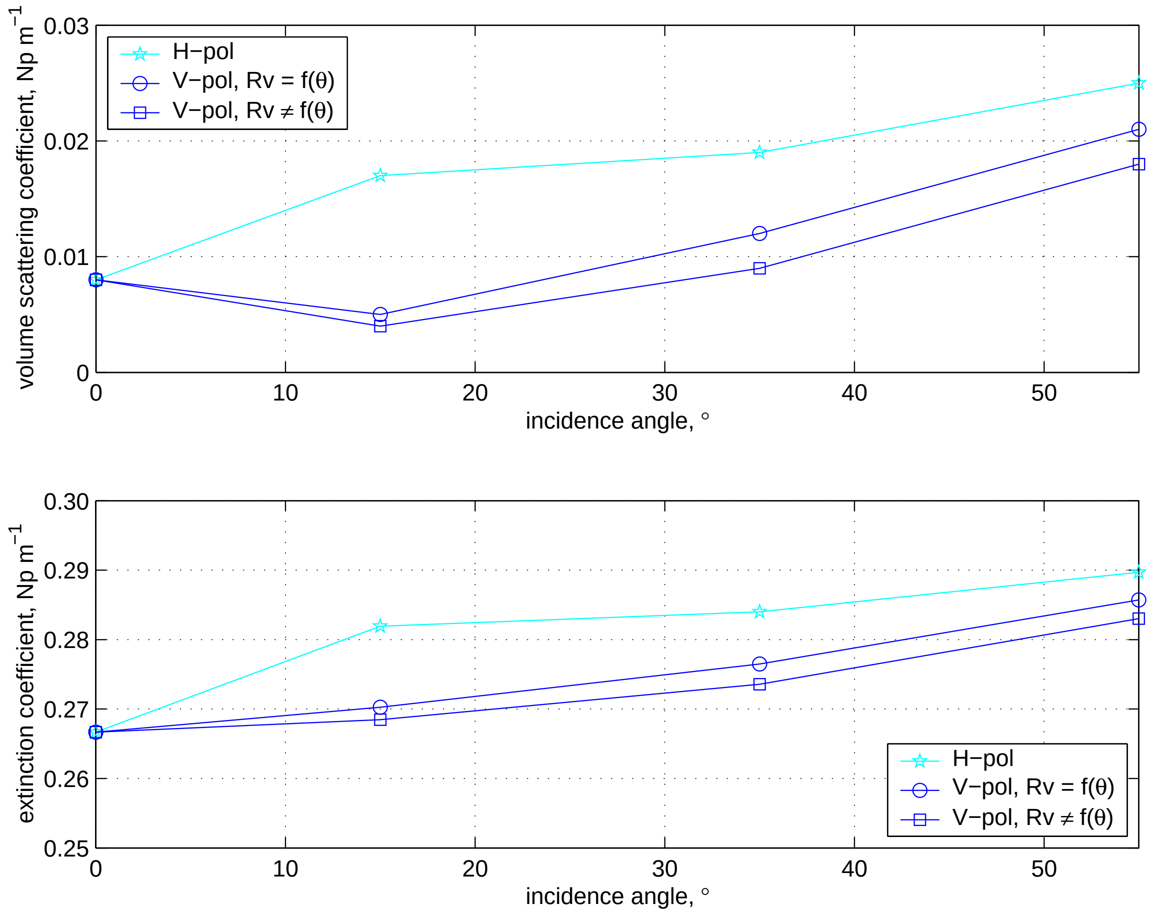

Figure 3.9: Volume scattering coefficients, κ_s (top), and extinction coefficients, κ_e (bottom), versus incidence angle.

3.4 Conclusions

The brightness temperature of a field–corn canopy at 1.4 GHz is independent of the azimuthal angle with respect to row direction soon after vegetation fraction is unity until maximum biomass is reached. As a result, the angle of the observation with respect to row direction will not affect soil moisture retrievals. When the leaf water column density becomes very small during the fall, the brightness temperature is a function of row direction. At this time a 5 to 10 K change with ϕ was observed both at H– and V–pol, depending on the incidence angle. It is also likely that a field corn canopy is essentially isotropic in azimuth at earlier points in the growing season when the leaf column density and fraction of cover are large enough compared to the stem column density. Other row crops that are less heterogeneous (such as wheat, soybeans, and cotton) are likely to have the same qualities.

Although the data presented are at a much smaller scale, the footprints of the radiometers covered several rows (Table 3.1) and the same row–direction effects would be seen at the satellite scale. In flat terrain, corn rows are either planted strictly N–S or E–W (as near the REBEX–8 site). In other areas, rows are also sometimes planted in a contour fashion following the shape of gently rolling topography in order to reduce soil erosion. In areas where contour planting practices are not used, the rows in fields of size up to 1 km on a side will be either parallel or perpendicular to each other. When the canopy is senescent, variations in soil moisture, soil texture, vegetation, and row–effects will all contribute to the variability in brightness among fields within a single satellite pixel.

The zero–order radiative transfer model, valid for a weakly–scattering canopy, was able to reproduce the observed brightness temperature change with incidence angle in a mature field corn canopy only when the volume scattering coefficient, κ_s, was allowed to be non–zero and to change with incidence angle. Significant scatter darkening was observed and this darkening increased with incidence angle. The effect of volume scattering on absolute brightness temperature was greater at V–pol, but κ_s was unexpectedly found to be greater at H–pol. The consequence of not accounting for scatter darkening is a wet bias in soil moisture retrievals at incidence angles away from nadir.

Leaves were found to play an important role in both scattering and absorption. Before they lose their water when the canopy senesces, the leaves effectively "hide" the internal structure of the canopy. Scattering by the leaves was found to be much higher at H–pol than expected. At senescence, the canopy appeared to be more transparent at H–pol than predicted by the zero–order model. V–pol predictions at senescence were close to the observations.

What are the immediate consequences of these findings? First, if such a drastic change is seen in the brightness temperature of field corn as a result of senescence, are there other biophysical processes that could produce similar results? What impacts will changes in the distribution of water among the leaves, stems, and ears within the vegetation canopy, in response to other forcings such as periods of extreme drought or wetness, have on the brightness temperature?

The existence of significant volume scattering in heterogeneous canopies such as field corn may be the most important consideration. Volumetric soil moisture error at H–pol will be low during most of the summer months. On the other hand, volume scattering in the vegetation had a much larger effect on V–pol brightness temperatures, especially at high incidence angles. Although H–pol has traditionally been used to measure soil moisture, future satellite systems will measure brightness temperature at both polarizations and a large variety of incidence angles (typically from $\theta = 0°$ to $55°$) in order to improve ground resolution and to separate soil and vegetation contributions [*Kerr et al.*, 2001]. Detailed models that fully account for scattering have been recently developed [*Karam*, 1997], but the zero–order solution is still being used by most researchers in both experimental [*Crosson et al.*, 2002] and modeling studies [*Burke et al.*, 2002]. It has many advantages: simplicity; a long history of use in many types of vegetation canopies; potentially only a small set of required ancillary data (soil temperature, canopy temperature, and water column density), some of which could be retrieved by another remote sensing methods [*Jackson*, 1993]; and extensive validation. Unfortunately, most of the validation has been done at incidence angles near nadir where the effects of the canopy, and volume scattering, are small. The inability of the zero–order model to reproduce observed change in microwave brightness with incidence angle will be less drastic in many types of vegetation, and can be rectified by considering κ_s to be non–zero and a function of θ as shown is the present work, and in others at higher frequencies [*Brunfeldt and Ulaby*, 1986]. Further evaluation of the performance of the zero–order model at higher incidence angles must be performed.

CHAPTER 4

Radiometric Sensitivity to Soil Moisture, Vegetation Temperature, and Canopy Water in Scattering and Nonscattering Canopies at 1.4 GHz

Chapter 4 tests the zero–order model formulated in Chapter 3 against continuous observations of microwave brightness collected during REBEX–8x3 for a mature field corn canopy. The strengths and weaknesses of the model are identified. The weaknesses of the model are further investigated through careful analysis of recorded microwave brightness and coincident soil moisture and micrometeorology measurements. The sensitivity to soil moisture and to changes in canopy water, either in the form of intercepted precipitation or dew, are inferred from the data. Finally, this chapter compares the sensitivity of a the field corn canopy to changes in soil moisture, canopy water, and vegetation temperature to those sensitivities in a equivalent nonscattering canopy and to those predicted by the new zero–order model.

In this chapter, soil moisture is given in units of % instead of m^3 m^{-3} in order to be consistent with the microwave remote sensing literature.

4.1 Model Performance During REBEX–8x3

The zero–order model (3.2) was shown in Chapter 3 to match observations of brightness temperature during REBEX–8x3 if the volume scattering coefficient, κ_s, is allowed to be a function of incidence angle, i.e. the canopy is anisotropic in elevation. The data used

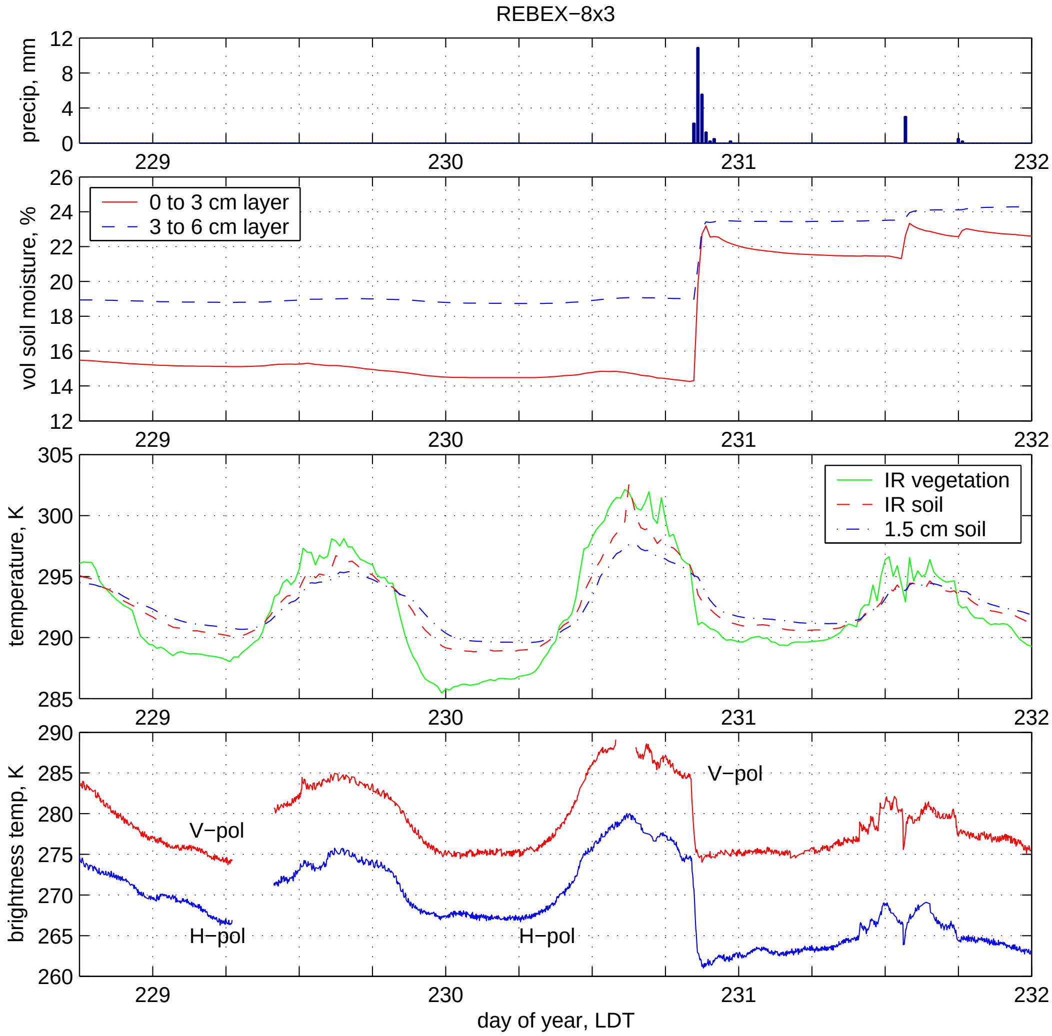

Figure 4.1: Precipitation, soil moisture, vegetation and soil temperatures, and 1.4 GHz brightness temperature ($\theta = 35°$, $\phi = 60°$) during REBEX–8x3.

to formulate the model were recorded near sunrise when temperature gradients within and between the soil and canopy were small (Table 3.2). How well does this model perform at other points during the day?

Figure 4.1 presents the precipitation, soil moisture, vegetation and soil temperatures, and microwave brightness recorded during REBEX–8x3. The radiometer's angle of incidence was 35°, at 60° with respect to row direction. The corn was mature and the water column density was at the highest level observed during the summer ($M_w = 6.3$ kg m^{-2}, $M = 8.0$ kg m^{-2}). Measurements of soil moisture and micrometeorology were 20–minute averages of data sampled every 10 seconds. Instantaneous measurements of brightness temperature were made every two minutes. Radiometer precision (NEΔT) was 0.4 to 0.5 K. Three rain events were recorded during the three day experiment: approximately 21 mm of rain fell between 20:00 and 23:40 on day 230; 3 mm between 13:20 and 13:40 on day 231; and less than 1 mm between 17:40 and 18:20 on day 231.

Upon initial examination of the data, the following observations can be made. Both polarizations tracked each other throughout the experiment and followed general trends in canopy temperature. The range of temperatures within the canopy is delimited by the measured vegetation and soil IR radiometric temperatures. There were several instances where sharp but short peaks in microwave brightness are related to peaks in vegetation IR radiometric temperature. V–pol microwave brightness had a slightly larger diurnal variation than H–pol. Before the first rain event late on day 230, the difference between V–pol and H–pol was approximately 7 to 8 K during the early morning hours (from 0:00 to 6:00), but 9 to 11 K during the afternoon (12:00 to 18:00).

The change in surface soil moisture following the 21 mm rain event on day 230 was smaller than expected. The equivalent depth of water stored in the soil, d, can be found from the volumetric soil moisture content:

$$\theta_v = \frac{d}{D} \times 100\%. \tag{4.1}$$

Here: θ_v is volumetric water content in %; and D is the total depth of soil solids, water, and air (the depth over which soil moisture is measured) [*Hanks*, 1992]. The 0–6 cm soil moisture increased by a little less than 7% after the rain, an increase in water equivalent depth of 4 mm. Since run–off was negligible at the experiment site, the balance of the precipitation, 17 mm, was either deposited on the vegetation or in deeper soil layers. Intercepted precipitation, at most equal (but likely less than) a heavy dew, would be less than 0.5 mm [*Jackson and Moy*, 1999]. Precipitation and 0–3 cm soil moisture during the time period leading up to REBEX–8x3 are plotted in Figure 4.2. After 22 mm of precipitation on day 210, less than 11 mm of rain fell over the next 20 days. This extremely dry period occurred during

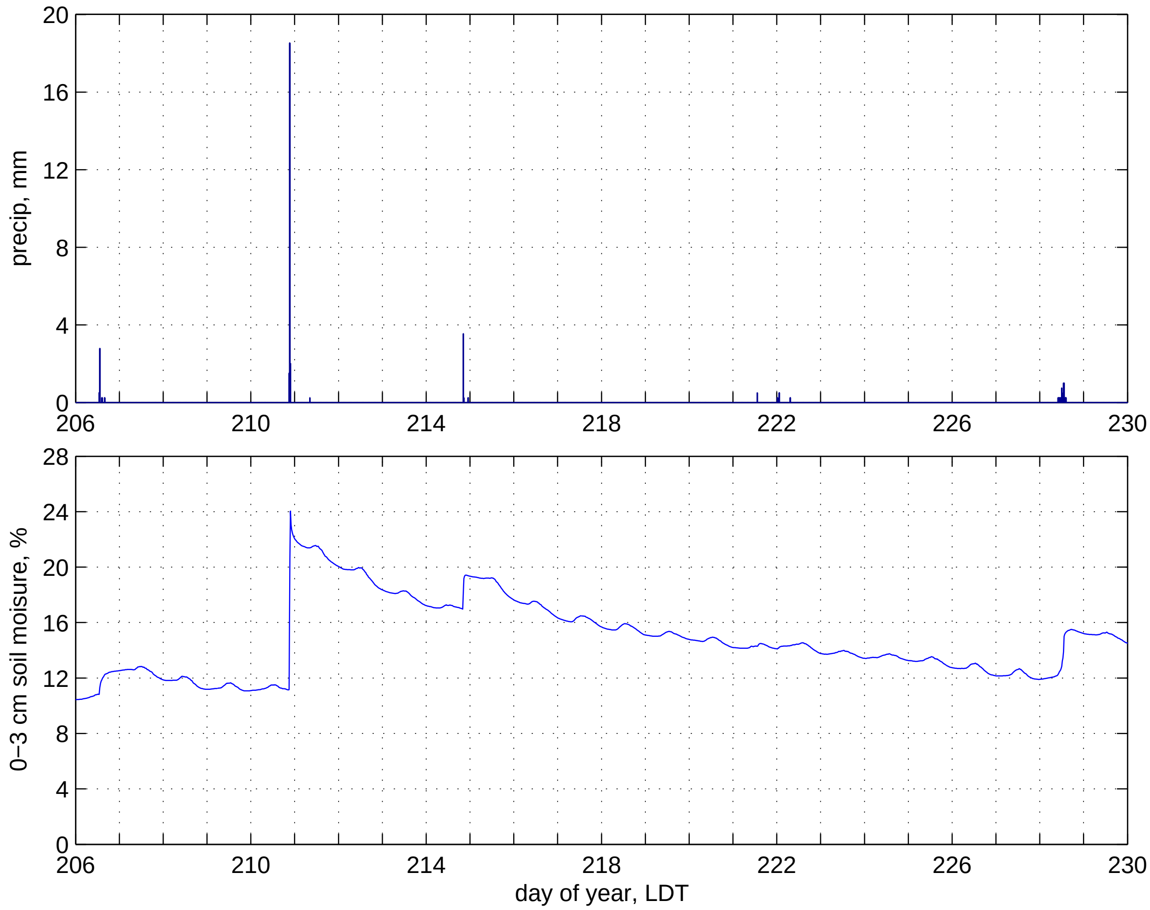

Figure 4.2: Precipitation and soil moisture leading up to REBEX–8x3.

the warmest point of the summer (late July and early August) and was reflected in the soil moisture record. It is plausible that cracks in soil formed during this dry period. Cracks would allow water to immediately penetrate to deeper depths within the soil. This would account for the “disappearance” of more than 16 mm of water on day 230.

In Figures 4.1 and 4.2 it is also apparent that the diurnal change in soil moisture is not quite correct. In the absence of precipitation, soil water content changes in response to temperature gradients. Water moves “down” a temperature gradient, from warmer regions to cooler regions. Hence soil moisture at the surface should peak shortly after sunrise when the soil at the surface is cooler than the soil at depth, decrease during the day as surface soil layer becomes warmer than the underlying soil, and increase again during the night. In Section 2.3, TDR temperature dependence was assumed to be negligible.

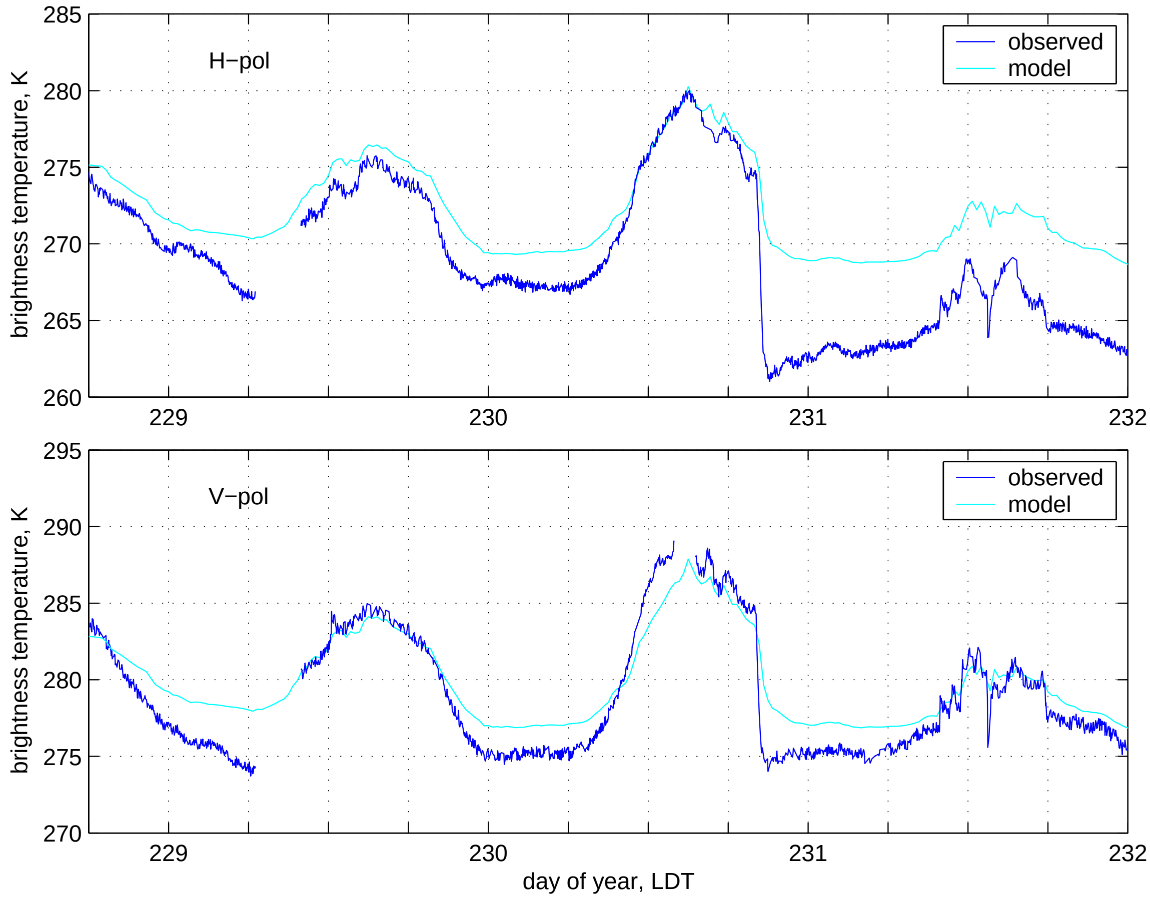

Figure 4.3: Observed and modeled H– and V–pol brightness temperatures during REBEX–8x3.

From Figure 4.2, it appears that in fact the temperature dependence is slightly positive: the increase in temperature during the day produces an apparent increase in the measured water content. A soil model in combination with the calibration procedure described in Section 2.3 could be used to find the true TDR temperature dependence for the soil at the experiment site.

Figure 4.3 compares observed and modeled H– and V–pol brightness temperatures during REBEX–8x3. The new zero–order model matches the observations closely. The model correctly predicts the change in brightness as the soil and canopy warm and cool over the course of the day. This performance is particularly striking considering the simplicity of the model. The variable T_{canopy}, defined as the average soil surface and vegetation IR radiometric temperature, appears to capture the essential variation in vegetation temperature. Temperature gradients within the canopy apparently have little affect on the microwave brightness, although these gradients were not large during REBEX–8x3 (at most 4 K).

The radiometric sensitivity to T_{canopy} can be found by taking the derivative of (3.2):

$$dT_B/dT_{canopy} = (1-\alpha)(1-L)\left[1+R_{soil}\,L\right]. \tag{4.2}$$

Recall that in the new model α and L, as well as R_{soil}, are functions of θ and polarization. R_{soil} is also a function of soil moisture (and weakly of soil temperature). Using (4.2), the sensitivity to canopy temperature can be found to vary only from about 0.64 to slightly less than 0.66 K K^{-1} at H–pol for volumetric soil moisture ranging from 15 to 25% (the range encountered during REBEX–8x3), and from about 0.63 to slightly more than 0.64 K K^{-1} at V–pol.

One strength of the model appears to be its sensitivity to canopy temperature. On the other hand, there are three periods during which the model significantly deviates from the observations. The first two periods occur during the night, on days 228/229 and 229/230. After each of these two periods, the model "recovers" and predictions match observations after about 10:00 in the morning. Could the presence of dew on the canopy, which would have formed overnight and then evaporated after sunrise, have caused these errors? The third period began late on day 230 and persisted until approximately 10:00 on day 231 at V–pol, and throughout all of day 231 at H–pol. The start of this period coincides with the first precipitation event which produced a change in 0–3 cm soil moisture of 9% and certainly would have thoroughly wet the canopy.

Evidently, one model weakness is its incorrect representation of the effects of water on the canopy. In all three periods, observed brightness is *less* than modeled brightness. One hypothesis that can be formed from these observations is that water on the canopy appears to *decrease* the microwave brightness. This hypothesis will be tested in Sections 4.3 and 4.4. The decrease in brightness during the third period could also have been caused by the change in soil moisture. To separate these effects, the sensitivity of microwave brightness to changes in soil moisture in this particular field corn canopy must first be determined.

4.2 Soil Moisture Sensitivity

It is generally assumed that microwave brightness at 1.4 GHz is sensitive to soil moisture up to a certain level of canopy biomass. This level has not been clearly defined. *O'Neill et al.* [1996] reported a measurable sensitivity to soil moisture at a water column density of 4 kg m^{-2}. *Ulaby et al.* [1983] found that a change of one percent gravimetric soil moisture produced a change in brightness temperature of 1.1 K for a water column density of approximately 5 kg m^{-2}. On the other hand, *Brunfeldt and Ulaby* [1984] observed no difference between corn fields that either had metal screens placed at the soil surface, or had no screens, at the middle of the growing season. Finally, *Wang et al.* [1984] observed no sensitivity to soil moisture through a grass canopy with vegetation column density of 8 kg m^{-2}. The point at which most vegetation canopies become opaque is believed by many researchers to be at a water column density of about 5 kg m^{-2}, but this must depend upon the distribution of moisture in the canopy. For example, while *Wang et al.* [1984] observed no sensitivity to soil moisture through a sufficiently dense grass canopy, a field corn canopy of similar density but with water concentrated in stems and ears might be sufficiently transparent to 1.4 GHz radiation to allow sensitivity to soil moisture.

The rain event on day 230 increased the 0–3 cm soil moisture by 9%. V–pol and H–pol brightness reacted differently to this change in soil moisture. See Figure 4.4 for a closer view of days 230 and 231. Immediately following the rain event there was a small increase in the H–pol brightness temperature, from 262.0 K at 22:00 on day 230 to 263.5 K at 6:00 on day 231. In this and the following analysis, several adjacent measurements of brightness temperature have been averaged together in order to lower the uncertainty to less than 0.2 K. This increase occurred while the 0–3 cm soil water content decreased by 1% as water infiltrated into the soil. On the other hand, the V–pol brightness temperature remained essentially constant during this same time period. This increase in H–pol

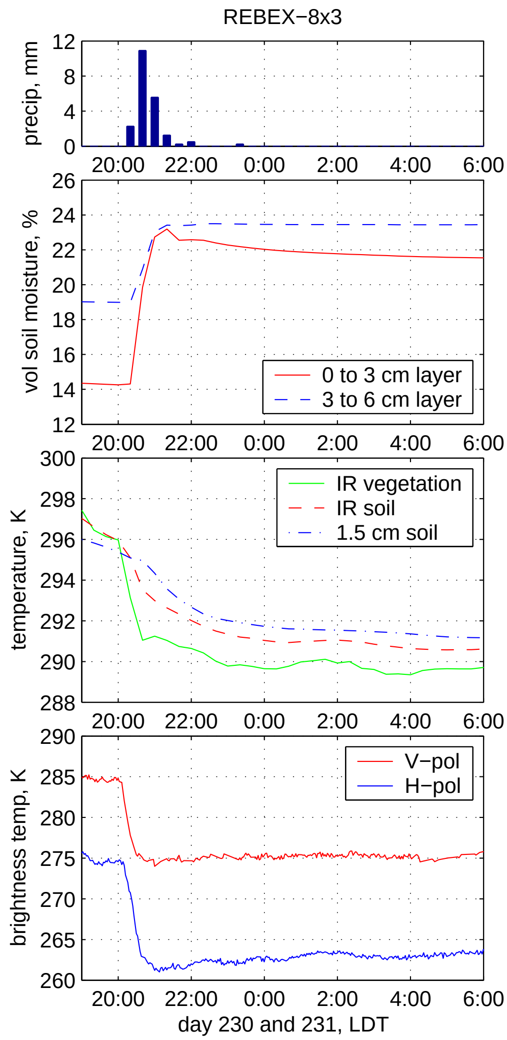

Figure 4.4: Soil moisture at 0–3 cm and the difference between V–pol and H–pol brightness temperatures during REBEX–8x3.

brightness temperature was not consistent with changes in vegetation or soil temperatures observed during the same period. T_{canopy} and soil temperature at 1.5 cm both *decreased* by 1.2 K and 1.4 K, respectively. It was also not likely to be caused by changes in water intercepted by the canopy, which would be expected to remain constant during the night. The change in H–pol brightness temperature appeared to be caused in large by the change in soil moisture. The sensitivity at H–pol was approximately:

$$\frac{\Delta T_B}{\Delta \mathrm{VSM}} \approx \frac{1.5\ \mathrm{K}}{1\%} = 1.5\ \mathrm{K}\ \%^{-1}. \tag{4.3}$$

This may be a conservative estimate, given the changes in soil and canopy temperatures

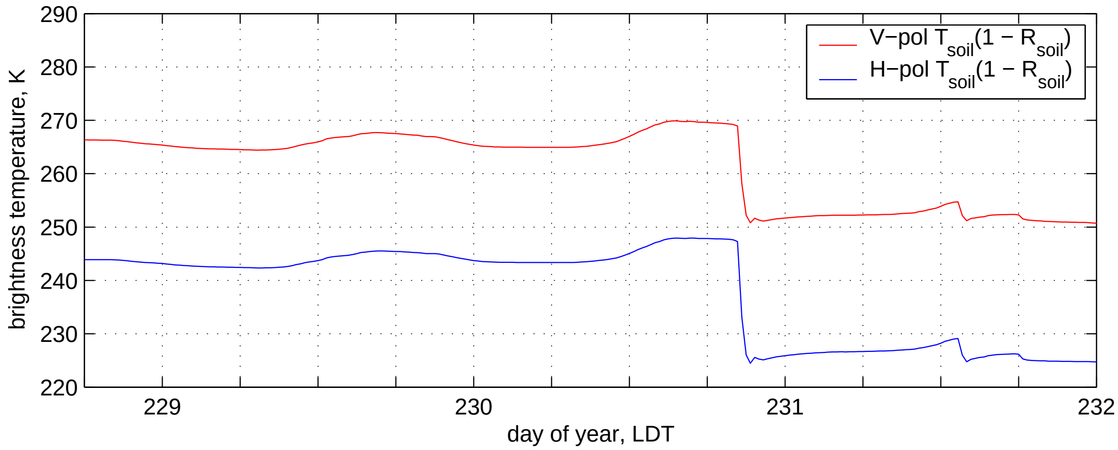

Figure 4.5: Modeled brightness temperature of the soil, just below the vegetation canopy, during REBEX–8x3.

which tended to decrease the brightness temperature during this time period. Taking into account the competing effects of changes in soil and canopy temperatures, V–pol sensitivity exists at this level of water column density, but it is much smaller ($<$ 1K), perhaps approximately equal to the sensitivity to canopy temperature.

The modeled brightness temperature of the soil, just below the vegetation canopy is plotted in Figure 4.5. The change in soil moisture produces about a 23 K and 10 K change at H– and V–pol, respectively. This sensitivity, about 2.6 K $\%^{-1}$ at H–pol, is consistent with past research [*Schmugge et al.*, 1986].

The 0–3 cm soil water content and the difference between V–pol and H–pol during REBEX–8x3 is shown in Figure 4.6. If in fact there was a much higher sensitivity to soil moisture at H–pol than at V–pol, there should be an obvious change in the difference between the polarizations after the rain event. This is what was observed. Before the first rain event, differences between V–pol and H–pol during the early morning hours (0:00 to 6:00) on days 229 and 230 were 7 to 8 K. After the rain event, H–pol was approximately 12 to 13 K lower than V–pol. During the rest of day 231, the difference between V–pol and H–pol was larger than it was when the soil was drier on days 229 and 230.

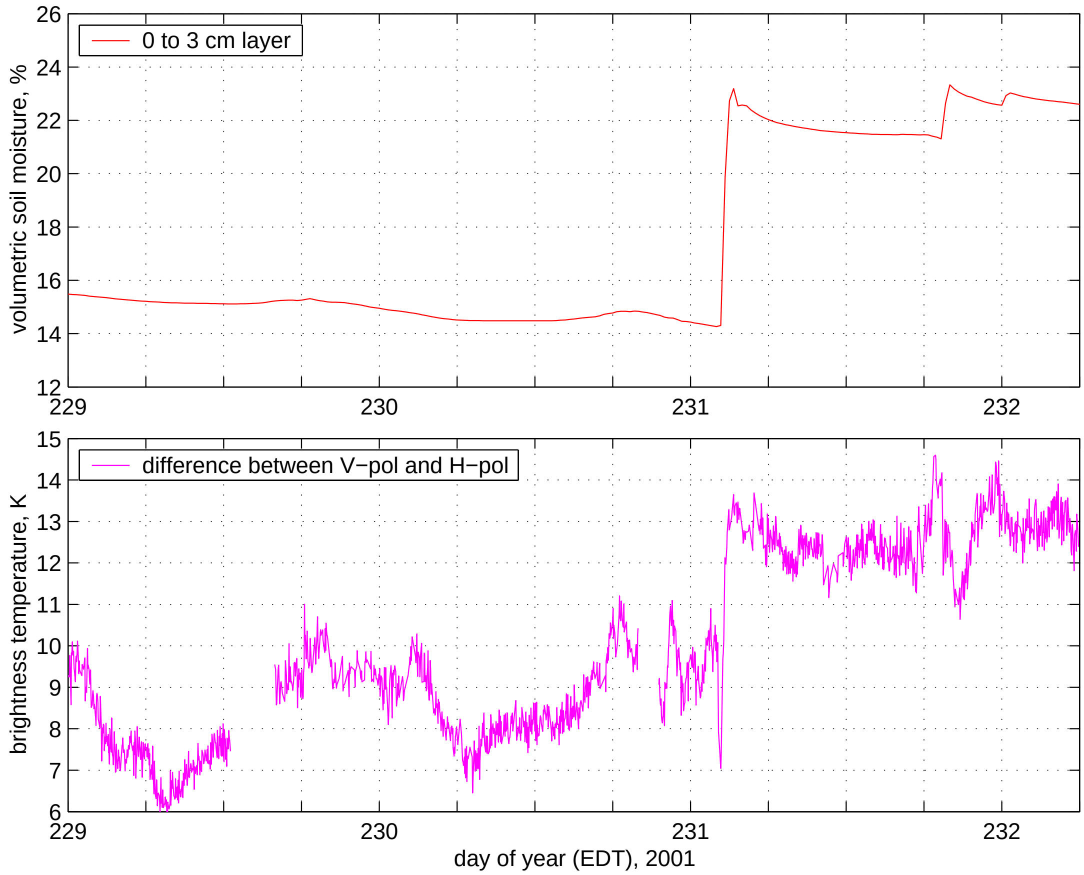

Figure 4.6: Soil moisture at 0–3 cm and the difference between V–pol and H–pol brightness temperatures during REBEX–8x3.

4.3 Dew

Does dew on the canopy affect the brightness temperature? Theoretically, liquid water on the scatterers in the canopy would increase their dielectric constant and loss. Higher scatterer dielectric constant results in more scattering of radiation out of the beam. When the scatterers have a higher loss, more of the scattered radiation is absorbed by other scatterers and hence less radiation can be scattered *back* into the beam. The result is an increase in volume scattering and lower brightness temperatures. But this may be balanced or exceeded by an increase in emission due to an increase in the total water column density [*Ferrazzoli et al.*, 1992]. What is the net effect of water on the canopy?

A light dew was observed during data collection around 7:00 LDT on day 229. The dew had evaporated by 10:00 that morning. The comparison of model predictions and observed brightness temperatures in Figure 4.3 during this period suggest that the net effect of dew is a decrease in the microwave brightness. No visits to the experiment site were made on days 230 and 231, although the model predictions again indicate the likely presence of dew during the night of days 229/230.

In order to determine the relative amount of dew during the night and early morning hours of days 228/229 and 229/230, the canopy energy balance was evaluated to find the latent heat transfer [*Arya*, 1988]:

$$H_L = R_n - H_S - G - \Delta W. \tag{4.4}$$

Here H_L is the flux of latent heat; R_n, the net radiation; H_S, the sensible heat flux; G, the ground heat flux; and ΔW, the rate of change of energy stored in the canopy. All of these variables have the units of W m^{-2}. The net radiation was not measured directly. It was calculated using measurements of downwelling solar radiation, S, downwelling atmospheric radiation, A, and vegetation IR radiometric temperature, T_{veg}:

$$R_n = S + A - \left(aS + \sigma T_{veg}^4\right) \tag{4.5}$$

where σ is the Stefan–Boltzmann constant and a is the albedo [*Jacobs and Van Pul*, 1990]. The vegetation radiometric temperature, instead of the canopy temperature, was used since it is a direct measurement of the emission from the top of the canopy and a canopy emissivity of unity at IR wavelengths has been assumed. The sensible heat flux was calculated using bulk aerodynamic theory as follows:

$$H_S = \rho_{air}\, c_{p,air}\, C_H \left(T_{veg} - T_{air}\right) u \tag{4.6}$$

where ρ_{air}, is the density of air; $c_{p,air}$, air specific heat;

$$C_H = k^2 \left[\ln\left(\frac{z_u - d}{z_{om}}\right) + \psi_m(\zeta)\right]^{-1} \left[\ln\left(\frac{z_a - d}{z_{oh}}\right) + \psi_h(\zeta)\right]^{-1}, \tag{4.7}$$

the transfer coefficient; T_{air}, the air temperature measured at z_{air}; u, the wind speed at z_u; k is Von Karman constant; d, the zero–plane displacement [*Jacobs and Van Boxel*, 1988];

z_{om}, the roughness length for momentum [*Jacobs and Van Boxel*, 1988]; z_{oh}, the roughness length for heat; ψ_m and ψ_h are the profile diabatic correction factors for momentum and heat, respectively; and ζ, the buoyancy parameter. $\ln(z_{om}/z_{oh}) \approx 2$ [*Massman*, 1999]. For stable conditions typical at night, $\psi_m = \psi_h = 6\ln(1+\zeta)$ [*Yasuda*, 1988] and $\zeta \approx 0.4$ [*Wilson et al.*, 1999]. Again, vegetation radiometric temperature, instead of canopy temperature, was used since it is the top of the canopy that is exchanging heat with the atmosphere. The rate of change of energy stored in the canopy was estimated using the canopy water column density:

$$\Delta W \approx \frac{M_w\, c_{p,water}\, \Delta T_{canopy}}{\Delta t}. \tag{4.8}$$

$c_{p,water}$ is the specific heat of water; T_{canopy}, the average of measured vegetation and soil IR temperatures; and ΔT_{canopy}, the change in T_{canopy} during the measurement time interval Δt. Ground heat flux was *not* measured, but estimated to be -15 W m^{-2} based upon measurements made under a field corn canopy during REBEX–7 the previous summer.

Dew is the result of three processes [*Monteith*, 1957]. Dewfall, or water condensing from air originating above the canopy, is by far the dominant process of dew formation in a corn canopy when the soil surface is dry [*Atzema et al.*, 1990]. Recall from (1.3) that latent heat flux is equal to the rate of evaporation, transpiration, and condensation, E, multiplied by the latent heat of vaporization, L_e:

$$H_L = L_e E. \tag{4.9}$$

At night, transpiration is negligible and a negative latent heat flux represents condensation of water on the canopy. Figure 4.7 presents the canopy temperature, the cumulative amount of condensation (dew) on the canopy since 18:00 LDT as predicted by (4.4), and the H– and V–pol brightness temperatures for the night of days 228/229 and 229/230.

A negligible amount of dew on 229/230 is predicted by the energy balance model. This is contrary to the predictions of the zero–order model in Figure 4.3. If the net effect of dew is a decrease in brightness, smaller yet significant amount of dew should have

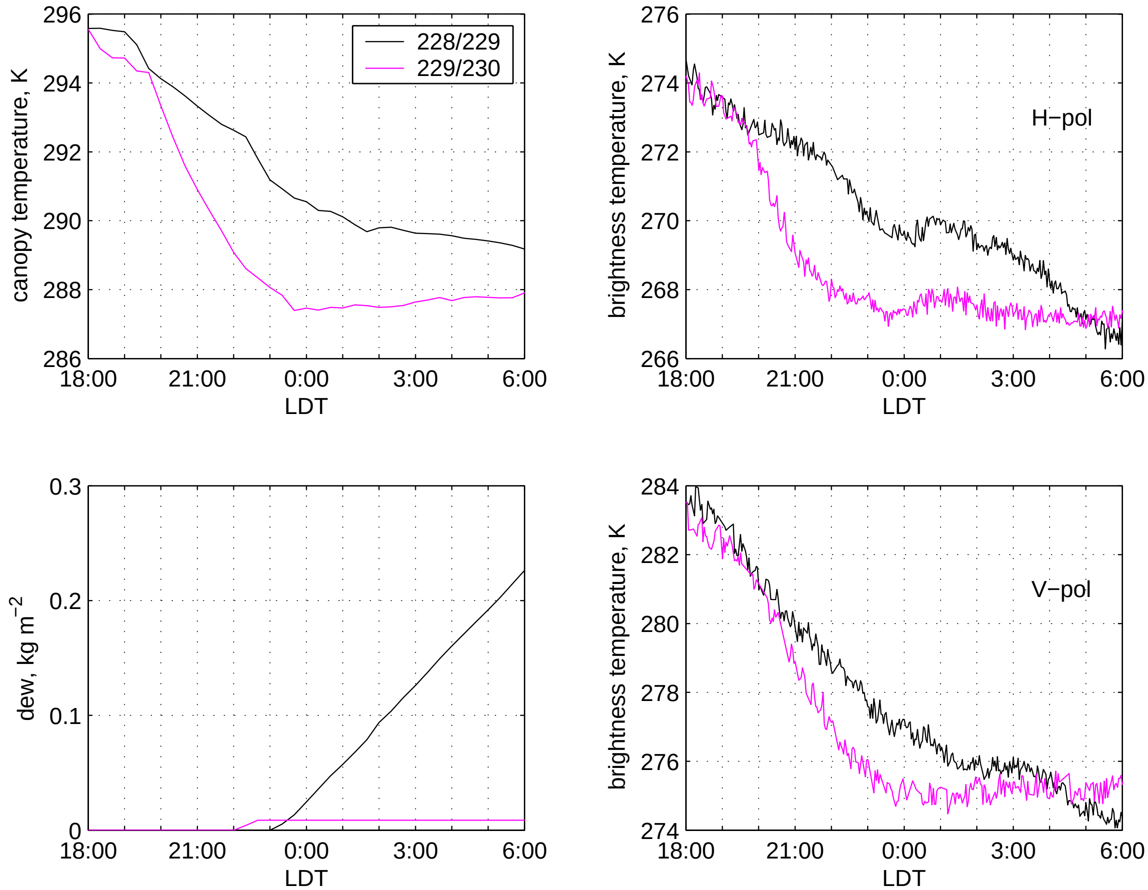

Figure 4.7: Canopy temperature, modeled dew deposition to the canopy, and H– and V–pol brightness temperatures during the night for days 228/229 and 229/230.

covered the vegetation on 229/230. Predictions of the zero–order model are depressed by approximately 4 K at both H– and V–pol on day 228/229 and by approximately 2 to 2.5 K on 229/230. Although the energy balance method is physically correct, the theory employed to compute the components of the energy balance are simplifications of complex processes. The bulk aerodynamic transfer coefficient in (4.7) rests on many assumptions and is suitable only for mean behavior. Furthermore, both changes in canopy energy storage and ground heat flux were estimated. Even though ground heat flux was measured in a similar situation, ground heat flux is difficult to measure [*van Loon et al.*, 1998]. Errors in any of the terms on the right–hand side of (4.4) would alter the *amount* of dew on the canopy.

Although the total amount of dew predicted by the model in Figure 4.7 is reasonable, it is probably incorrect. There is more confidence in the predictions of the *relative* amount of dew deposited during the nights of 228/229 and 229/230. Uncertainty in the variables of (4.4) are likely to be similar on consecutive nights. Taking the limitations of this modeling approach into account, Figure 4.7 would at least indicate that *less* dew formed on the canopy during the night of days 229/230 than on 228/229. If this is correct, then it appears that: the net effect of dew is a decrease in brightness; and as more dew is deposited on the canopy, the brightness continues to decrease.

From the zero–model comparison in Figure 4.3, it appears that the brightness temperatures on the night of days 228/229 were progressively depressed as the dew formed, while on the night of 229/230, dewfall occurred earlier, during a short period of time, and remained on the canopy for the rest of the night. The gradual increase in the difference between modeled and observed brightness on 228/229 in Figure 4.3 also supports the conclusions made earlier.

According to Figure 4.7, by the approximately 6:00 LDT on day 229, brightness temperatures at both H– and V–pol were approximately 1 K lower than the brightness temperatures recorded the next night, despite the fact that the canopy temperature at 6:00 on day 229 was more than 1 K *higher* than on day 230. Soil moisture was virtually constant during this time and soil temperature at 1.5 cm was 2 to 3 K *less* on the night of 229/230 (Figure 4.1). If there was in fact dew on the canopy on the night of 229/230, then these observations again support the assertion that *more* dew the previous night resulted in a *larger* decrease in the brightness temperature. It also appears that dew effects H– and V–pol brightness equally.

The assertion that there was more dew on the canopy during the night of 228/229 than 229/230 is supported by measurements of air temperature, dew point temperature, and wind speed in Figure 4.8. Dew point temperature was calculated from the air temperature and relative humidity measured at 7.8 m. Wind speed was measured at 10 m. Note that at

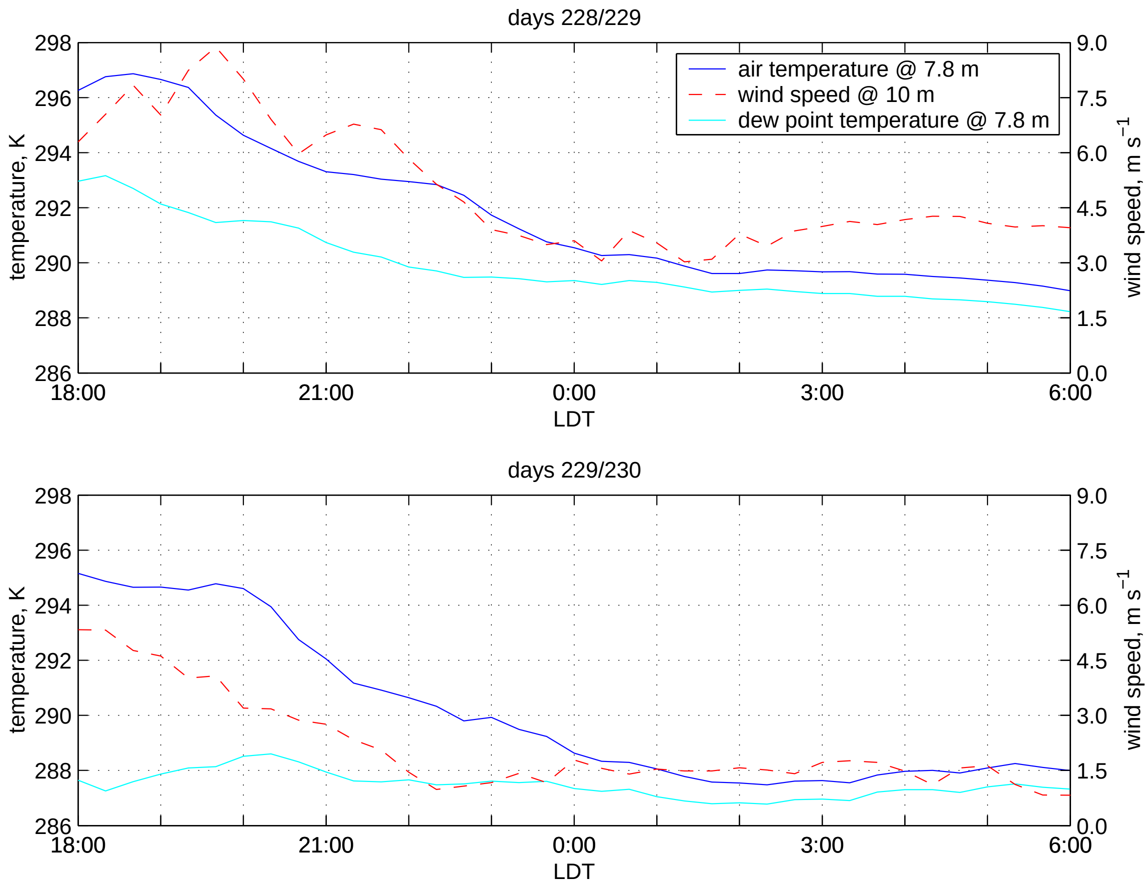

Figure 4.8: Air temperature at 7.8 m, wind speed at 10 m, and dew point temperature at 7.8 m for the night of days 228/229 (top) and the night of days 229/230 (bottom).

18:00 the dew point temperature on 228/229 was much higher than on 229/230, indicating that there was *less* moisture in the air above the canopy on the second night. On the night of 228/229, the dew point temperature immediately began to decrease, suggesting either condensation on the canopy was pulling moisture from the air, or the arrival of a drier air mass. On the other hand, the dew point temperature on 229/230 remained roughly constant the entire night. From 0:00 on, air and dew point temperatures were nearly identical on both nights.

Another notable feature of Figure 4.8 is the difference in measured wind speed between the two nights. The wind speed is considerably lower on 229/230. (The threshold of the anemometer was 0.45 m s^{-1}). According to bulk aerodynamic theory,

$$E = \rho_{air} C_W \left(Q_0 - Q\right) u \tag{4.10}$$

where: C_W is the transfer coefficient for water vapor, similar to the transfer coefficient for heat in (4.7); Q_0 is the mean specific humidity close to the surface; and Q is the mean specific humidity at a reference height. During dew formation, $Q_0 < Q$ (the surface is drawing moisture from the air above) and $E < 0$. Note that E is also directly proportional to wind speed. Given the limitations of the bulk aerodynamic approach discussed earlier, a higher wind speed on the night of 228/229 than on 229/230 would favor more dew. There is a point at which a higher wind speed inhibits dew formation [*Monteith*, 1957], but the wind on 228/229 was fairly gentle and likely below this level.

In summary, observations and modeling results support the hypothesis that water on the canopy in the form of dew has the net effect of *decreasing* the microwave brightness. Furthermore, it appears that as more water is deposited on the canopy, the microwave brightness continues to decrease. Both polarizations appear to be affected equally.

4.4 Intercepted Precipitation

The data from REBEX–8x3 in Figure 4.1 and Figure 4.4 show that H–pol and V–pol both experienced sharps drops during each rain event. On day 230, the H–pol brightness temperature decreased by 13.4 K between 20:00 and 21:20 LDT, while V–pol decreased by 10.8 K. During this same time period, the canopy temperature decreased by 4.1 K and 20 mm of precipitation fell, causing the 0–3 cm soil moisture to increase by 9%. Considering the analyses in Sections 4.2 and 4.3, the change in brightness on day 230 must be a combination of changes in canopy temperature, soil moisture, and water on the canopy.

Given the sensitivity to soil moisture at H–pol in (4.3), a 9% change in soil moisture would result in a $9\% \times 1.5\ \mathrm{K}\ \%^{-1} = 13.5$ K change in brightness temperature. This is slightly more than the entire change observed at H–pol. According to (4.2), the change in canopy temperature during this period would result in a $4.1\ \mathrm{K} \times 0.6\ \mathrm{K\ K}^{-1} = 2.5$ K change in brightness temperature. If instead a soil moisture sensitivity of approximately 1 K $\%^{-1}$ is assumed, then a $13.4 - 2.5 - 9 \approx 2$ K change could be attributed to the change in canopy water. At V–pol, the soil moisture sensitivity is much less. The change in vegetation temperature also accounts for $4.1\ \mathrm{K} \times 0.6\ \mathrm{K\ K}^{-1} = 2.5$ K of the 10.8 K total change in brightness temperature. The other 8.3 K must be a combination of enhanced scattering due to the canopy water and to the change in soil moisture. If a soil moisture sensitivity equivalent to the sensitivity to canopy temperature is assumed, then $9\% \times 0.6\ \mathrm{K}\ \%^{-1} = 5.4$ K can be attributed to the change in soil moisture and the rest, $10.8 - 2.5 - 5.4 \approx 3$ K due to the effect of the intercepted precipitation. From these approximate calculations it again appears that the net effect of intercepted precipitation is a decrease in brightness temperature at both H– and V–pol. Volume scattering is enhanced more than emission.

The model comparison in Figure 4.3 supports a 2 to 3 K decrease in V–pol brightness temperature due to the intercepted precipitation. By approximately 10:00 on day 231, the model predictions again match the observations. These observations are consistent with a drying of the canopy. On the other hand, modeled H–pol brightness remains higher than the observed brightness throughout the course of day 231. Evidently, the canopy is *more transparent* than predicted by the model: the soil moisture sensitivity predicted by the model is *too low*. It also appears that dew can wet the canopy more than intercepted precipitation. A maximum depression of about 4 K was observed during dew formation while the decrease in brightness was slightly less (about 2 to 3 K) after the 21 mm precipitation event.

There were two other rain events during REBEX–8x3. Within less than 20 minutes after the second rain event, both polarizations of microwave brightness recovered quickly and started to increase. It was unlikely that such a quick change in brightness temperature was related to canopy water, despite the fact that the zero–order model V–pol predictions support the existence of a dry canopy after about 10:00 on day 231. Either the microwave brightness was responding solely to changes in vegetation temperature, or perhaps the canopy was still wet from the first rain event and water ponded between the rows for a short period of time. Another sharp drop during the third rain event appears to be caused by intercepted water. The model does not predict all of the drop observed at both H– and V–pol and this drop remained through the end of the data record. It is not known for certain whether the canopy dried during the 4 hours after the second rain event.

4.5 Conclusions

The new zero–order model, which considers κ_s to be a function of θ, correctly predicts the change in brightness in response to changing vegetation temperature. In light of its simplicity, this performance was not expected and its sensitivity to vegetation temperature is the model's main strength.

The net effect of water on a field corn canopy, either in the form of dew or intercepted precipitation, is to decrease the brightness temperature. Volume scattering is enhanced more than emission. This effect is seen at both polarizations, and each polarization appears to be affected equally. As more water is deposited on the canopy the brightness at both polarizations continues to decrease. At some point a decrease in brightness with canopy water would no longer occur since there is a limit to the amount of water that a canopy can hold. Depressions of about 2 to 4 K were observed. Dew can decrease the brightness more than a soaking rain. The new zero–order model did not correctly predict this decrease in brightness. In fact, any increase in canopy water (water column density) *increases* the brightness predicted by the zero–order model. These predictions are *opposite* of what was observed in field corn. For other canopies, the balance between enhancement of volume scattering and emission may depend on the vegetation type and observation frequency [*Wigneron et al.*, 1996] and water on the canopy may significantly bias soil moisture retrievals in either direction.

Finally, a robust sensitivity to changes in soil moisture, approximately 1 to 1.5 K per % 0–3 cm volumetric water content, was observed at H–pol in field corn at a water col-

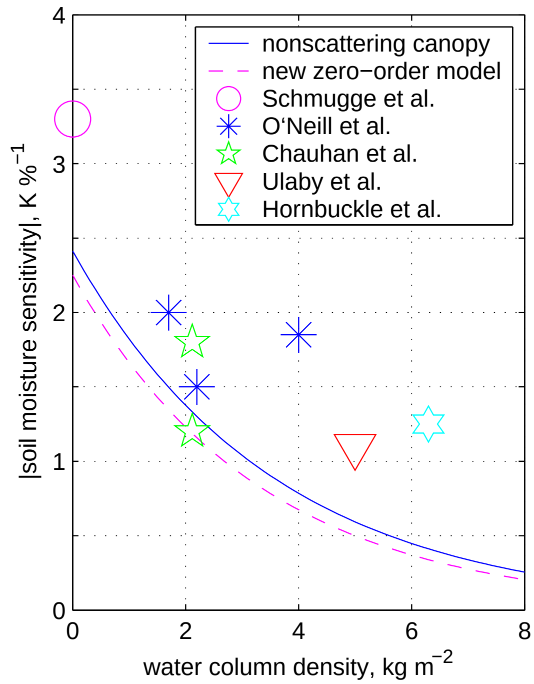

Figure 4.9: Modeled and measured sensitivity of H–pol 1.4 GHz brightness temperature to volumetric soil moisture in field corn.

umn density of 6.3 kg m^{-2}, the highest column density observed during the summer. The sensitivity at V–pol was less than 1 K and similar in magnitude to the sensitivity to vegetation temperature. Soil moisture sensitivity as predicted for a nonscattering canopy ($\tau = b \times M_w$, $b = 0.115$ [*Jackson and O'Neill*, 1990]), the new zero–order model, and the sensitivities reported in field corn from aircraft platforms [*Chauhan et al.*, 1994; *O'Neill et al.*, 1996; *Ulaby et al.*, 1983], a bare soil sensitivity established by many field experiments both from both airplane platforms and tower/truck–mounted radiometers [*Schmugge et al.*, 1986], and this dissertation for H–pol brightness temperature at 1.4 GHz is plotted in Figure 4.9. The soil moisture sensitivity reported in this dissertation is significantly higher than that predicted for an equivalent nonscattering canopy and by the new zero–order model.

It can be concluded that both the amount of water in the canopy (water column density), and its *distribution* play an important role in determining soil moisture sensitivity. Hence canopies such as field corn in which the moisture is concentrated in stems and fruit appear

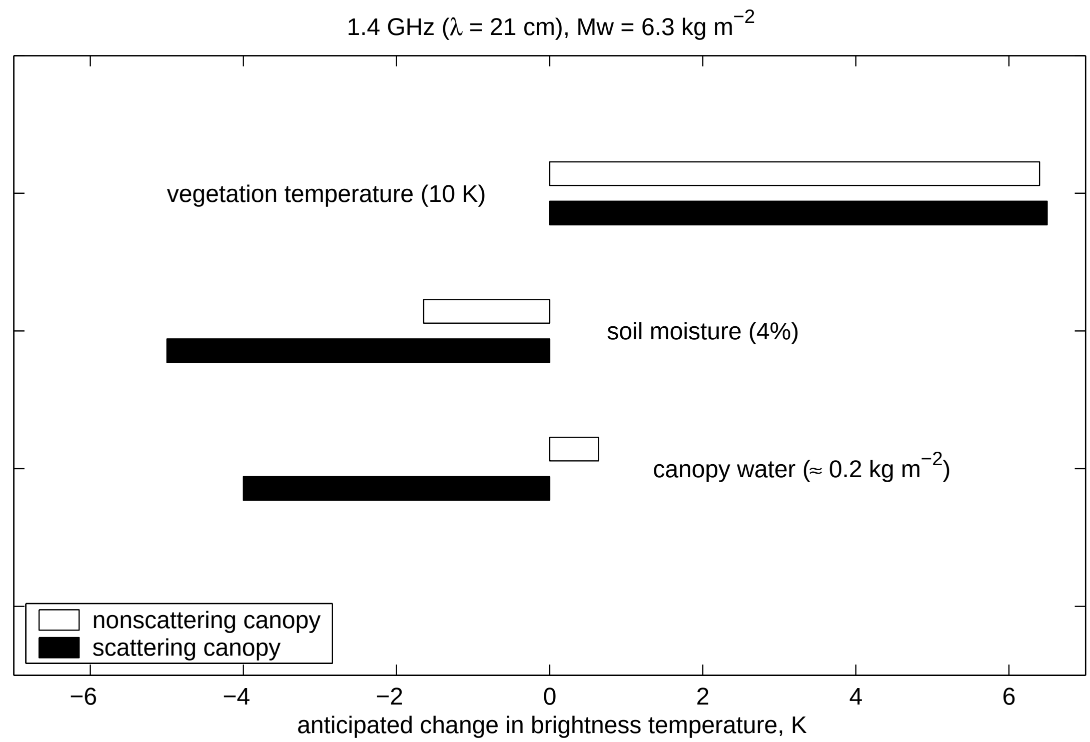

Figure 4.10: Anticipated change in H–pol brightness temperature in response to typical changes in vegetation temperature, soil moisture, and canopy water at 1.4 GHz for a real (scattering) mature field corn canopy and an equivalent nonscattering canopy

.

more transparent than nonscattering canopies such as grass where the water is more evenly spread over the entire canopy volume. The increased sensitivity to soil moisture could be because the canopy is in fact more transparent than predicted, or because the zero–order model does not account for reflections between the canopy and the soil surface. Enhanced backscatter from scattering canopies has been observed in radar experiments. There may be a similar effect in radiometry.

With an appropriate emission model that can account for both volume scattering and the effects of water on the canopy, microwave radiometry will be able to detect changes in soil moisture of less than 2%, given a typical microwave radiometer NEΔT of 1 K, at all stages of field corn development (growth, maturity, and senescence). The zero–order model is a strong candidate, if its two main weaknesses (sensitivity to canopy water and H–pol transparency) can be rectified.

The approximate radiometric sensitivities of a nonscattering canopy, the new zero–order model, and a scattering (field corn) canopy to vegetation temperature, soil moisture, and water column density are listed in Table 4.1. The anticipated change in brightness that can be expected given typical changes in vegetation temperature, soil moisture, and canopy water in scattering (field corn) and nonscattering (grass) canopies is shown in Figure 4.10. The amount of dew deposited during the night of 228/229 (roughly 0.2 kg $m^{-2} = 0.2$ mm) and the associated change in brightness (about 4 K) is assumed to be typical. Note that: the anticipated changes are comparable; the change in response to soil moisture is much greater in scattering canopies; and changes in canopy water have opposite effects. A heavy dew can deposit up to approximately 0.4 to 0.5 kg m^{-2} = 0.4 to 0.5 mm of water [*Atzema et al.*, 1990; *Jackson and Moy*, 1999]). Change in brightness caused by dew may be the biggest challenge to year–long sensitivity to soil moisture in field corn. The new zero–order model's sensitivity to temperature was excellent. On the other hand, the overpass time of future satellite missions are likely to be in the early morning hours when dew may be present.

Table 4.1: Radiometric sensitivity to: vegetation temperature (vt), in K K^{-1}; soil moisture (sm), in K $\%^{-1}$; and canopy water (cw), in K dg^{-1} m^{-2} (Kelvin per decigram per square meter), for nonscattering canopies, the new zero–order model, and an actual field corn canopy at 1.4 GHz and a water column density of 6.3 kg m^{-2}.

	vt (H,V)	sm (H)	sm (V)	cw (H)	cw (V)
nonscattering canopy	0.6	-0.4	-0.3	0.3	0.5
new zero–order model	0.6	-0.3	-0.3	0.4	0.7
field corn canopy	0.6	-1.3 K	-0.6	≈ -2	≈ -2

CHAPTER 5

Summary, Contributions, and Future Work

This final chapter includes a summary of the dissertation, identification of significant contributions, and recommended future work.

5.1 Summary

Many of the impacts of climate change will be expressed in the water cycle. Microwave radiometry is sensitive to the quantity and distribution of moisture in soil and vegetation. Recent advances in radiometer technology and data assimilation techniques offer the possibility of real–time soil moisture measurements on a global scale. Critical to this vision is the development of reliable models of land surface microwave brightness. In this dissertation, measurements of 1.4 GHz brightness, micrometeorology, and soil moisture were collected over the course of the growing season in a field of corn to determine how scattering canopies differ from the predictions made by models that are only strictly appropriate for weakly–scattering canopies. Of greatest interest was how the amount and distribution of moisture in vegetation influences microwave brightness.

5.2 Contributions

- Both polarizations of the 1.4 GHz brightness of a field corn canopy are isotropic in azimuth during most of the growing season. When the canopy is senescent, 1.4 GHz brightness is a strong function of row direction. At H–pol, brightness is highest parallel to the rows, while at V–pol, brightness is highest perpendicular to the rows. Brightness temperature changes by 5 to 10 K in azimuth, depending on the incidence angle. These findings greatly simplify the formulation of appropriate models of land surface brightness. Leaves were seen to play an important role: instead of acting simply as a "cloud" of moisture, they scatter microwave radiation and mask the internal, stem–dominated structure of a field corn canopy. At senescence when they lose their water, they become essentially invisible and the internal structure is exposed.

- The question is raised whether other biophysical processes, associated with periods of drought or extreme wetness, could cause changes in the effective canopy constitutive properties. In many areas, agricultural fields are strictly planted N–S or E–W, and azimuthal anisotropy at senescence will contribute to the inter–pixel variability of satellite measurements. Errors of 5 to 10 K may translate into errors of 10 to 20% in soil moisture estimation.

- The zero–order radiative transfer model, used by many researchers because of its simplicity, could not reproduce the observed change in brightness with incidence angle measured in a field corn canopy. Validation of this model by other researchers has occurred only at angles of incidence near nadir. The measurements reported in this dissertation represent the first reported systematic investigation of the variation with incidence angle. Significant scatter darkening was found. Without knowledge of the behavior of scatter darkening, soil moisture retrievals would have a wet bias, on the order of 2 to 12% at H–pol. These findings are timely since the first significant 1.4 GHz radiometer (SMOS) will be launched within the next few years. Initial versions of algorithms constructed for this mission will utilize V–pol brightness at large incidence angles to estimate biomass. Scatter darkening at V–pol was even greater than at H–pol. If this effect were ignored, vegetation column density would be underestimated, leading to over prediction of soil moisture.

- A new zero–order model was formulated to account for the observed variation with incidence angle. This was accomplished by allowing the volume scattering coefficient to be a function of incidence angle and polarization. The canopy medium is anisotropic in elevation. Potentially this model will be of great use for the SMOS mission. The small magnitude of the scattering coefficients allows the zero–order model to retain its limited physical significance. Surprisingly, scattering was more important at H–pol than V–pol, lending more information on the role of leaves.

- The new zero–order model was compared with continuous measurements of microwave brightness made in a field of mature corn. The new model correctly predicts change in brightness in response to vegetation temperature. The weakness of this and any other zero–order model is its under prediction of the H–pol soil moisture sensitivity in heterogeneous canopies where the moisture is concentrated in stems and fruit, and its inability to respond correctly to changes in canopy water, either in the form of intercepted precipitation or dew. Both the distribution and amount of water in the canopy were found to be important.

- Soil moisture sensitivity at H–pol was found to be at least 1 K $\%^{-1}$ in a mature field corn canopy. This sensitivity is much higher than expected, both from model predictions and the results of previous research. With an appropriate emission model, there will be significant soil moisture sensitivity throughout the growing season in most, and perhaps all, agricultural crops. There are no other published records of soil moisture sensitivity at such a high level of vegetation column density. Only the use of a unique technique, consisting of simultaneous analyses of continuous measurements of microwave brightness, micrometeorology, and soil moisture, allowed this observation of sensitivity to be made.

- An increase in canopy water, either in the form of intercepted precipitation or dew, has the net effect of decreasing the microwave brightness in a corn canopy. This effect was observed at both polarizations, and each polarization appeared to be affected equally. This is opposite to what had been assumed previously. This work also marks the first time the effects of dew on the brightness have been successfully identified. As more water is deposited on the canopy, the brightness at both polarizations continues to decrease. Depressions of 2 to 4 K were observed. Dew can decrease the brightness more than a soaking rain.

- The radiometric sensitivities to soil moisture, vegetation temperature, and canopy water for nonscattering and scattering canopies were found at a vegetation column density of 8 kg m^{-2}. The expected change in brightness is comparable for typical changes in these three variables. Accounting for the presence of dew and the corresponding decrease in brightness may be the biggest challenge to year–long sensitivity to soil moisture in agricultural crops.

- Precise and continuous measurements of brightness temperature, micrometeorology, and soil moisture were made on the plot scale. A unique measurement technique allowed the calibration of buried soil moisture sensors, This rare data set can be used in many more investigations.

5.3 Future Work

Hypothesis:

> Models of microwave brightness can be improved by taking into account the static and time–varying spatial distribution of water in and on the vegetation, along with canopy geometry.

I propose to develop a detailed soil–vegetation–atmosphere transfer (SVAT) model to couple with models of microwave emission in order to further improve brightness modeling by taking into account temperature variations and the time–varying spatial distribution of water in and on the vegetation. I plan to test these coupled models with data I have collected during my thesis work and in future plot–scale field experiments. Ultimately, these models will be used in conjunction with future satellite measurements to predict the moisture and energy exchange between the land surface and the atmosphere on regional scales.

Coupled SVAT and microwave brightness models allow the integration of many types of observations, both of microwave brightness and micrometeorology, over long periods of time. Through this integration, subtle physical properties can be uncovered. The power of this approach is illustrated in Chapters 3 and 4 of this dissertation. Without this time-series of microwave brightness, micrometeorology, and soil moisture data, I would not have been able to discover the relative influences of canopy anisotropy, vegetation temperature, soil moisture, and canopy water. This concept of using other data besides simply the microwave brightness over longer periods of time is much like using the context of a sentence to decipher an unknown word, as opposed to only examining the word itself. I would not have been able to draw these conclusions if only observations of microwave brightness had been made, or if the observations had been too sparse (e.g. once daily measurements as typically recorded in other investigations). I suspect much more information can be extracted from this existing data set using coupled SVAT and microwave brightness models.

Although developing and validating a new SVAT model will be challenging, it may in itself not be an entirely new research activity. It will, however, enable me to later pursue original research on how time-varying spatial distributions of water in and on the vegetation canopy can effect the microwave brightness and its sensitivity to soil moisture. Together, the new coupled SVAT and microwave models would enable me to improve the fundamental physics of microwave scattering models and ultimately to confront other central scientific issues, such as understanding the roles of land surface energy and water exchanges and their correct scale of representation in models [*National Research Council*, 1999] in anticipation of the first significant 1.4 GHz satellite radiometer, scheduled for launch in 2005 [*Kerr et al.*, 2001]. My other future research goals include:

- further development of in situ soil moisture measurement expertise with single frequency (impedance probes) and multi–frequency (time domain reflectometry) instruments;
- development of new single frequency and multi–frequency instruments to measure the time–varying distribution of water in vegetation;
- development of SVAT / microwave brightness models for several types of vegetation;
- determining the scales at which SVAT / microwave brightness models correctly anticipate soil moisture, brightness, and surface fluxes;
- extending point–scale (one-dimensional) SVAT / microwave brightness models to two and three dimensions;
- and incorporating SVAT / microwave brightness models into numerical weather prediction models.

BIBLIOGRAPHY

BIBLIOGRAPHY

Anderson, J., H. van den Dool, A. Barnston, W. Chen, W. Stern, and J. Ploshay, Present–day capabilities of numerical and statistical models for atmospheric extratropical seasonal simulation and prediction, *Bull. Amer. Meteor. Soc.*, *80*, 1349–1361, 1999.

Arya, S. P., *Introduction to Micrometeorology*, Academic Press, San Diego, CA, 1988.

Atzema, A. J., A. F. G. Jacobs, and L. Wartena, Moisture distribution within a maize crop due to dew, *Neth. J. of Agric. Sci.*, *38*, 117–129, 1990.

Baker, J. M., and R. J. Lascano, The spatial sensitivity of time–domain reflectometry, *Soil Sci.*, *147*, 378–384, 1989.

Beers, Y., *Introduction to the Theory of Error*, Addison–Wesley, Reading, MA, 1962.

Beljaars, A. C. M., and P. Viterbo, Soil moisture – precipitation interaction: Experience with two land surface schemes in the ECMWF model, in *Global Energy and Water Cycles*, edited by K. A. Browning and R. J. Gurney, Cambridge University Press, Cambridge, UK, 1999.

Bohren, C. F., and D. R. Huffman, *Absorption and Scattering of Light by Small Particles*, John Wiley & Sons, Inc., New York, 1998.

Bonan, G. B., and L. M. Stillwell-Soller, Soil water and the persistence of floods and droughts in the Mississippi River Basin, *Water Resour. Res.*, *34*, 2693–2701, 1998.

Brunfeldt, D. R., and F. T. Ulaby, Measured microwave emission and scattering in vegetation canopies, *IEEE Trans. Geosci. Remote Sens.*, *GE–22*, 520–524, 1984.

Brunfeldt, D. R., and F. T. Ulaby, Microwave emission from row crops, *IEEE Trans. Geosci. Remote Sens.*, *GE–24*, 353–359, 1986.

Brutsaert, W., *Evaporation in the Atmosphere: Theory, History, and Applications*, D. Reidel, Boston, 1984.

Burke, E. J., L. A. Bastidas, and W. J. Shuttleworth, Exploring the potential for multipatch soil–moisture retrievals using multiparameter optimization techniques, *IEEE Trans. Geosci. Remote Sens.*, *40*, 1114–1120, 2002.

Calvet, J.-C., and J. Noilhan, From near–surface to root–zone soil moisture using year–round data, *J. Hydromet.*, *1*, 393–411, 2000.

Calvet, J.-C., J. Noilhan, and P. Bessemoulin, Retrieving the root–zone soil moisture from surface soil moisture or temperature estimates: A feasibility study based on field measurements, *J. Appl. Meteor.*, *37*, 371–386, 1998.

Campbell, G. S., and J. M. Norman, *An Introduction to Environmental Biophysics*, Springer–Verlag, New York, 1998.

Campbell Scientific, Inc., *CR10X Measurement and Control Module Operator's Manual*, Logan, UT, 2001.

Chang, J.-T., and P. J. Wetzel, Effects of spatial variations of soil moisture and vegetation on the evolution of a prestorm environment: A numerical case study, *Mon. Weather Rev.*, *119*, 1368–1390, 1991.

Chauhan, N. S., D. M. Le Vine, and R. H. Lang, Discrete scatter model for microwave radar and radiometer response to corn: Comparison of theory and data, *IEEE Trans. Geosci. Remote Sens.*, *32*, 416–426, 1994.

Choudhury, B. J., T. J. Schmugge, A. Chang, and R. W. Newton, Effect of surface roughness on the microwave emission from soils, *J. Geophys. Res.*, *84*, 5699–5706, 1979.

Choudhury, B. J., T. J. Schmugge, and T. Mo, A parameterization of effective soil temperature for microwave emission, *J. Geophys. Res.*, *87*, 1301–1304, 1982.

Cole, K. S., and R. H. Cole, Dispersion and absorption in dielectrics. I. Alternating current characteristics, *J. Chem. Phys.*, *9*, 341–351, 1952.

Crosson, W. L., C. A. Laymon, R. Inguva, and C. Bowman, Comparison of two microwave radiobrightness models and validation with field measurements, *IEEE Trans. Geosci. Remote Sens.*, *40*, 143–152, 2002.

Curtis, J. O., Moisture effects on the dielectric properties of soils, *IEEE Trans. Geosci. Remote Sens.*, *39*, 125–128, 2001.

Dasberg, S., and J. W. Hopmans, Time domain reflectometry calibration for uniformly and nonuniformily wetted sandy and clayey loam soils, *Soil Sci. Soc. Am. J.*, *56*, 1341–1345, 1992.

De Loor, G. P., Dielectric properties of heterogeneous mixtures, Ph.D. thesis, University of Leiden, Netherlands, 1956.

Debye, P. J. W., *Polar Molecules*, Dover, New York, 1929.

Delta–T Devices Ltd., *Theta Probe Soil Moisture Sensor User Manual Type ML2x*, Cambridge, England, 1999.

Delworth, T., and S. Manabe, The influence of soil wetness on near–surface atmospheric variability, *J. Climate*, *2*, 1447–1462, 1989.

Dirksen, C., and S. Dasberg, Improved calibration of time domain reflectometry soil water content measurements, *Soil Sci. Soc. Am. J.*, *57*, 660–667, 1993.

Dirmeyer, P. A., and K. L. Brubaker, Contrasting evaporative moisture sources during the drought of 1988 and the flood of 1993, *J. Geophys. Res.*, *104*, 19,383–19,397, 1999.

Dirmeyer, P. A., F. J. Zeng, A. Ducharne, J. C. Morrill, and R. D. Koster, The sensitivity of surface fluxes to soil water content in three land surface schemes, *J. Hydromet.*, *1*, 121–134, 2000.

Dobson, M. C., F. T. Ulaby, M. T. Hallikainen, and M. A. El-Rayes, Microwave dielectric behavior of wet soil – part II: Dielectric mixing models, *IEEE Trans. Geosci. Remote Sens.*, *GE–23*, 35–46, 1985.

Douglas, E. M., R. M. Vogel, and C. N. Kroll, Trends in floods and low flows in the United States: Impact of spatial correlation, *J. Hydrol.*, *240*, 90–105, 2000.

Dutton, E. G., J. J. Michalsky, T. Stoffel, B. W. Forgan, J. Hickey, D. W. Nelson, T. L. Alberta, and I. Reda, Measurement of broadband diffuse solar irradiance using current commercial instrumentation with a correction for thermal offset errors, *J. Atmos. Ocean. Tech.*, *18*, 297–314, 2001.

Eagleman, J. R., and W. C. Lin, Remote sensing of soil moisture by a 21–cm passive radiometer, *J. Geophys. Res.*, *81*, 3660–3666, 1976.

Easterling, D. R., J. L. Evans, P. Y. Groisman, T. R. Karl, K. E. Kunkel, and P. Ambenje, Observed variability and trends in extreme climate events: A brief review, *Bull. Amer. Meteor. Soc.*, *81*, 417–425, 2000a.

Easterling, D. R., G. A. Meehl, C. Parmesan, S. A. Changnon, T. R. Karl, and L. O. Mearns, Climate extremes: Observations, modeling, and impacts, *Science*, *289*, 2068–2074, 2000b.

Easterling, D. R., et al., Maximum and minimum temperature trends for the globe, *Science*, *277*, 364–367, 1997.

Eltahir, E. A. B., A soil moisture – rainfall feedback mechanism 1. Theory and observations, *Water Resour. Res.*, *34*, 765–776, 1998.

England, A. W., Thermal microwave emission from a scattering layer, *J. Geophys. Res.*, *80*, 4484–4496, 1975.

England, A. W., and G. R. Johnson, Microwave brightness spectra of layered media, *Geophysics*, *42*, 514–521, 1977.

Entekhabi, D., H. Nakamura, and E. G. Njoku, Solving the inverse problem for soil moisture and temperature profiles by sequential assimilation of multifrequency remotely sensed observations, *IEEE Trans. Geosci. Remote Sens.*, *32*, 438–447, 1994.

Entekhabi, D., et al., An agenda for land surface hydrology research and a call for the second international hydrological decade, *Bull. Amer. Meteor. Soc.*, *80*, 2043–2058, 1999.

Fairall, C. W., P. O. G. Persson, E. F. Bradley, R. E. Payne, and S. P. Anderson, A new look at calibration and use of Eppley Precision Infrared Radiometers. Part I: Theory and application, *J. Atmos. Ocean. Tech.*, *15*, 1229–1242, 1998.

Ferrazzoli, P., S. Paloscia, P. Pampaloni, G. Schiavon, D. Solimini, and P. Coppo, Sensitivity of microwave measurements to vegetation biomass and soil moisture content: A case study, *IEEE Trans. Geosci. Remote Sens.*, *30*, 750–756, 1992.

Findell, K. L., Atmospheric controls on soil moisture – boundary layer interactions, Ph.D. thesis, Massachusettes Institute of Technology, 2001.

Findell, K. L., and E. A. B. Eltahir, An analysis of the soil moisture – rainfall feedback, based on direct observations from Illinois, *Water Resour. Res.*, *33*, 725–735, 1997.

Findell, K. L., and E. A. B. Eltahir, Analysis of the pathways relating soil moisture and subsequent rainfall in Illinois, *J. Geophys. Res.*, *104*, 31,565–31,574, 1999.

Fischman, M. A., Development of a direct–sampling digital correlation radiometer for earth remote sensing applications, Ph.D. thesis, The University of Michigan, 2001.

Fischman, M. A., and A. W. England, Sensitivity of a 1.4 GHz direct–sampling radiometer, *IEEE Trans. Geosci. Remote Sens.*, *37*, 2172–2180, 1999.

Galantowicz, J. F., D. Entekhabi, and E. G. Njoku, Tests of sequential data assimilation for retrieving profile soil moisture and temperature from observed L–band radiobrightness, *IEEE Trans. Geosci. Remote Sens.*, *37*, 1860–1870, 1999.

Giorgi, F., L. O. Mearns, C. Shields, and L. Mayer, A regional model study of the importance of local versus remote controls of the 1988 drought and the 1993 flood over the central United States, *J. Climate*, *9*, 1150–1168, 1996.

Grant, E., T. Buchanan, and T. Cook, Dielectric behavior of water at microwave frequencies, *J. Chem. Phys.*, *26*, 156–161, 1957.

Groisman, P. Y., R. W. Knight, and T. R. Karl, Heavy precipitation and high streamflow in the contiguous United States: Trends in the twentieth century, *Bull. Amer. Meteor. Soc.*, *82*, 219–246, 2001.

Groisman, P. Y., et al., Changes in the probability of heavy precipitation: Important indicators of climatic change, *Climatic Change*, *42*, 243–283, 1999.

Hallikainen, M. T., F. T. Ulaby, M. C. Dobson, M. A. El-Rayes, and L.-K. Wu, Microwave dielectric behavior of wet soil – part I: Empirical models and experimental observations, *IEEE Trans. Geosci. Remote Sens.*, *GE–23*, 25–34, 1985.

Hanks, R. J., *Applied Soil Physics, Second Edition*, Springer–Verlag, New York, 1992.

Hillhorst, M. A., C. Dirksen, F. W. H. Kampers, and R. A. Feddes, Dielectric relaxation of bound water versus soil matric pressure, *Soil Sci. Soc. Am. J.*, *65*, 311–314, 2001.

Hoekstra, P., and A. Delaney, Dielectric properties of soils at UHF and microwave frequencies, *J. Geophys. Res.*, *79*, 1699–1708, 1974.

Hoekstra, P., and W. Doyle, Dielectric relaxation of surface adsorbed water, *J. Colloid Interface Sci.*, *36*, 513, 1972.

Hoffert, M. I., et al., Advanced technology paths to global climate stability: Energy for a greenhouse planet, *Science*, *298*, 981–987, 2002.

Hong, S.-Y., and E. Kalnay, Role of sea surface temperature and soil–moisture feedback in the 1998 Oklahoma–Texas drought, *Nature*, *408*, 842–844, 2000.

Hong, S.-Y., and H.-L. Pan, Impact of soil moisture anomalies on seasonal, summertime circulation over North America in a regional climate model, *J. Geophys. Res.*, *105*, 29,625–29,634, 2000.

Houser, P. R., W. J. Shuttleworth, J. S. Famiglietti, H. V. Gupta, K. H. Syed, and D. C. Goodrich, Integration of soil moisture remote sensing and hydrologic modeling using data assimilation, *Water Resour. Res.*, *34*, 3405–3420, 1998.

Intergovernmental Panel on Climate Change, *Climate Change 1995: The Science of Climate Change*, Cambridge University Press, London, 1996.

Jackson, T. J., Measuring surface soil moisture using passive microwave remote sensing, *Hydrol. Processes*, *7*, 139–152, 1993.

Jackson, T. J., and L. Moy, Dew effects on passive microwave observations of land surfaces, *Remote Sens. Environ.*, *70*, 129–137, 1999.

Jackson, T. J., and P. E. O'Neill, Attenuation of soil and microwave emission by corn and soybeans at 1.4 and 5 GHz, *IEEE Trans. Geosci. Remote Sens.*, *28*, 978–980, 1990.

Jackson, T. J., T. J. Schmugge, and J. R. Wang, Passive microwave remote sensing of soil moisture under vegetation canopies, *Water Resour. Res.*, *18*, 1137–1142, 1982.

Jackson, T. J., P. E. O'Neill, and C. T. Swift, Passive microwave observation of diurnal surface soil moisture, *IEEE Trans. Geosci. Remote Sens.*, *35*, 1210–1222, 1997.

Jackson, T. J., T. J. Schmugge, P. E. O'Neill, and M. B. Parlange, Soil water infiltration observation with microwave radiometers, *IEEE Trans. Geosci. Remote Sens.*, *36*, 1376–1383, 1998.

Jacobs, A. F. G., and J. H. Van Boxel, Computational parameter estimation for a maize crop, *Bound. Lay. Meteorol.*, *42*, 265–279, 1988.

Jacobs, A. F. G., and W. A. J. Van Pul, Seasonal changes in the albedo of a maize crop during two seasons, *Agric. For. Meteorol.*, *49*, 351–360, 1990.

Karam, M. A., A physical model for microwave radiometry of vegetation, *IEEE Trans. Geosci. Remote Sens.*, *35*, 1045–1058, 1997.

Karl, T. R., and R. W. Knight, Secular trends of precipitation amount, frequency, and intensity in the United States, *Bull. Amer. Meteor. Soc.*, *79*, 1107–1119, 1998.

Karl, T. R., R. W. Knight, D. R. Easterling, and R. G. Quayle, Indices of climate change for the united states, *Bull. Amer. Meteor. Soc.*, *77*, 279–291, 1996.

Kaspar, T. C., S. D. Logsdon, and M. A. Prieksat, Traffic pattern and tillage system effects on corn root and shoot growth, *Agron. J.*, *87*, 1046–1051, 1995.

Kerr, Y. H., P. Waldteufel, J.-P. Wigneron, J.-M. Martinuzzi, J. Font, and M. Berger, Soil moisture retrieval from space: The soil moisture and ocean salinity (SMOS) mission, *IEEE Trans. Geosci. Remote Sens.*, *39*, 1729–1735, 2001.

Knight, J. H., Sensitivity of time domain reflectometry measurements to lateral variations in soil water content, *Water Resour. Res.*, *28*, 2345–2352, 1992.

Knight, J. H., P. A. Ferré, D. L. Rudolph, and R. G. Kachanoski, A numerical analysis of the effects of coatings and gaps upon the relative dielectric permittivity measurement with time domain reflectometry, *Water Resour. Res.*, *33*, 1455–1460, 1997.

Koster, R. D., and M. J. Suarez, The influence of land surface moisture retention on precipitation statistics, *J. Climate*, *9*, 2551–2567, 1996.

Koster, R. D., M. J. Suarez, and M. Heiser, Variance and predictability of precipitation at seasonal–to–interannual timescales, *J. Hydromet.*, *1*, 26–46, 2000.

Kunkel, K. E., K. Andsager, and D. R. Easterling, Long–term trends in extreme precipitation events over the conterminous United States, *J. Climate*, *12*, 2515–2527, 1999a.

Kunkel, K. E., R. A. Pielke Jr., and S. A. Changnon, Temporal fluctuations in weather and climate extremes that cause economic and human health impacts: A review, *Bull. Amer. Meteor. Soc.*, *80*, 1077–1098, 1999b.

Le Vine, D. M., Synthetic aperture radiometer systems, *IEEE Trans. Micro. Theory Tech.*, *47*, 2228–2236, 1999.

Le Vine, D. M., A. Griffis, C. T. Swift, and T. J. Jackson, ESTAR: A synthetic aperture microwave radiometer for remote sensing applications, *Proc. IEEE*, *82*, 1787–1801, 1994.

Lee, J. K., and J. A. Kong, Passive microwave remote sensing of an anisotropic random–medium layer, *IEEE Trans. Geosci. Remote Sens.*, *GE–23*, 924–932, 1985.

Lins, H. F., and J. R. Slack, Streamflow trends in the United States, *Geophys. Res. Lett.*, *26*, 227–230, 1999.

Liou, Y.-A., J. F. Galantowicz, and A. W. England, A land surface process / radiobrightness model with coupled heat and moisture transport for prairie grassland, *IEEE Trans. Geosci. Remote Sens.*, *37*, 1848–1859, 1999.

Macelloni, G., P. Pampaloni, S. Paloscia, and R. Ruisi, Effects of spatial inhomogeneities and microwave emission enhancement in random media: An experimental study, *IEEE Trans. Geosci. Remote Sens.*, *34*, 1084–1089, 1996.

Mahfouf, J.-F., Analysis of soil moisture from near–surface parameters: A feasibility study, *J. Appl. Meteor.*, *30*, 1534–1547, 1991.

Manabe, S., Climate and the ocean circulation: 1, The atmospheric circulation and the hydrology of the earth's surface, *Mon. Weather Rev.*, *97*, 739–805, 1969.

Massman, W. J., A model study of kB_H^{-1} for vegetated surfaces using 'localized near–field' Lagrangian theory, *J. Hydrol.*, *223*, 27–43, 1999.

Meehl, G. A., et al., An introduction to trends in extreme weather and climate events: Observations, socioeconomic impacts, terrestrial ecological impacts, and model projections, *Bull. Amer. Meteor. Soc.*, *81*, 413–416, 2000.

Mintz, Y., and G. Walker, Global fields of soil moisture and land surface evapotranspiration derived from observed precipitation and surface air temperature, *J. Appl. Meteor.*, *32*, 1305–1334, 1993.

Mo, T., B. J. Choudhury, T. J. Schmugge, J. R. Wang, and T. J. Jackson, A model for microwave emission from vegetation–covered fields, *J. Geophys. Res.*, *87*, 11,229–11,237, 1982.

Monteith, J. L., Dew, *Quart. J. Roy. Meteorol. Soc.*, *83*, 322–341, 1957.

National Research Council, *Global Environmental Change: Research Pathways for the Next Decade*, National Academy Press, Washington, DC, 1999.

Neild, R. E., D. A. Wilhite, and K. G. Hubbard, Preseason precipitation probabilities as an aid to corn planting decisions, *Agric. For. Meteorol.*, *41*, 259–266, 1987.

News and Notes, Record cold grips much of the nation in november and december: Two–month period is the coldest on record in the united states, *Bull. Amer. Meteor. Soc.*, *82*, 499–500, 2001.

Newton, R. W., Microwave remote sensing and its application to soil moisture detection, *Tech. Rep. Technical Report RSC–81*, Texas A&M University, College Station, TX, 1977.

Newton, R. W., and J. W. Rouse, Jr., Microwave radiometer measurements of soil moisture content, *IEEE Trans. Antennas Propagat.*, *AP-28*, 680–686, 1980.

Njoku, E., and J. A. Kong, Theory for passive microwave remote sensing of near–surface soil moisture, *J. Geophys. Res.*, *82*, 3108–3118, 1977.

Norman, J. M., and F. Becker, Terminology in thermal infrared remote sensing of natural surfaces, *Agric. For. Meteorol.*, *77*, 153–166, 1995.

Oglesby, R. J., and D. J. Erickson, Soil moisture and the persistence of North American drought, *J. Climate*, *2*, 1362–1380, 1989.

Oh, Y., and Y. C. Kay, Condition for precise measurement of soil surface roughness, *IEEE Trans. Geosci. Remote Sens.*, *36*, 691–695, 1998.

Oki, T., The global water cycle, in *Global Energy and Water Cycles*, edited by K. A. Browning and R. J. Gurney, Cambridge University Press, Cambridge, UK, 1999.

Olhoeft, G. R., Electrical properties of rocks, in *Physical Properties of Rocks and Minerals*, edited by Y. S. Touloukian, W. R. Judd, and R. F. Roy, CINDAS Data Series on Material Properties, Hemisphere, New York, 1989.

O'Neill, P. E., T. J. Jackson, B. J. Blanchard, J. R. Wang, and W. I. Gould, Effects of corn stalk orientation and water content on passive microwave remote sensing of soil moisture, *Remote Sens. Environ.*, *16*, 55–67, 1984.

O'Neill, P. E., N. S. Chauhan, and T. J. Jackson, Use of active and passive microwave remote sensing for soil moisture estimation through corn, *Intl. J. Remote Sens.*, *17*, 1851–1865, 1996.

Or, D., and J. M. Wraith, Temperature effects on soil bulk dielectric permittivity measured by time domain reflectometry: A physical model, *Water Resour. Res.*, *35*, 371–383, 1999.

Pan, Z., M. Segal, R. Turner, and E. Takle, Model simulation of impacts of transient surface wetness on summer rainfall in the United States Midwest during drought and flood years, *Mon. Weather Rev.*, *123*, 1575–1581, 1995.

Pepin, S., N. J. Livingston, and W. R. Hook, Temperature–dependent measurement errors in time domain reflectometry determinations of soil water, *Soil Sci. Soc. Am. J.*, *59*, 38–43, 1995.

Persson, M., and R. Berndtsson, Texture and electrical conductivity effects on temperature dependency in time domain reflectometry, *Soil Sci. Soc. Am. J.*, *62*, 887–893, 1998.

Pitman, A. J., et al., Key results and implications from phase 1(c) of the Project for Intercomparison of Land–surface Parameterization Schemes, *Climate Dynamics*, *15*, 673–684, 1999.

Pollack, H. N., S. Huang, and P.-Y. Shen, Climate change record in subsurface temperatures: A global perspective, *Science*, *282*, 279–281, 1998.

Reda, I., J. R. Hickey, T. Stoffel, and D. Myers, Pyrgeometer calibration at the National Renewable Energy Laboratory (NREL), *J. Atmos. Solar–Terr. Phys.*, *64*, 1623–1629, 2002.

Reichle, R. H., D. B. McLaughlin, and D. Entekhabi, Variational data assimilation of microwave radiobrightness observations for land surface hydrology applications, *IEEE Trans. Geosci. Remote Sens.*, *39*, 1708–1718, 2001.

Rhoades, J. D., N. A. Manteghi, P. J. Shouse, and W. J. Alves, Soil electrical conductivity and soil salinity: New formulations and calibrations, *Soil Sci. Soc. Am. J.*, *53*, 433–439, 1989.

Rind, D., The influence of ground moisture conditions in North America on summer climate as modeled in the GISS GCM, *Mon. Weather Rev.*, *110*, 1487–1494, 1982.

Roads, J., and A. Betts, NCEP–NCAR and ECMWF reanalysis surface water and energy budgets for the Mississippi River Basin, *J. Hydromet.*, *1*, 88–94, 2000.

Schmugge, T. J., Remote sensing of surface soil moisture, *J. Appl. Meteor.*, *17*, 1549–1557, 1978.

Schmugge, T. J., and B. J. Choudhury, A comparison of radiative transfer models for predicting the microwave emission from soils, *Radio Sci.*, *16*, 927–938, 1981.

Schmugge, T. J., and T. J. Jackson, A dielectric model of the vegetation effects on the microwave emission from soils, *IEEE Trans. Geosci. Remote Sens.*, *30*, 757–760, 1992.

Schmugge, T. J., P. Gloersen, T. Wilheit, and F. Geiger, Remote sensing of soil moisture with microwave radiometers, *J. Geophys. Res.*, *79*, 317–323, 1974.

Schmugge, T. J., P. E. O'Neill, and J. R. Wang, Passive microwave soil moisture research, *IEEE Trans. Geosci. Remote Sens.*, *GE–24*, 12–22, 1986.

Schulz, J.-P., L. Dümenil, J. Polcher, C. A. Schlosser, and Y. Xue, Land surface energy and moisture fluxes: Comparing three models, *J. Appl. Meteor.*, *37*, 288–307, 1998.

Segal, M., and R. W. Arritt, Nonclassical mesoscale circulations caused by surface sensible heat–flux gradients, *Bull. Amer. Meteor. Soc.*, *73*, 1593–1604, 1992.

Seyfried, M. S., and M. D. Murdock, Response of a new soil water sensor to variable soil, water content, and temperature, *Soil Sci. Soc. Am. J.*, *65*, 28–34, 2001.

Sharratt, B. S., J. Zandlo, and G. Spoden, Frequency of precipitation across the northern U.S. corn belt, *J. Appl. Meteor.*, *40*, 183–191, 2001.

Shukla, J., and Y. Mintz, Influence of land–surface evapotranspiration on the earth's climate, *Science*, *215*, 1498–1501, 1982.

Stogryn, A., Equations for calculating the dielectric constant of saline water, *IEEE Trans. Micro. Theory Tech.*, *MIT-19*, 733–736, 1971.

Swift, C. T., D. M. Le Vine, and C. S. Ruf, Aperture synthesis concepts in microwave remote sensing of the earth, *IEEE Trans. Micro. Theory Tech.*, *39*, 1931–1935, 1991.

Topp, G. C., J. L. Davis, and A. P. Annan, Electromagnetic determination of soil water content: Measurements in coaxial transmission lines, *Water Resour. Res.*, *16*, 574–582, 1980.

Trenberth, K. E., and C. J. Guillemot, Physical processes involved in the 1988 drought and 1993 floods in North America, *J. Climate*, *9*, 1288–1298, 1996.

Ulaby, F. T., R. K. Moore, and A. K. Fung, *Microwave Remote Sensing: Active and Passive*, vol. 1-3, Artech House, Norwood, MA, 1981-1986.

Ulaby, F. T., M. Razani, and M. C. Dobson, Effects of vegetation cover on the microwave radiometric sensitivity to soil moisture, *IEEE Trans. Geosci. Remote Sens.*, *GE–21*, 51–61, 1983.

Ulaby, F. T., A. Tavakoli, and T. B. A. Senior, Microwave propagation constant for a vegetation canopy with vertical stalks, *IEEE Trans. Geosci. Remote Sens.*, *GE–25*, 714–725, 1987.

Vachaud, G., A. Passerat De Silane, P. Balabanis, and M. Vauclin, Temporal stability of spatially measured soil water probability density function, *Soil Sci. Soc. Am. J.*, *49*, 822–827, 1985.

van Loon, W. K. P., H. M. H. Bastings, and E. J. Moors, Calibration of soil heat flux sensors, *Agric. For. Meteorol.*, *92*, 1–8, 1998.

Walker, J., and P. R. Rowntree, The effect of soil moisture on circulation and rainfall in a tropical model, *Quart. J. Roy. Meteorol. Soc.*, *103*, 29–46, 1977.

Wang, J. R., The dielectric properties of soil–water mixtures at microwave frequencies, *Radio Sci.*, *15*, 977–985, 1980.

Wang, J. R., R. W. Newton, and J. W. Rouse, Jr., Passive microwave remote sensing of soil moisture: The effect of tilled row structure, *IEEE Trans. Geosci. Remote Sens.*, *GE–18*, 296–302, 1980a.

Wang, J. R., J. C. Shiue, and J. E. McMurtrey, III, Microwave remote sensing of soil moisture content over bare and vegetated fields, *Geophys. Res. Lett.*, *7*, 801–804, 1980b.

Wang, J. R., J. C. Shiue, S. L. Chuang, R. T. Shin, and M. Dombrowski, Thermal microwave emission from vegetated fields: A comparison between theory and experiment, *IEEE Trans. Geosci. Remote Sens.*, *GE–22*, 143–150, 1984.

Washington, W. M., Climate–model responses to increased CO_2 and other greenhouse gases, in *Climate System Modeling*, edited by K. E. Trenberth, Cambridge University Press, London, 1992.

Wetherald, R. T., and S. Manabe, Simulation of hydrologic changes associated with global warming, *J. Geophys. Res.*, *107, 4379, doi:10.1029/2001JD001195*, 2002.

Whalley, W. R., Considerations on the use of time–domain relflectometry (TDR) for measuring soil water content, *J. Soil Sci.*, *44*, 1–9, 1993.

White, I., J. H. Knight, S. J. Zegelin, and G. C. Topp, Comments on ’Considerations on the use of time–domain relflectometry (TDR) for measuring soil water content’ by W. R. Whalley, *Europ. J. Soil Sci.*, *45*, 503–508, 1994.

Wigneron, J.-P., J.-C. Calvet, Y. Kerr, A. Chanzy, and A. Lopes, Microwave emission of vegetation: Sensitivity to leaf characteristics, *IEEE Trans. Geosci. Remote Sens.*, *31*, 716–726, 1993.

Wigneron, J.-P., J.-C. Calvet, and Y. Kerr, Monitoring water interception by crop fields from passive microwave observations, *Agric. For. Meteorol.*, *80*, 177–194, 1996.

Wigneron, J.-P., A. Olioso, J.-C. Calvet, and P. Bertuzzi, Estimating root zone soil moisture from surface soil moisture data and soil–vegetation–atmosphere transfer modeling, *Water Resour. Res.*, *35*, 3735–3745, 1999.

Wigneron, J.-P., L. Laguerre, and Y. H. Kerr, A simple parameterization of the L–band microwave emission from rough agricultural soils, *IEEE Trans. Geosci. Remote Sens.*, *39*, 1697–1707, 2001.

Wilson, T. B., W. L. Bland, and J. M. Norman, Measurement and simulation of dew accumulation and drying in a potato canopy, *Agric. For. Meteorol.*, *93*, 111–119, 1999.

Wraith, J. M., and D. Or, Temperature effects on soil bulk dielectric permittivity measured by time domain reflectometry: Experimental evidence and hypothesis development, *Water Resour. Res.*, *35*, 361–369, 1999.

Yasuda, N., Turbulent diffusivity and diurnal variations in the atmospheric boundary layer, *Bound. Lay. Meteorol.*, *43*, 209–221, 1988.

Yeh, T. C., R. T. Wetherald, and S. Manabe, The effect of soil moisture on the short–term climate and hydrology change: A numerical experiment, *Mon. Weather Rev.*, *112*, 474–490, 1984.